Characterization of wave impact loading on structures at full scale : field experiment, statistical analysis and 3D advanced numerical modeling

Pierre-Antoine Poncet

École doctorale des sciences exactes et leurs applications

Characterization of wave impact loading on structures at full scale : field experiment, statistical analysis and 3D advanced numerical modeling

THÈSE

présentée et soutenue publiquement le xx xxxx 2021

pour l'obtention du

Doctorat de l'Université de Pau et des Pays de l'Adour

(mention Génie-Civil)

par

Pierre-Antoine Poncet

Composition du jury

Rapporteurs :	Frédéric Dias	University College Dublin, School of Mathematics and Statistics
	Vincent Rey	Mediterranean Institute of Oceanography (MIO) Université de Toulon

Laboratoire des sciences pour l'ingénieur appliquées à la mécanique et au génie électrique
Fédération de recherche CNRS IPRA — Équipe interaction vagues structures

Contents

Acknowledgements

I want to deeply thank Stéphane Abadie for giving me the opportunity to conduct my thesis on the experiments at the Artha breakwater. With Benoit Larroque they started this experiments in 2013. It is an exceptional site and I am therefore honoured to have been able to work on a subject that make so much sense for me. I would also like to thank Benoit Liquet for his time and help with the statistics and Damien Sous for his guiding during the underwater measurement campaign and the post-processing of the data. I feel extremely lucky to have had the opportunity to learn from them all and get precious knowledge from their very different expertise. This diversity was one of the main challenges of this thesis and none of it would have been possible without the pedagogy of all my supervisor. I would also like to thank Volker Roeber for his precious teachings on Boussinesq models.

This work wouldn't have been the same without the collaboration with Dorian D'Amico who provided an essential help on data management. It is his work that made it possible for me to focus on physical processes.

I also want to thank my fellow doctorate student and members of the SIAME laboratory who made the day to day life at office so enjoyable. Thank you Florian, Sophie, Lucie, Delphine, Amaia, Manuel, Ximun and Youssef for the support and precious advice during the essential coffee breaks.

Finally I want to express all my gratitude towards my family and friends who supported and followed me during this period. My parents for their support in my choice, my grand-father for giving me so many wise advice during the more difficult part at the end of the thesis. To all my friend who were there for me during the difficult times, I can't thank you enough.

Abstract

This thesis aims at better understanding the solicitations generated by waves on coastal structures, focusing on breaking and broken waves. The Artha breakwater, protecting the bay of St-Jean de Luz, in the southwest of France, has been equipped with high frequency pressure sensors since 2015 allowing the collection of an extensive dataset. The chosen site, is indeed characterized by very energetic wave conditions, making it a very interesting site for such measurements. Using the collected database, the thesis try to bring new knowledge on the local hydrodynamics and loading acting in-situ, from the global influence of environmental conditions to the mechanics of wave impacts. The work is divided in the three following independent parts which, each, deals with a different aspect of the problem. The first part proposes and an analysis of the data collected at the Artha breakwater. The details of the high frequency pressure measurements on the wall of the Artha western roundhead are presented as well as the simultaneous recording of offshore wave parameters, water level and local wind. Based on this database, statistical models are implemented and analyzed. These models provide predictions of the maximal pressure acting on the instrumented wall in function of the external conditions. An analysis of the pressure signal is also conducted and shows the existence of highly impulsive impacts, which nevertheless, appear as outliers. The stability of the breakwater is finally assessed. Numerous hypothesis have to be done for the estimation, leaving many unresolved questions. In particular, it appears that computing the load requires to know the maximal wave height in front of the breakwater. The study of the hydrodynamic in the vicinity of the breakwater is therefore required and is the object of the second chapter of the thesis. This chapter uses the results of measurements carried out with immersed, independent sensors in the block armour. Modulations of the significant wave height and reflection coefficient by the block armour in function of water level are detailed based on the measurements. 2DV numerical simulations with the SWASH model are also carried out to reproduce these results after calibration. Based on this model, the maximal wave height and surf zone extent are determined for ten different scenarios, allowing to estimate the maximal pressure on the wall according to the Goda formula. The predictions of Goda's theory are next compared with the predictions of the statistical model of the first chapter. The latter provides as expected weaker values compared to Goda's formula. Other parameters can nevertheless explain this difference, and in particular the circular shape of the western roundhead. In the third and last chapter, wave impact on cylinders with various radius are investigated with a Navier-Stokes VOF numerical model (i.e., the OpenFoam interFoam solver). The influence of the radius on the maximal force applied on the initially impacted line of the cylinder is shown to be nonlinear. Those results are compared with the prediction of classical engineering formula which predicts a linear behavior. The severeness of the impact and the location of maximal pressure on the cylinder is also studied by sligthly shifting the initial free surface. One interesting results is that the maximal pressure is not located on the initially impacted line for the violent sloshing impacts studied.

Cette thèse vise à mieux comprendre les sollicitations générées par les vagues sur les structures côtières, en se focalisant sur les vagues déferlantes et déferlées. Dans ce but, la digue de l'Artha, protégeant la baie de St-Jean de Luz, a été équipée de capteurs de pression haute fréquence depuis 2015 permettant la collecte d'un large jeu de données. Le site choisi, est caractérisé par des conditions de houle très énergiques, ce qui en fait un site très intéressant pour de telles mesures. En utilisant la base de données collectée, la thèse tente d'apporter de nouvelles connaissances sur l'hydrodynamique locale et les forces qui agissent en nature, en s'intéressant à l'influence globale des conditions environnementales ainsi qu'à la mécanique de l'impact des vagues. Le manuscrit est divisé en trois parties indépendantes qui, chacune, traite d'un aspect différent du problème. La première partie propose une analyse des données collectées sur la digue de l'Artha. Les mesures de pression réalisées à haute fréquence sur le musoir ouest de l'ouvrage sont présentées ainsi que les données simultanées des paramètres de vagues en mer, du niveau d'eau et du vent local. A partir de cette base de données, des modèles statistiques sont mis en oeuvre et analysés. Ces modèles fournissent des prédictions de la pression maximale agissant sur la paroi instrumentée en fonction des conditions externes. Une analyse du signal de pression est également menée et montre l'existence d'impacts impulsifs, qui apparaissent néanmoins en tant qu'outliers dans le jeu de données. La stabilité de la digue est enfin évaluée. De nombreuses hypothèses doivent être faites pour cette estimation, laissant de nombreuses questions non résolues. En particulier, il apparaît que le calcul de la charge nécessite de connaître la hauteur maximale des vagues devant l'ouvrage. L'étude de l'hydrodynamique au voisinage du brise-lames est donc nécessaire et fait l'objet du deuxième chapitre de la thèse. Ce chapitre utilise les résultats de mesures effectuées avec des capteurs indépendants immergés dans la carapace. Les modulations de la hauteur significative de la vague et du coefficient de réflexion en fonction du niveau d'eau sont détaillées à partir des mesures. Des simulations numériques 2DV avec le modèle SWASH sont également réalisées pour reproduire ces résultats après calibration. Sur la base de ce modèle, la hauteur maximale des vagues et l'étendue de la zone de déferlement sont déterminées pour dix scénarios différents, permettant d'estimer la pression maximale sur le mur selon la formule de Goda. Les prédictions de la théorie de Goda sont ensuite comparées aux prédictions du modèle statistique du premier chapitre. Ce dernier fournit comme prévu des valeurs plus faibles par rapport à la formule de Goda. D'autres paramètres peuvent néanmoins expliquer cette différence, et notamment la forme circulaire du musoir. L'effet du rayon de courbure sur l'intensité de l'impact est ainsi étudié dans le dernier chapitre. Dans ce chapitre, l'impact des vagues sur des cylindres de différents rayons est étudié avec un modèle numérique VOF de Navier-Stokes (c'est-à-dire le solveur OpenFoam interFoam). L'influence du rayon sur la force maximale appliquée sur la ligne initialement impactée du cylindre s'avère être non-linéaire, contrairement à ce que prévoient les formules d'ingénieries classiques. La sévérité de l'impact et l'emplacement de la pression maximale sur le cylindre sont également étudiés en déplaçant légèrement la surface libre initiale. Un résultat intéressant est que la pression maximale n'est pas située sur la ligne initialement impactée pour les impacts violents de type sloshing étudiés ici.

Introduction

With more than half of the world population living nowadays in coastal areas, an accurate assessment of the coast vulnerability has become a necessity. Nevertheless, it remains, even today, a challenge, as various coast typologies coexist in the world (i.e., sand beaches, pockets beaches, urbanized areas, etc.), with potentially different physical processes governing their dynamics. The present work focuses on a specific breakwater, a common feature in urbanized coastal environments. The overall objective is to characterise and predict the local hydrodynamics and loading acting in-situ, for which, as we shall see, the present literature appears quite reduced. The studied environment also exhibits geometrical features which share potentially common aspects with rocky beaches bounded by cliffs (i.e., very heterogeneous, sometimes steep, bathymetry, vertical surfaces, etc.). As such, this thesis addresses a quite general problem with broader applications than the sole local object.

Breakwaters are designed to protect the coast against specific hazards. Broadly speaking, coastlines are submitted to various wave climates and exposed to diverse natural phenomena ranging from storms with different impacts to tsunamis. Owing to this variability, breakwaters can take various shapes and positions with respect to the coastline. Overall three main types of breakwater exist: rubble mound breakwaters, caisson breakwaters and composite breakwaters. Rubble mound breakwaters consist in an arrangement of rock or concrete elements that dissipate wave energy through porosity. Caisson breakwaters offer a vertical concrete structure to the ocean. The function of this type of structure is more to reflect than dissipate wave energy. Composite breakwaters share the two previous components. For the latter type, depending on the slope, depth and surrounding bathymetry, the wave interaction with the breakwater may take different forms. It is the purpose of the present work to better understand the various functioning modes of composite breakwaters.

Wave impact has been, for a long time now, identified as one of the main source of breakwater damages. The latter can take different forms and intensities, from local alteration of the structure, requiring recurrent repairing by the stakeholders, to more dramatic events with heavy social and economical costs. The aim of this study is therefore also focused on waves impact. Wave impact pressure on vertical wall have been widely studied in controlled environments [Bagnold, 1939, Hattori and Arami, 1993, Hofland et al., 2011] and by means of numerical models [Martin-Medina et al., 2018, Lugni et al., 2010, Scolan, 2010]. The physical processes governing wave impact are relatively well known. Several engineering formula have been published witnessing this knowledge [Goda, 1975, Oumeraci et al., 2001]. Nevertheless, the shift from the lab scale to the one of the real field still requires field data which appear to be scarce in the literature. The reason of that is the difficulty to perform wave impact pressure measurements in nature due to the severity of the phenomena. To that respect, for instance, measurements conducted more than 80 year ago [Rouville et al.,

1938] are still mentioned as one of the most complete dataset. Nevertheless, the development of embedded systems and remote communication now gives access to technologies that far surpass the ones involved in older experiments. The quite limited range of wave conditions observed in the most cited experiments [Rouville et al., 1938, Bullock et al., 2001] also suggests the need for long term observations in the adequate environment.

The former reasons led us to undertake a long term monitoring at the Artha breakwater, a detached structure protecting the bay of St-Jean de Luz in the southwest of France (Figure 1). The location of this structure, in the bay of Biscay, is obviously characterised by very energetic wave conditions. As an illustration, in February 2017, a 50000 kg bloc of concrete was displaced from the block armour below the mean water level to the top of the breakwater (Figure 2). This type of events already occurred several times in the past which gives an idea of the violence of waves in this area.

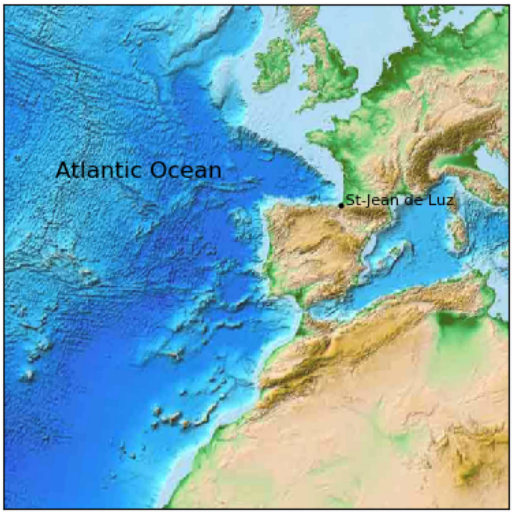

Figure 1: Geographical situation of the studied site

During the 17th and 18th centuries, the towns of St-Jean de Luz and Ciboure were submitted to several significant flooding during storms that destroyed numerous buildings. Following those events, several attempts were made to protect the bay. At the end of the 19th century, the three breakwaters that we know today, namely the Artha breakwater detached from land, the Socoa breakwater to the west and the St Barbe breakwater to the east (Figure 3), were built. Artha is a 255m long structure set upon an existing reef over 120m on the west while the remaining part sits on sand. This breakwater displays a block armour made up of 50 tons concrete blocks. As already mentioned, a few of these blocks have already been found on the top of the caisson, 6.9 m over the mean water level. An overall displacement of the blocks towards the east is also regularly observed as well as local erosion of the wall masonry. Theses damages require regular maintenance operations by the stakeholders (i.e. the Departmental Council CD64) to keep the breakwater functional.

The depth in front of the western round head is of 15m, but the bathymetry in the area is fairly complex

a) b)

Figure 2: Snapshots from the storm of February 28, 2017. a) photograph of a wave impacting the Artha breakwater, b) photograph of a 50T block displaced by a wave during this storm.

with shallower areas on the eastern part and in front of Socoa breakwater (Figure 3). Several reefs and troughs can be identified which likely affect wave transformation from the offshore domain to the toe of the breakwater making refraction and shoaling processes complex in this area. Additionally, wave breaking more than 1km offshore are regularly observed during the main winter storm. In the bay, the depth is globally lower than 10m.

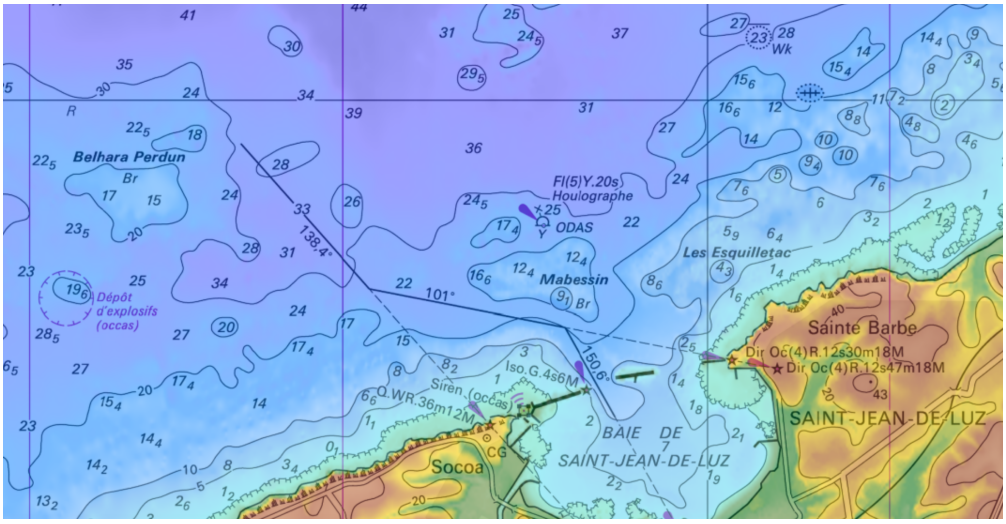

Figure 3: Bathymetry in the area of the Artha breakwater

Based on swell orientation [Kergadallan et al., 2020] and observation of damages, the most exposed part of the Artha breakwater may be the western roundhead. We, therefore, selected this area to install the high frequency pressure sensors which have been used to collect data since 2015 (with some interruptions). In parallel, the bay of St-Jean Luz is also monitored with several other sensors including a directional wave buoy about 1 km offshore, a tide gauge located inside the bay on a nearby pier (i.e. the Socoa tide gauge), and a bit further up, a weather station installed on the Socoa semaphore which among others, records wind measurements.

During the thesis, a shorter campaign, involving wave measurements above the blocks, has also been performed. Additionally, several models were used to complement or analyse the data, among which, numerical models (SWASH, OPENFOAM) and statistical models. The different parts are described in the next chapters following the outlines proposed hereafter.

Chapter 1 presents a short state of the art on wave impact field and laboratory experiments which support the scientific questions of the thesis. Then chapter 2 gives methodological complements which come in addition to the more detailed description of the work given in the following chapters. Chapter 3 proposes a presentation and an analysis of the data collected at the Artha breakwater, namely the high frequency pressure measurements as well as the simultaneous measurements of the environmental variables. Based on this database, statistical models, providing a prediction of the maximal pressure acting on the instrumented wall in function of the external conditions are developed. Chapter 4 proposes the study of the wave field in the vicinity of the breakwater. This chapter uses the results of measurements carried out with immersed, independent sensors in the block armour and numerical modelling. In chapter 5, wave impact on cylinders with various radius are investigated with a Navier-Stokes VOF numerical model (i.e., the OpenFoam interFoam solver) in order to better understand the role of the roundhead shape on the impact distribution. Finally a conclusion chapter attempts to conclude this work and draw perspectives for the future.

It has to be stressed here that the main chapters of the thesis (i.e., chapter 3, chapter 4 and chapter 5) were constructed as separated entities with the idea to propose them later for publication. Therefore, for each part, a state of the art specific to the problematic and the methods employed, are detailed. We apologise in advance for the few repeats that the reader may found, here and there, in the text.

Finally note that this PhD thesis was funded by the E2S UPPA ISITE project, and supported by the European projects MAREA and EZPONDA.

Chapter 1

State of the art and scientific questions

Wave impacts have been early identified as one of the main source of breakwater failure, which in turn, led to the development of an active research on this topic. In this chapter, a non extensive literature review is proposed to support the questions addressed in this thesis and bring a few scientific elements to understand the following chapters.

1.1 Environmental parameters and impact pressures in field experiments

Field wave impact pressure measurements have been conducted since the 19th century (Figure 1.1 from Blackmore and Hewson [1984]).

One of the most extensive dataset is described in Rouville et al. [1938]. In 1938, the french engineer M.A. de Rouville conducted several field experiments in Dieppe on the north west coast of France. To that occasion, different types of sensors were presented as well as mechanical tests on metallic cylinder submitted to wave impacts. Most of them were found to be limited by their response frequency leading to the choice of piezoelectric quartz pressure sensors to finally equip the vertical wall of the breakwater head. The measurements required the intervention of an operator for several reasons. First, the membrane of the sensor being sensitive, it is protected by a remotely removable protection. Secondly, The wave parameters offshore the breakwater had to be visually estimated. And finally, the vertical velocity of the upward jet was also measured thanks to a video camera.

The main results of this experiment are summed up in figure 1.2. From this experiment, De Rouville concluded that the highest pressure is not generated by the largest waves. In particular, the maximum impact (i.e., 6.9 bar) was recorded with an offshore wave height of about 1.8 m and a breaking wave estimated at 2.5 m. The pressure signal associated with this impact is presented in figure 1.3. On the lower sensor, the rise time from 0 to 6.9 bar is 5 ms. A vertical variability of the peak pressure is observed, with, overall, the higher the sensor, the lower the pressure (note that for some other impacts, higher pressures were observed at higher locations). The upward water jet vertical velocity was estimated at 23 $m.s^{-1}$ (Note that even higher values (35 $m.s^{-1}$) were measured in 1933 when the piezoelectric sensors were not yet installed.). During this experiment, wave heights ranged from 1.50 m to 4.50 m with associated wave lengths from about 35 m

TABLE 1

Results from all known investigations to measure wave impact pressures on seawalls and breakwaters

Investigator	Location of measurements	P_i max (kN/m²)	P_i ave (kN/m²)	H_b (m)
T. Stevenson	Skerryvore Rocks, 1843—1844	291	100	—
	Bell Rock	145	—	—
	Dunbar Harbour, 1858	375	—	6.1
	Buckie	322	—	6.1
F. Latham	Penzance Harbour, England	—	96	—
H.M. Robert	Oswego Harbour, N. York, 1884	45	24	5.0
C.H. McKinstry	Milwaukee Bay, 12/2/1894	68	—	—
	Milwaukee Bay, 8/4/1894	165	—	4.0
D.D. Gaillard	St. Augustine, Fla. 1890—1891	32	—	1.8
	Lake Superior, S. Pier, 1902	113	—	4.9
	Lake Superior, S. Pier, 1902	79	—	4.0
	Lake Superior, E. B'water, 1902	121	—	—
	Black Rock, 1902	99	—	—
D.A. Molitor	Lake Ontario, Canada, 1915	30	—	2.8
I. Hiroi	Otaru Harbour, Japan, 1920	345	—	—
L. Luiggi	Port of Valparaiso, 1921	322	—	7.0
M.A. Rouville et al.	Dieppe, France, 1937	690	—	2.5
P.D. Cot	Le Havre, France, 1937	98	—	2.5
T. Kuribayashi et al.	Haboro Harbour, Japan, 1957	110	—	4.5
R.L. Millar et al.	Cape Cod, U.S.A., 1974	41	19	0.9

Figure 1.1: Synthesis of wave impact in-situ measurements prior to 1984 from Blackmore and Hewson [1984].

to 50 m, (measured by sight).

Between 1938 and 1984, only two experiments are mentioned in the literature. Kuribayashi et al. [1959] used electric strain gauge pressure sensors to measure wave impact on field. Different types of impact were identified and the influence of the wave period remarked. Miller et al. [1975] conducted measurements on a regular sloping beach with important tidal variation. The sensors were located on a dedicated plate partly immersed in this environment. With varying water levels, the sensors measured at various location in the surf-zone, also collecting different type of wave impacts, from sloshing to broken wave impacts.

Blackmore and Hewson [1984] conducted successive experiments at several seawalls over a duration of four years. Due to the few data collected at at the other sites, they finally focused on the Ilfracombe seawall, a structure displaying a curved reentrant face. At this site, five transducers (natural frequency of more than 15 kHz) were set-up on the vertical and 4 horizontally. Incoming waves were measured by means of three additional transducers located on the beach. 112 impacts were measured in 350 h with wave heights ranging between 0.8 m and 1.3 m and wave period between 2.67 s and 8.50 s. Typical church spire shape impact signal were reported.

DATES ET HEURES.	CARACTÉRISTIQUES DE LA HOULE					VITESSE VERTICALE initiale (en mètres par seconde).	PRESSIONS ENREGISTRÉES (EN TONNES PAR MÈTRE CARRÉ) à		
	AU LARGE.			AU DÉFERLEMENT.			0 m.35	1 m. 35	2 m. 35
	Longueur d'onde (en mètres).	Creux (en mètres).	Célérité (en mètres par seconde).	Creux (en mètres).	Vitesse horizontale (en mètres par seconde).		du pied de la jetée.		
1933.									
3 novembre à $13^h 52^m$	40 00	1 50	6 00	2 00	12 00	77 00	//	//	//
1935.									
2 décembre à $12^h 08^m$	//	//	//	//	//	//	18	7	//
2 décembre à $12^h 12^m$	//	//	//	//	//	//	20	19	//
2 décembre à $12^h 13^m$	//	//	//	//	//	//	52	25	//
16 décembre à $12^h 35^m$	//	//	//	//	//	//	23	31	22
16 décembre à $12^h 45^m$	//	//	//	//	//	//	18	27	12
1937.									
9 février à $12^h 27^m$	45 00	2 50	6 00	3 50	6 50	31 00	16	8	0
9 février à $12^h 30^m$	45 00	2 50	6 00	3 50	7 50	37 00	40	10	2
23 février à $12^h 21^m$	40 00	1 80	6 00	2 50	8 50	23 00	69	7	0
23 février à $12^h 37^m$	40 00	1 80	6 00	2 50	6 80	25 00	62	3	0
1er mars à $15^h 56^m$	40 00	2 50	5 50	3 50	11 50	32 00	37	4	0

Figure 1.2: Main results of the experiment carried out in Dieppe by De Rouville

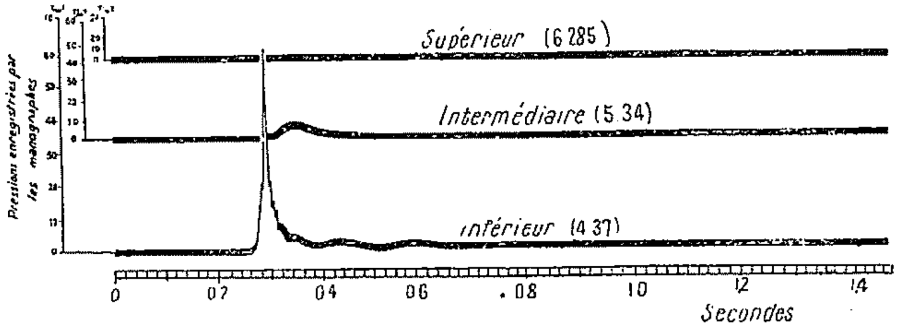

Figure 1.3: Pressure signal associated with the highest pressure peak measured (6.9 bars) by de Rouville

In Bird et al. [1998], an array of sensors was set-up at the Alderney breakwater in the Channel island, recording both pressure and aeration rate, the latter being identified as a potential contributor to the pressure damping reported between model and real scale [Peregrine, 2003]. This experiment lasted several years leading to important papers [Bird et al., 1998, Bullock et al., 2001, 2007]. Different types of impacts were identified and the influence of the aeration level highlighted. Additionally, a correlation between risetime and maximal pressure was presented following Blackmore and Hewson [1984] works.

In all the past experiments, there is no mention of a systematic and extensive study of the influence of environmental conditions, namely, mainly wave parameters and water level, on wave impact pressures. This is likely due to the difficulty to measure this very transient phenomenon over a long period of time in conjunction with local wave conditions. It has to be reminded here that the highest pressures are not necessarily observed during the most severe wave conditions [Rouville et al., 1938]. Nevertheless, this statement has to be precised and this will be the goal of the chapter 3 of this thesis.

1.2 A few elements on the wave impact physics

1.2.1 Impacts with air entrapment

Complex physical phenomena take place during natural wave impacts in which, hydrostatic and dynamic pressures have their own contribution. Moreover, gravity waves being at the interface between water and air, a breaking wave may entrap a variable quantity of air in function of its shape. As a result, for certain types of impact, air compressibility has to be taken into account.

One of the first to study aerated waves impacts is Bagnold [1939]. In the latter work, the following impact types were identified depending on the position of the breaking point with respect to the obstacle : broken waves impacts, impacts with large cushion of air entrapped and impact with thin horizontal air pockets entrapped. It is also shown that the integral of the pressure signal in time tends to a definite value (for a given wave height) called the pressure impulse. This implies that the impacts reaching the highest pressure last a shorter time. The maximum pressure value observed in Bagnold [1939], is of 1/6 the theoretical value expected in the case of a water hammer, and 1/14 the largest value recorded during the in-situ experiments of Rouville et al. [1938] in Dieppe.

Bagnold [1939] also shows that the maximum pressure generated by a wave impact can be determined by solving the problem of a cylinder of water of unit cross section and length K travelling with initial velocity U, which enters the mouth of a cup of depth D containing air initially at atmospheric pressure.

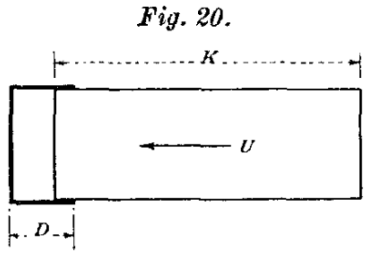

Figure 1.4: Sketch of Bagnold's piston source : (Bagnold [1939])

It is assumed that when air is entrapped, the momentum of the water mass is absorbed by the force of the compressed air over the area of the water surface. The momentum ρUK is equal to the time integral of the local pressure on the wall (i.e., the pressure impulse). Under those assumptions and with this conceptual model, pressure impulse is shown to be a stable parameter for a given wave height and period. Indeed the wave height and celerity, respectively represented by K and U in the model, are controlled by wave period and local bathymetry before impact. The value of the integral can be obtained from the pressure time serie and the wave celerity is known, therefore K can be calculated by :

$$K = \frac{\int p \, \mathrm{d}t}{\rho U} \tag{1.1}$$

K is found to be 1/5 of the wave amplitude in Bagnold's experiment. When compared to the values obtained in De Rouville's experiment, the maximal pressure according to the piston theory, taking $K = \frac{2h}{5}$ ($2h$ being the through to crest wave height in Bagnold [1939]), is exceeded in 2 cases, for seven interesting

wave impulses. One explanation could be that K actually takes higher values than $\frac{2h}{5}$ in the field.

For fixed K and U, typical pressure-time curves were computed for different D for the two different scales studied, leading to the following empirical relation linking the maximum pressure to the parameters of the problem :

$$(p_{max} - p_0) = 2.7\frac{\rho U^2 K}{D} \tag{1.2}$$

Aerated impacts are seemingly observed in this thesis in chapter 3. While the pressure signals measured in the present field experiment are far from the idealised Bagnold case, the model formerly described provides a simple conceptual tools to better understand the phenomenon.

1.2.2 Scaling : from prototype to natural scale

Larger pressures have been acknowledgedly recorded in controlled small scale environments compared to the field scale [Hofland et al., 2011, Bullock et al., 2005]. The scaling number for inertia gravity flow in water is the Froude number $Fr = \frac{U}{\sqrt{gh}}$, for the inertia compression flow in the air it is the Cauchy number $Ca = \frac{\rho_e U^2}{\gamma p_0}$. It is therefore difficult to extrapolate pressure from smaller scale test in laboratory to full scale while maintaining the Froude and Cauchy ratio. The impact scaling issue has been for instance addressed by Faltinsen and Timokha [2009] and Bogaert et al. [2010] in the context of LNG Tanks. Using Froude scaling, a good agreement between the dimensionless maximal pressures at the two scales is achieved while a clear difference is observed regarding the frequency. Kimmoun et al. [2010] obtained different results while comparing small and large scale tests. In this case, the maximal pressure scaled with $\sqrt{\lambda}$ (with λ the geometrical scale). Yet, Bogaert et al. [2010] showed that those two results were compatible in the light of the dimensionless impact number based on Bagnold's model. Nevertheless, the difficulty to properly scale aerated wave impacts clearly remains.

It was one of the purpose of the present experiment to collect field data as complete as possible in order to address this scale question in the future. Nevertheless, in non-controlled environment, several problems makes the analysis more complex as described in the following subsections.

1.2.3 Wave shape before impact

As mentioned by Peregrine [2003] for instance, the wave shape before impact highly controls the pressure signal. In a recent review, Dias and Ghidaglia [2018] proposed an extensive description of the different loading processes in function of the wave shape before impact with three main elementary loading processes (ELP). Each one of these ELPs is properly described by a theory associated with a specific scaling law. These elements are referred to in this thesis, particularly in chapter 3 and chapter 5. In the field experiments mentioned previously, the waves transformation was not studied and therefore, the wave shape at the impact remains totally unknown. Even though a perfect definition of the impacting wave would be beyond any reachable result, a relative knowledge of the wave field during the measurements is certainly an added-value to interpret the results.

In the literature, field measurements of wave transformation were mostly conducted for low sloping beaches [Ruessink et al., 1998, Senechal et al., 2011]. Therefore, the wave propagation and subsequent breaking and run-up in steep rocky beaches or on man-made structures is less well understood. Regarding

this issue, most of the knowledge comes from laboratory experiments conducted by coastal engineers (e.g., Van der Meer and Stam [1992]). Field experiments only appeared recently due to the intrinsic difficulties to undertake this type of measurements. For instance, Dodet et al. [2018] studied the wave field in the intertidal zone of rocky beaches in cliffs environments with slopes $0.1 < \tan(\beta) < 0.4$ using an array of pressure sensors.

The present thesis also proposes field measurements of the wave field before impacts (chapter 4). The aim here is to better understand the pressures measured synchronously on the obstacle and validate a numerical model.

1.2.4 3D versus 2D

Even though scaling is an acknowledged issue, other factors can also explain the difference observed at the two scales as mentioned in Peregrine [2003]. In particular, the three dimensionality of the wave impacts in real conditions is a very strong factor which differs from the controlled experiments usually performed. The three dimensionality may come from the wave itself [Peregrine, 2003] or the obstacle shape. Regarding the latter, there are numerous studies on wave impact on cylinders as this type of structure is commonly met in maritime Engineering. Nevertheless, few have addressed the case of large relative radius as found for instance in the case of a breakwater roundhead. *It is the aim of chapter 5, to address this issue numerically.*

1.2.5 On Engineering formula

Finally, from a practical point of view, there is obviously a need for an accurate determination of the critical load due to waves on coastal and marine structures. Nevertheless, owing to the inherent difficulty of the impact phenomenon, the complexity of real structures as well as of the surrounding environment, the design load determination still largely relies on physical tests, conducted for each different projects and on empirical formula (e.g., Goda [1975], Takahashi [2002]). The latter integrates many complex processes in a supposedly conservative way. Therefore, the gap between the extensive knowledge of the physical processes involved (waves, impact, etc.) and the engineering application of this knowledge appears significant. Moreover, in the studies described in Bird et al. [1998], Bullock et al. [2007], Bullock G. et al. [2004] and derived from the latest extensive in-situ wave impact pressure measurements, results were not compared with the classical engineering formula and therefore the latter only rely on physical tests.

Therefore, it appears interesting to compare field data with design formula to quantify the discrepancy. This will be also performed in chapter 4 where we compare statistically our data with the classical formula used to design vertical breakwaters [Goda, 1975].

Chapter 2

Complements on methodology

This chapter provides information on methods or results which are used in the following chapters. This information should be seen as a complement of the methodological section of the next three chapters.

2.1 Statistical models

In chapter 3, linear and non linear statistical models are employed. Additionally, throughout the thesis, multiple single variable linear regressions are conducted. The principles of this method are explained hereafter.

Linear regression models aim at determining a linear relationship between an explanatory variable (or predictor variable) x and a variable of interest (or response variable) y. Assuming that the response variable (y) has a constant variance whatever the value of the variable (x) (homoscedasticity), the model is of the following form :

$$y_i = \alpha + \beta x_i + \epsilon_i \tag{2.1}$$

with y_i and x_i the i-th observation of the respective variables and ϵ_i the error. In chapter 3, linear models involving several explanatory variables are presented. To determine α and β the least square method is employed. In this case, we seek to minimise :

$$\sum_{i=1}^{n} \epsilon_i^2 = \sum_{i=1}^{n} (y_i - \alpha - \beta x_i)^2 \tag{2.2}$$

the solution is given by :

$$\hat{\beta} = \frac{\sum_{i=1}^{n}(x_i - \overline{x})(y_i - \overline{y})}{\sum_{i=1}^{n}(x_i - \overline{x})^2} \tag{2.3}$$

and

$$\hat{\alpha} = \bar{y} - (\hat{\beta}\overline{x}) \tag{2.4}$$

The coefficient of determination R^2 is then :

$$R^2 = \frac{(\overline{xy} - \overline{x}\overline{y})^2}{(\overline{x^2} - \overline{x}^2)(\overline{y^2} - \overline{y}^2)} \tag{2.5}$$

with this value, we provide an estimate of the share of variability explained by the predictor variable.

This model can be generalised to k explanatory variables. In this case the model is now :

$$y_i = \beta_0 + \beta_1 x_{i,1} + \beta_2 x_{i,2} + ... + \beta_k x_{i,k} + \epsilon_i \tag{2.6}$$

which in matrix notation, gives :

$$Y = X\beta + \epsilon \tag{2.7}$$

with :

$$Y = \begin{pmatrix} y_1 \\ y_2 \\ \vdots \\ y_n \end{pmatrix} \tag{2.8}$$

$$X = \begin{pmatrix} 1 & x_{11} & \cdots & x_{1k} \\ 1 & x_{21} & \cdots & x_{2k} \\ \vdots & \vdots & \ddots & \vdots \\ 1 & x_{n1} & \cdots & x_{nk} \end{pmatrix} \tag{2.9}$$

$$\beta = \begin{pmatrix} \beta_0 \\ \beta_1 \\ \vdots \\ \beta_k \end{pmatrix} \tag{2.10}$$

$$\epsilon = \begin{pmatrix} \epsilon_1 \\ \epsilon_2 \\ \vdots \\ \epsilon_n \end{pmatrix} \tag{2.11}$$

The least square estimate $\hat{\beta}$ is the coefficient vector which minimises :

$$||Y - X\beta||^2 \tag{2.12}$$

admitting the existence of $(X^tX)^{-1}$, $\hat{\beta}$ is then :

$$\hat{\beta} = (X^TX)^{-1}X^tY \tag{2.13}$$

The predicts of the model are then:

$$\hat{Y} = X\hat{\beta} \tag{2.14}$$

In the case of a multiple variable linear model, R^2 is obtained by :

$$R^2 = 1 - \frac{\sum_i^n (\hat{y}_i - \overline{y})^2}{\sum_i^n (y_i - \overline{y})^2} \tag{2.15}$$

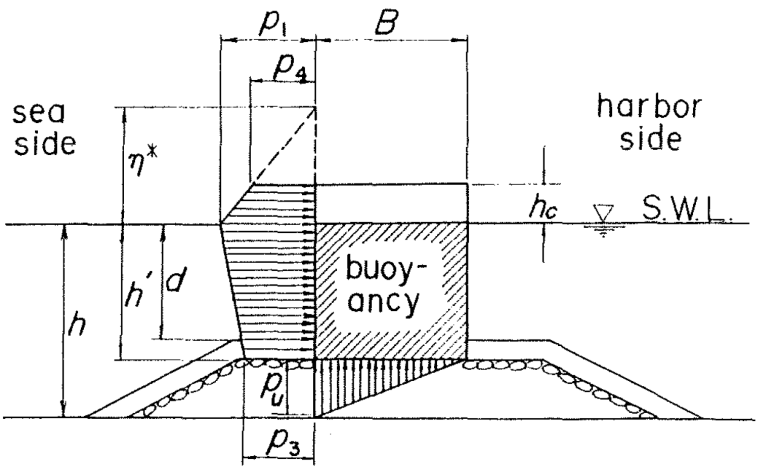

Fig. 4.21 Goda pressure formula

Figure 2.1: Sketch presenting the parameters used in Goda's formula [Takahashi, 2002]

A better estimator of the model quality, taking the number of variables into account is the adjusted R^2 defined as :

$$\overline{R}^2 = 1 - \frac{n-1}{n-(p+1)}(1-R^2) \tag{2.16}$$

with p the number of variable and n the number of observations.

The multilinear regression model is used in chapter 3 to find a relationship between several environmental variables describing waves, water level and wind and the maximal pressure on the wall over a prescribed duration. Non-linear models are then developed in order to better reproduce the effect of some explanatory variables. In this case, functions have to be determined instead of the scalar coefficient β_i. A more detailed description of non linear models is provided in chapter 3.

2.2 Design formula for vertical or composite breakwaters

Goda's formula [Goda, 1975] is the most widely used formula for the design of vertical breakwaters. It was established considering 13 breakwater failure real cases and further, validated in controlled environments. In the literature, there is no acknowledged attempt to compare this formula with field data. The first reason may be that Goda's formula considers a linear pressure distribution generating a static force which should be seen as a conservative envelope of the actual pressure field. The formula also requires the knowledge of the maximal wave height in front of the structure which is not easy to measure. In this thesis, we tried to compare statistically the data obtained at the Artha breakwater with Goda's formula complemented by Takahashi [2002] for the impulsive term in chapter 4.

The procedure to calculate the characteristic pressures represented in figure 2.1 is then the following :

$$\eta^* = 0.75(1+\cos\theta)\lambda_1 H_D \tag{2.17}$$

$$p_1 = 0.5(1 + \cos\theta)(\lambda_1\alpha_1 + \lambda_2\alpha^* \cos^2\theta)w_0 H_D \tag{2.18}$$

$$p_3 = \alpha_3 p_1 \tag{2.19}$$

$$p_4 = \alpha_4 p_1 \tag{2.20}$$

$$p_u = 0.5(1 + cos\theta)\lambda_3\alpha_1\alpha_3 w_0 H_D \tag{2.21}$$

With :

$$\alpha_1 = 0.6 + 0.5\{(4\pi h/L_D)/\sinh(4\pi h/L_D)\}^2 \tag{2.22}$$

$$\alpha^* = max\{\alpha_2, \alpha_I\} \tag{2.23}$$

$$\alpha_2 = min\{(1 - d/h_b)(H_D/d)^2/3, 2d/H_D\} \tag{2.24}$$

$$\alpha_3 = 1 - (h'/h)\{1 - 1/\cosh(2\pi h/L_D)\} \tag{2.25}$$

$$\alpha_4 = 1 - h_c^*/\eta^* \tag{2.26}$$

$$h_c^* = min\{\eta^*, h_c\} \tag{2.27}$$

With :

θ : mean incidence of the waves.
$\lambda_1, \lambda_2, \lambda_3$: modification factors dependent on the structural type.
H_D, L_D : design wave height and wave length.
α_I : impulsive pressure coefficient
w_0 : the specific weight of sea water ($= \rho_0 g$)
h_b : offshore water depth at a distance five time the significant wave height $H_{1/3}$

The impulsive pressure coefficient α_I is determined as :

$$\alpha_I = \alpha_{I0}\alpha_{I1} \tag{2.28}$$

α_{I0} represent the effect of wave height on the mound :

$$\begin{aligned} \alpha_{I0} &= H/d \qquad H \leq 2d \\ &= 2 \qquad H > 2d \end{aligned} \tag{2.29}$$

α_{I1} represent the effect of the mound shape :

$$\begin{aligned} \alpha_{I1} &= \cos\delta_2/\cosh\delta_1 \qquad \delta_2 \leq 0 \\ &= 1/\{\cosh\delta_1(\cosh\delta_2)^{0.5} \qquad \delta_2 > 0 \end{aligned} \tag{2.30}$$

$$\begin{aligned} \delta_1 &= 20\delta_{11} \qquad \delta_{11} \leq 0 \\ &= 15\delta_{11} \qquad \delta_{11} > 0 \end{aligned} \tag{2.31}$$

$$\begin{aligned} \delta_2 &= 4.9\delta_{22} \qquad \delta_{22} \leq 0 \\ &= 3\delta_{22} \qquad \delta_{22} > 0 \end{aligned} \tag{2.32}$$

$$\begin{aligned} \delta_{11} &= 0.93(B_M/L - 0.12) + 0.36\{(h-d)/h - 0.6\} \\ \delta_{22} &= -0.36(B_M/L - 0.12) + 0.93\{(h-d)/h - 0.6\} \end{aligned} \tag{2.33}$$

With B_M the berm width.

The so-called design wave is the highest wave in the design sea state in front of the breakwater [Takahashi, 2002]. In chapter 4, a numerical model is used to determine this parameter.

2.3 Description of the wave field

chapter 4 is devoted to the description of the wave field above the rubble mound just before the impact on the wall. Hereafter, a few methodological complements are given regarding this aspect.

2.3.1 Measuring waves from the bottom pressure signal using linear wave theory

The simplest theory available to describe surface waves is the Airy linear theory.

Under the approximation of an incompressible, non-viscous irrotational flow, the four basic equations to be solved are introduced in Figure 2.2.

- mass conservation (in black on Figure 2.2)
- Kinematic and dynamic free surface boundary condition (in blue on Figure 2.2)
- Bottom boundary condition (in grey on Figure 2.2)

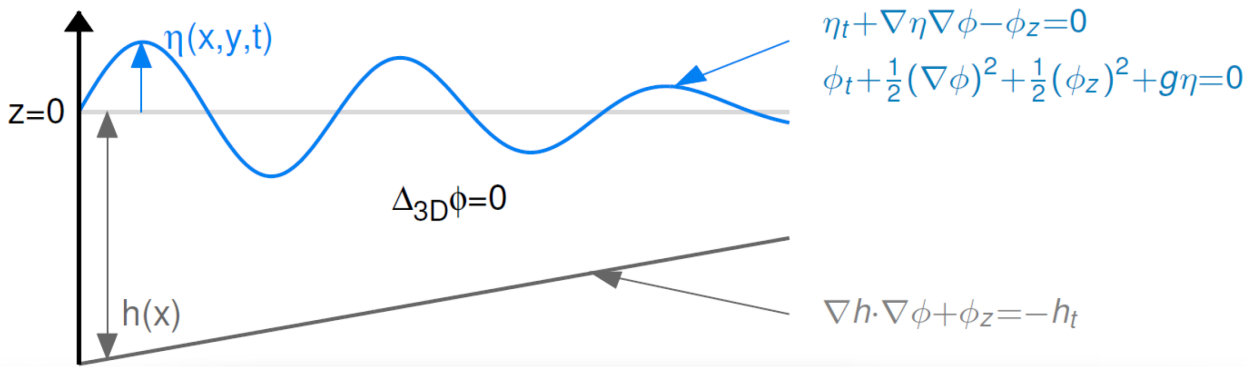

Figure 2.2: Sketch of wave propagating over a linearly varying bathymetry and governing equations

After combining the boundary condition in $z = \eta$ and applying a Taylor development at $z = 0$, we get :

$$\frac{\partial^2\phi}{\partial t^2} + g\frac{\partial\phi}{\partial z} = 0 \qquad z = 0 \tag{2.34}$$

$$\frac{\partial^2\phi}{\partial x^2} + \frac{\partial^2\phi}{\partial z^2} = 0 \qquad -h \leq z \leq \eta \tag{2.35}$$

$$\frac{\partial\phi}{\partial z} = 0 \qquad z = -h \tag{2.36}$$

Searching for periodic solutions of permanent form travelling with a constant celerity $c = \omega/k$ yields the free surface profile :

$$\eta = \frac{A\omega}{g}\cosh(kh)\cos(kx - \omega t) \tag{2.37}$$

Defining the wave amplitude $a = H/2$, gives :

$$\eta = a\cos(kx - \omega t) \tag{2.38}$$

$$A = \frac{ag}{\omega}\frac{1}{\cosh(kh)} \tag{2.39}$$

And the velocity potential for a linear progressive wave is given by :

$$\phi = \frac{ag}{\omega}\frac{\cosh(k(z+h))}{\cosh(kh)}\sin(kx - \omega t) \tag{2.40}$$

The flow velocity components can further be obtained by differentiating this equation with respect to the desired direction (not shown here).

With the free surface boundary condition, the dispersion relation is obtained as :

$$\omega^2 = gk\tanh(kh) \tag{2.41}$$

With k wave number, ω wave frequency and g gravitational acceleration.

Pressure in the water column is obtained by the Bernoulli equation :

$$\frac{p}{\rho} + gz + \frac{\partial \phi}{\partial t} + \frac{(\nabla \phi)^2}{2} = 0 \tag{2.42}$$

The conservation of mass gives $(\nabla \phi)^2 = 0$, replacing ϕ, we get :

$$p = -\rho g z + \rho \frac{gH}{2} \frac{\cosh\left(k(z+h)\right)}{\cosh\left(kh\right)} \cos(kx - \omega t) \tag{2.43}$$

or else :

$$p = -\rho g z + \rho g \eta K_p(z) \tag{2.44}$$

defining the so-called "correction factor" by :

$$K_p(z) = \frac{\cosh\left(k(z+h)\right)}{\cosh\left(kh\right)} \leq 1 \tag{2.45}$$

In chapter 4, we used pressure measurements on the sea bottom to estimate the surface wave field based on this simple theory.

2.4 reflected wave field : the three probes method

In chapter 4, the wave field is composed of incident and reflected waves due to the presence of the breakwater. Hence, the need to separate the two components. The method proposed by Mansard and Funke [1980] is used to that purpose.

The method, based on a least square procedure, requires the knowledge of the spectrum at three points close to each other and on a line parallel to the wave propagation direction and with limited depth variation.

Assuming that incident and reflected waves are travelling in opposite direction along the same axis and that this irregular wave signal is measured at 3 or more points p on that same axis, the wave profile observed at each of those points can be given as a summation of discrete Fourier components :

$$\eta_p(t) = \sum_{k=1}^{N} A_{p,k} \sin(\frac{2\pi k t}{T} + \alpha_{p,k}) \tag{2.46}$$

with $A_{p,k}$ the Fourier coefficient for frequency k/T, T the duration of the observed wave profile, $\alpha_{p,k}$ the phase, N the number of discrete Fourier components.

From the Fourier transform of $\eta_p(t)$, we have the Fourier coefficients and their phase in polar form :

$$B_{p,k} = A_{p,k} e^{i\alpha_{p,k}} \tag{2.47}$$

Or :

$$B_{p,k} = [A_{p,k} \cos(\alpha_{p,k}) + i\alpha_{p,k} \sin(\alpha_{p,k})] \tag{2.48}$$

The general equation for a progressive wave is :

$$\eta_X(t) = \sum_{k=1}^{N} C_k \sin(-\frac{2\pi kt}{T} + \frac{2\pi X}{L_k} + \theta_k) \tag{2.49}$$

With θ_k an arbitrary phase, X the space variable in the direction of wave propagation, L_k the wave length of frequency k/T.

The wave signal observed at each point p can be described as the summation of :

- a) an incident wave $C_{I,k}$,
- b) a reflected wave $C_{R,k}$,
- c) some parasitic noise.

With X_1 the distance from the wave source to probe $p = 1$ and XR_1 the distance from the reflecting structure to probe $p = 1$, the measured wave profile at this location can be written as :

$$\begin{aligned}\eta_{p=1}(t) = &\sum_{k=1}^{N} C_{Ik} \sin(-\frac{2\pi kt}{T} + \frac{2\pi X_1}{L_k} + \theta_k) \\ &+ \sum_{k=1}^{N} C_{Rk} \sin(-\frac{2\pi kt}{T} + \frac{2\pi(X_1 + 2XR_1)}{L_k} + \theta_k + \phi_k) \\ &+ \omega_1(t)\end{aligned} \tag{2.50}$$

With $\omega_1(t)$, the noise at $p = 1$ and ϕ_k, a phase change due to reflection. At probe $p = 2$, at a distance X_{12} from the probes at $p = 1$, the phase angles are now :

$$(-\frac{2\pi kt}{T} + \frac{2\pi(X_1 + X_{12})}{L_k} + \theta_k) \tag{2.51}$$

and

$$(-\frac{2\pi kt}{T} + \frac{2\pi(X_1 + 2XR_1 - X_{12})}{L_k} + \theta_k + \phi_k) \tag{2.52}$$

For the incident and reflected waves respectively.

Similar relations are obtained for each probes p. The Fourier transform of the signal described by 2.50 yields :

$$\begin{aligned}F[\eta_{p=1}(t)] = B_{1,k} = &C_{I,k} \exp(i\frac{2\pi X_1}{L_k} + i\theta_k) \\ &+ C_{R,k} \exp(i\frac{2\pi(X_1 + 2XR_1)}{L_k} + i(\theta_k + \phi_k)) \\ &+ Y_{1,k} \exp(i\rho_{1,k})\end{aligned} \tag{2.53}$$

Similarly at other probes p, we get :

$$F[\eta_p(t)] = B_{p,k} = C_{I,k}\exp(i\frac{2\pi(X_1+X_{1P}}{L_k} + i\theta_k) + C_{R,k}\exp(i\frac{2\pi(X_1+2XR_1-X_{1P})}{L_k} + i(\theta_k+\phi_k)) + Y_{1,k}\exp(i\rho_{p,k}) \quad (2.54)$$

As we are only interested in the phase difference between the probes, thus :

$$Z_{I,k} = C_{I,k}\exp(i\frac{2\pi X1}{L_k} + i\theta_k) \quad (2.55)$$

$$Z_{R,k} = C_{R,k}\exp(i\frac{2\pi(X_1+2XR_1)}{L_k} + i(\theta_k+\phi_K)) \quad (2.56)$$

$$Z_{N,p,k} = Y_{p,k}\exp(i(\rho_{p,k}) \quad (2.57)$$

And therefore :

$$B_{1,k} = Z_{I,k} + Z_{R,k} + Z_{N,1,k} \quad (2.58)$$

$$B_{2,k} = Z_{I,k}\exp(i\frac{2\pi X_{12}}{L_k}) + Z_{R,k}\exp(-i\frac{2\pi X_{12}}{L_k}) + Z_{N,2,k} \quad (2.59)$$

$$B_{3,k} = Z_{I,k}\exp(i\frac{2\pi X_{13}}{L_k}) + Z_{R,k}\exp(-i\frac{2\pi X_{13}}{L_k}) + Z_{N,3,k} \quad (2.60)$$

A least square method is employed to find the Z_I and Z_R that minimise Z_N :

$$\psi_{p,k} = \frac{2\pi X_{1P}}{L_k} \quad (2.61)$$

and

$$\beta_k = \psi_{2,k} = \frac{2\pi X_{12}}{L_k} \quad (2.62)$$

$$\gamma_k = \psi_{3,k} = \frac{2\pi X_{13}}{L_k} \quad (2.63)$$

We can now note :

$$Z_{I,k} + Z_{R,k} - B_{1,k} \approx \epsilon_{1,k} \quad (2.64)$$

$$Z_{I,k}\exp^{i\beta_k} + Z_{R,k}\exp^{-i\beta_k} - B_{2,k} \approx \epsilon_{2,k} \quad (2.65)$$

$$Z_{I,k}\exp^{i\gamma_k} + Z_{R,k}\exp^{-i\gamma_k} - B_{3,k} \approx \epsilon_{3,k} \quad (2.66)$$

where :

$$\epsilon_{p,k} = -Z_{N,p,k} + f_e(Z_{I,k}, Z_{R,k}) \tag{2.67}$$

the least square method allows to find the values of Z_I and Z_R that minimise $\sum_{p=1}^{N} \epsilon_{p,k}^2$.
This minimum is reached when :

$$\frac{\partial(\sum_{p=1}^{3}(\epsilon_{p,k}^2))}{\partial Z_{I,k}} = \frac{\partial(\sum_{p=1}^{3}(\epsilon_{p,k}^2))}{\partial Z_{R,k}} = 0 \tag{2.68}$$

Which yields :

$$\sum_{p=1}^{3}(Z_{I,k}e^{i\psi_{p,k}} + Z_{R,k}e^{-i\psi_{p,k}} - B_{p,k})e^{i\psi_{p,k}} = 0 \tag{2.69}$$

and

$$\sum_{p=1}^{3}(Z_{I,k}e^{i\psi_{p,k}} + Z_{R,k}e^{-i\psi_{p,k}} - B_{p,k})e^{-i\psi_{p,k}} = 0 \tag{2.70}$$

Developing the summation we have :

$$Z_{I,k}(1 + e^{i2\beta_k} + e^{i2\gamma_k}) + 3Z_{R,k} = B_{1,k} + B_{2,k}e^{i\beta_k} + B_{3,k}e^{i\gamma_k} \tag{2.71}$$

$$Z_{R,k}(1 + e^{-i2\beta_k} + e^{-i2\gamma_k}) + 3Z_{I,k} = B_{1,k} + B_{2,k}e^{-i\beta_k} + B_{3,k}e^{-i\gamma_k} \tag{2.72}$$

Finally the solution is :

$$Z_{I,k} = \frac{1}{D_k}(B_{1,k}(R_1 + iQ_1) + B_{2,k}(R_2 + iQ_2) + B_{3,k}(R_3 + iQ_3)) \tag{2.73}$$

and

$$Z_{R,k} = \frac{1}{D_k}(B_{1,k}(R1 - iQ1) + B_{2,k}(R2 - iQ2) + B_{3,k}(R3 - iQ3)) \tag{2.74}$$

With :

$$D_k = 2(\sin\beta_k{}^2 + \sin\gamma_k{}^2 + \sin\gamma_k - \beta_k{}^2) \tag{2.75}$$

$$R1_k = \sin\beta_k{}^2 + \sin\gamma_k{}^2 \tag{2.76}$$

$$Q1_k = \sin\beta_k \cos\beta_k + \sin\gamma_k \cos\gamma_k \tag{2.77}$$

$$R2_k = \sin\gamma_k \sin\gamma_k - \beta_k \tag{2.78}$$

$$Q2_k = \sin\gamma_k \cos\gamma_k - \beta_k - 2\sin\beta_k \tag{2.79}$$

$$R3_k = -\sin\beta_k \sin\gamma_k - \beta_k \tag{2.80}$$

$$Q3_k = \sin\beta_k \cos\gamma_k - \beta_k - 2\sin\gamma_k \tag{2.81}$$

Solving this for the k frequencies allows to reconstruct the incident and reflected spectrum.

2.5 Composition on incident and reflected waves

When a sinusoidal surface wave meets an obstacle, the reflected wave leads to the formation of a stationary wave. The mathematical description of this stationary wave is described hereafter as a very simple illustration of what is observed in chapter 4.

We consider an incident and a reflected sinusoidal surface wave of the following respective form :

$$\eta_i = a_i \cos(\omega t - kx) \tag{2.82}$$

$$\eta_r = a_r \cos(\omega t + kx + \beta) \tag{2.83}$$

With β the phase shift of the reflected wave.

The free surface is therefore described as :

$$\eta = a_i \cos(\omega t - kx) + Ra_i \cos(\omega t - kx) \tag{2.84}$$

With R the reflection coefficient. As shown in section 2.3.1, the free surface can also be expressed as :

$$\eta = A(x)cos(\omega t - kx) \tag{2.85}$$

Which gives in exponential form :

$$A(x)e^{i(\omega t - kx)} = a_i e^{i(\omega t - kx)} + Ra_i e^{i(\omega t + kx + \beta)} \tag{2.86}$$

so :

$$A(x) = a_i + Ra_i e^{i(2kx+\beta)} \tag{2.87}$$

The real part of this equation is :

$$A(x) = a_i + Ra_i \cos(2kx + \beta) \tag{2.88}$$

This is the equation of a stationary wave. This phenomena is observed in chapter 4, but the result is made more complex by the presence of the multiple frequencies present in the sea state considered.

Chapter 3

In-situ measurements of wave impact pressure on a composite breakwater submitted to high wave energy: data analysis and influence of the environmental variables

Contents

3.1 Introduction

Wave impacts have been early identified as one of the main sources for composite breakwater failure (e.g., Takahashi [2002]) and were therefore extensively studied since the beginning of the 20th century.

Very briefly, Sainflou [1928], then Rouville et al. [1938], identified the existence of different types of impacts. In 1939,Bagnold [1939] proposed a model for wave breaking impacts on vertical walls, based on air entrapment between the wave face and the wall later revised by Mitsuyasu [1966]. Numerical studies and wave flume experiments have since been conducted by Lugni et al. [2006], Peregrine [2003], Brosset et al. [2011], Scolan [2010] among others. All these studies show the complexity of the phenomenon, mixing compressible and incompressible processes Wagner [1932]. There is indeed a strong influence of the water/air interface shape at impact. This is highlighted by the so-called flip-through impact Cooker and Peregrine [1991]. This particular impact, which lies at the limit between a non-breaking wave run-up and a wave impact with air entrapped, is known to generate a sharp, very intense and localised pressure peak. The maximum pressure generated by a breaking wave on a wall is therefore very dependent on local scale processes and as a result, very difficult to predict.

On the other hand, on the practical side, there is a need for an accurate determination of the critical load due to waves on coastal and marine structures. Nevertheless, owing to the inherent difficulty of the impact phenomenon, the complexity of real structures as well as of the surrounding environment, this design load determination still largely relies on physical tests, which have to be conducted for each different projects and on empirical formula (e.g., Goda [1975], Takahashi [2002]). The latter integrates many complex processes in a supposedly conservative way. Therefore, the gap between the extensive knowledge of the physical processes involved (waves, impact, etc.) and the engineering application of this knowledge appears significant.

To reduce this gap, one of the ideas could be to collect and analyse extensive field data Oumeraci et al. [2001]. There are indeed significant differences between lab and field conditions, for instance illustrated by maximum pressure values in both environments. For instance, Hofland et al. [2011], Bullock et al. [2007] and Brosset et al. [2011] recorded impacts with maximal pressures of 27, 30 and 56 bar in wave flumes, respectively. These values are much larger than the 7.45 bar maximum impact pressure recorded in-situ by Bullock et al. [2005]. Peregrine [2003] identified a few factors likely to damp maximum impact pressure in natural conditions compared to ideal impacts in wave flume or numerical models. In particular, the three dimensional effects inherent to real waves as well as the breakwater block armour units are likely to diminish impact pressure. Aeration processes, different in fresh and salted waters, and scaling in general make it also difficult to compare flume and field measurements Bullock et al. [2001], Bredmose et al. [2009, 2015], Plumerault et al. [2012]. On the other hand, Peregrine [2003] also mentioned that bathymetric wave focusing could conversely increase impact pressure in some particular case.

Unfortunately, the amount of wave impact pressure field data appears quite limited due to the difficulty to perform accurate and long term measurements in this extreme environment Rouville et al. [1938] is one of the most complete measurement campaign conducted with various types of impact and the detection of remarkable events thanks to the piezo-resistive sensors. Note that a few earlier attempts are also reported in Blackmore and Hewson [1984] but using non-suitable pressure sensors. In the three years Dieppe field campaign, offshore significant wave heights ranged between 1.5 m and 2.5 m offshore, and the maximum estimated breaking wave height reached about 3.5m in front of the structure. Wavelength and water level were also recorded. Blackmore and Hewson [1984] conducted in-situ wave impact measurements at the Ilfracombe breakwater which resulted in 112 impacts of less than 0.48 bar. Within the framework of the PROVERB project (probabilistic design tools for vertical breakwaters), Bullock G. et al. [2004] carried out extensive wave impact measurements at the Alderney breakwater. They used a specifically designed sensor to record both pressure and aeration. In that study, the maximal recorded pressure was 3.37 bar at 6.2 m

(Chart Datum) with weaker values at higher levels. Significant wave heights up to 3.1 m were reported. More recently, at the Artha breakwater, in a preliminary campaign of four months involving two sensors, (against sixteen in the present study), Larroque et al. [2018] measured up to 2.5 bar in very energetic wave conditions (i.e., significant wave height $H_s = 5.5$ m) while, interestingly, the maximum pressure (i.e. 2.7 bar) was reached under more moderate wave conditions (i.e., $H_s = 2.2$ m). The significant influence of the water level was also pointed out.

The link between field wave impact pressures and environmental explanatory variables such as waves and water level, while obviously worth investigating, appears significantly understudied in the literature. This is surprising as a better knowledge in this direction could help improving the accuracy of the current empirical design formulas. Hence, for instance, Goda [1975] and Takahashi [2002] used to calculate the design load, a "design wave", assumed to be the largest wave in the design sea-state at the toe of the structure Goda [1988, 1975], Oumeraci et al. [2001]. More specifically, these formulas accept the design wave height, length and incident angle as input parameters among other ones (such as the geometrical parameters, etc.). In the field, the situation is more complex than in the laboratory, water level for instance interacting with the wave field, and therefore with the pressure distribution on the structure. Regarding this aspect, the PROVERB project Oumeraci et al. [2001], Kortenhaus and Oumeraci [1999], again, proposed a classification of impact types depending on the breakwater dimensions, wave height and water-level illustrating this strong link. Wind is also likely to play a role in the phenomenon for instance by slightly shaping the wave which may finally influence the local pressure field. Finally, Salvadori et al. [2013] stress the importance of the coupled influence of parameters on the critical load requiring a multivariate analysis to be relevant.

Nevertheless, so far, the relationship between impact pressure and environmental explanatory variables and the coupled influence of the parameters have never been studied or documented. In that context and in the lineage of Rouville et al. [1938], Blackmore and Hewson [1984], Bullock G. et al. [2004], we propose in this paper, high-frequency wave impact pressure measurements conducted at the Artha breakwater in Saint Jean de Luz Bay, south-west of France. Additionally, input data such as significant wave height, significant period, mean swell direction, water level, wind speed and wind direction were simultaneously collected and added to the pressure data to form an extensive dataset suitable for a statistical analysis.

In the first part of the article, the method employed for the measurements and the statistical models will be described. Then the results will be presented and finally, the discussion addresses several aspects of the problem.

3.2 Method

3.2.1 Presentation of the experiment

Configuration of the site

This work considers wave impact pressure measurements at the Artha breakwater in St-Jean de Luz, french basque coast, France (Figure 3.1). The Artha breakwater was built between 1872 and 1895 to protect the towns of St-Jean de Luz and Ciboure from flooding and erosion. The coastal structure was erected on an existing natural reef, where numerous concrete blocks were immersed, to create a high and stable bedrock. A large central caisson, made up of a mix of concrete and stones, surrounded by a concrete berm was then built

Figure 3.1: Geographical position of the experiment (red dot). The main swell direction from north-west is indicated

on that foundation. An armour, made of more than 20000, 50 tonnes, cuboid, $4 \times 2.5 \times 2\,m^3$ concrete blocks, defends the structure. This protection is key to the durability of the caisson. The recurring displacement of blocks by the waves requires to add about 30 concrete elements every year. Despite these maintenance operations, repairs of the masonry are frequently required.

A directional wave buoy (Figure 3.2), part of the national CANDHIS network `http://candhis.cetmef.developpement-durable.gouv.fr/`, provides swell measurements 1 km offshore of the breakwater, in 20 m deep. The Socoa tide gauge is located within the bay of Saint Jean de Luz, less than 1 km from the pressure sensors. Socoa semaphore is another 1km away and provides wind data.

The pressure sensors are located on the offshore facing side of the caisson, at the western roundhead (Figures 3.2, 3.3, 3.5) on the most exposed location. This position was determined based on observations of damages and climatology of swell parameters measured at the buoy.

Wave climate and tides

Kergadallan et al. [2020] provides an overview of the statistical characteristics of the wave climate based on a little more than 5 years of measurements. The average climate is characterized by a quantile 50% of 1.28 m and 80% of 2.32 m for the spectral significant wave height H_{m0} (respectively 1.78 m and 2.95 m in winter)

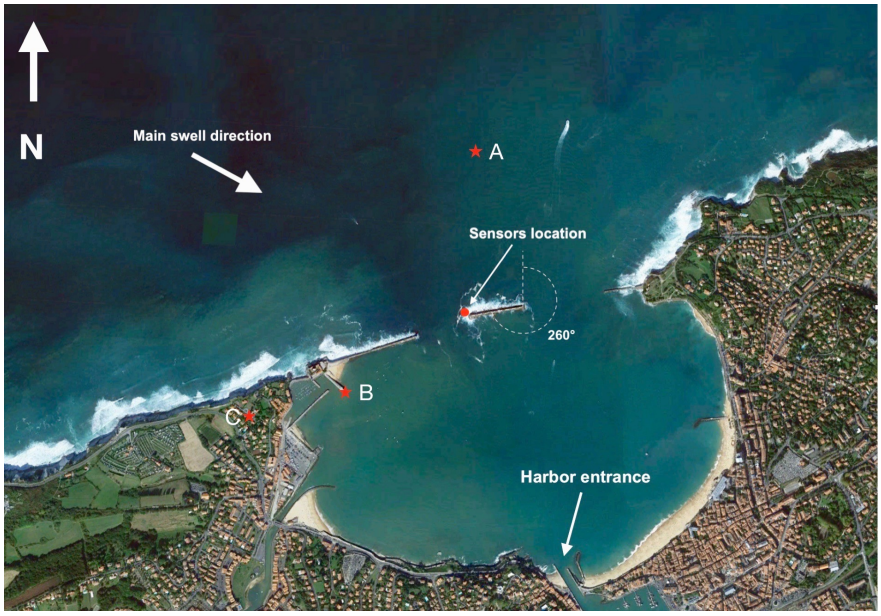

Figure 3.2: Aerial view of the bay of St-Jean de Luz. The location of the sensors on the breakwater is indicated by a red dot. The red stars correspond to (A): The directional wave buoy, (B): Socoa tide gauge, (C): Socoa Semaphore. Source: Google earth V 7.3.2.5776. (2019/03/05). St-Jean-De-Luz, France. 43°23' 53"N, 1°40' 27"W, Eye alt 4km. Maxar Technologies 2020.

with an associated peak period T_p between 10 and 12 s (respectively 11 and 13 s). The 5-year return level of the significant wave height is between 7.13 and 8.43 m depending on the fitting law chosen (respectively 7.25 - 9.05 m and 7.34 - 9.66 m for the 10-year and 20-year values). The peak direction of storm waves is predominantly west-north-west, with some events also reported from north-north-west. The tidal regime is mesotidal with 4.5 m spring tidal range around a mean water level of 2.64 m (C.D.).

Load expected at the Artha breakwater

The PROVERB classification (Figure 3.4) provides the shape of the load expected for a specific breakwater depending on three parameters :$h_b^* = h_b/h_s$, $H_s^* = H_{si}/h_s$, $B^* = B_{eq}/L_{pi}$, with h_s the depth at the toe of the breakwater, h_b the vertical distance from the toe to the berm, B_b the width of the berm, H_{si} and L_{pi} the wave height and length at depth h_s and $B_{eq} = B_b + h_b/2tan(\alpha)$.

To determine the category in the PROVERB classification, to which the Artha breakwater belongs, the geometrical characteristics of the structure as well as the water level matter. Figure 3.5 shows two cross-sections of the Artha breakwater. The caisson lies on a mound made up of concrete blocks and is protected by a berm concrete element of rectangular section (Figure 3.5 (a)). As illustrated in this figure, depending on the section considered, the bottom profile can be slightly different. According to this, we may consider the berm level as varying between rubble mound height, which, in Figure 3.5 (a), is approximately at the lowest Astronomical Tide Level, and the top part of the rectangular concrete protective element as in Figure 3.5 (b). Accordingly, h_b ranges between 15 and 18 m. Let us consider for the sake of clarity an intermediate value of 16.5 m. Then, considering the tide amplitude, h_s ranges approximately between 14.5 m and 19.5 m (Figure 3.5 (b)) leading to h_b^* varying from ≈ 0.85 for very high water levels to ≈ 1.13 for very low water

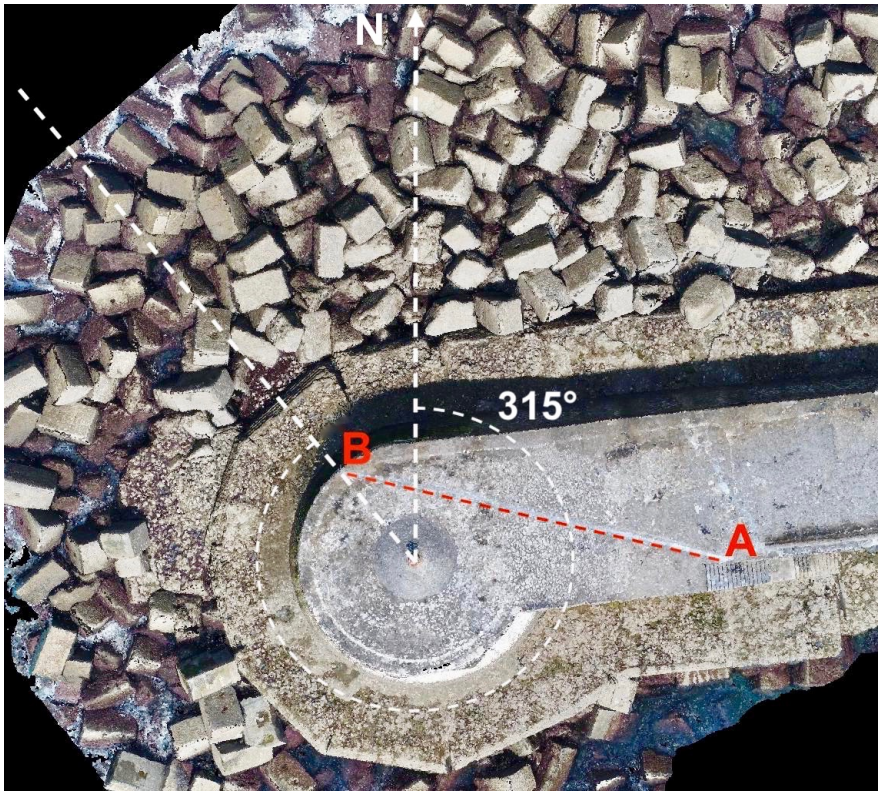

Figure 3.3: Ortho-photograph of the Artha breakwater western roundhead. (A) : Acquisition station (B) Sensor location. The trench connecting the sensor to the acquisition station is visible along the red dashed line. The azimuth of the sensors to roundhead center axis is indicated. source: LP GEO 3D - Lycée Cantau / C. Bagieu

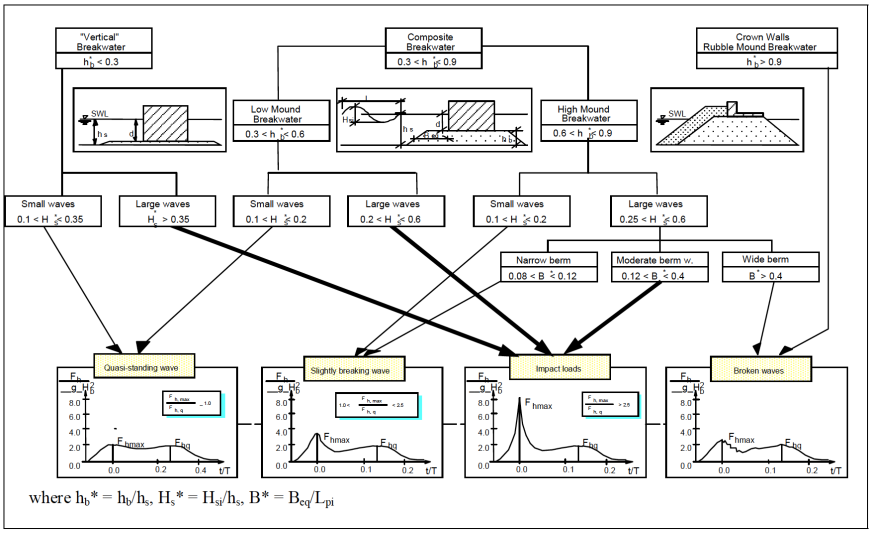

Figure 3.4: Typology of impacts in function of the breakwater type and geometry and waves and water level conditions. Source : PROVERB project chapter 2.2 [Oumeraci et al., 2001]

levels. Therefore, for low to intermediate water level, the Artha breakwater is considered as a crown wall rubble mound breakwater or equivalently, all the waves break before reaching the wall. In this situation, the load is likely to resemble the one depicted on the right panel (referred as to broken waves in Figure 3.4). At very high water levels, the breakwater works as a composite breakwater and the load consequently depends on several other parameters. h_b^* being larger than 0.6, the breakwater is considered as a high mound breakwater. Small waves (i.e., $H_s^* < 0.2$), which represent a maximum H_s of $\approx$ 3-4 m, are supposed to generate slosh impact or slightly breaking wave impact as in the second panel of Figure 3.4. For larger waves, (say, $H_s > 5m$) the relative berm B^* has to be calculated. For large waves like this, periods between 15 and 17 s are expected in Saint Jean de Luz [Kergadallan et al., 2020]. The calculation shows that the breakwater falls in the moderate berm category for which impulsive (impact loads in Figure 3.4) load are likely to occur.

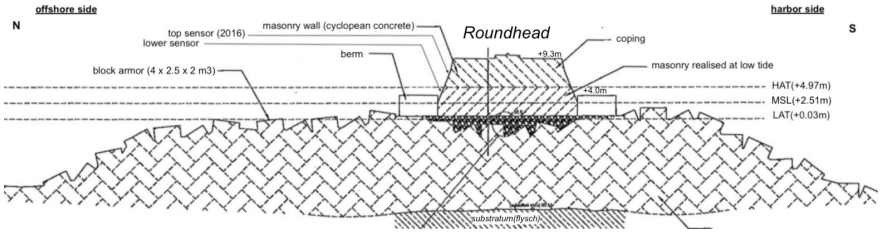

(a)

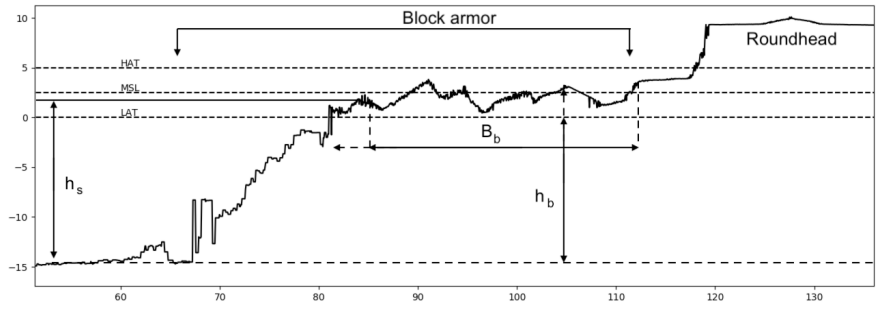

(b)

Figure 3.5: (a) Schematic cross section of the Artha breakwater roundhead perpendicular to the structure trunk. The main structural elements are mentioned as well as the position of the sensors during the 2016 campaign (b) Bottom level measured in a cross section of the Artha breakwater western roundhead along the axis passing by the lower sensor and the centre of the roundhead. Altimetry is in chart-datum.

Sensors and acquisition station

To achieve high-frequency measurement in marine grade conditions, piezo-resistive sensors with a natural frequency of 1 kHz and IP68 protection rating were selected.

A data acquisition station is installed on the protected side of the breakwater, in a dedicated chamber. It is connected to the sensors by a trench of more than 30 m, on the top of the roundhead, as seen in Figure 3.3. The isolated nature of the site implies to use a flexible and remotely programmable data acquisition system. To that end, a CompactRIO 9076 from National Instruments© was deployed. With a 16 bit encoding, the digitization precision is way below the accuracy of the sensors. The acquisition frequency of 10 kHz was

selected with respect to the Shannon–Hartley theorem [Shannon, 1949]. To download the data and modify the recording parameters if needed, a wireless system is used to communicate with the data acquisition station. To ensure the durability of the measurements, the installation is powered by a photovoltaic panel and a high capacity battery with a solar charge controller. This set up allows measurements of wave impact over extended periods.

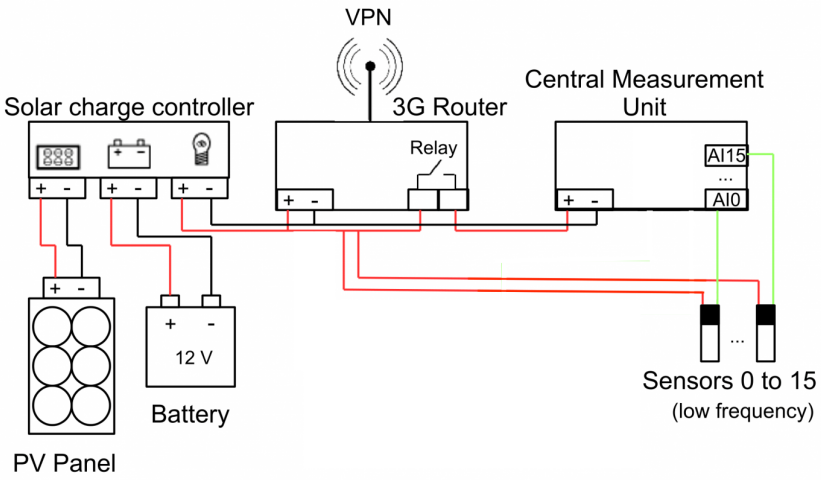

Figure 3.6: Schematic description of the hardware used for the measurements

A preliminary campaign with two sensors vertically distant of 1.85 m was first performed in 2015-2016 [Larroque et al., 2018]. In 2018, the installation was upgraded with 15 new sensors while the upper sensor of 2016 was removed. This provides a set of 16 sensors including the lower sensor of 2016. The two set-ups are presented in Figures 3.7 and 3.8.

3.2.2 Data overview

Wave impact pressure data

The procedure of pressure acquisition and post-processing is described in detail in Damico et al. [2020]. The acquisition station records wave impact pressure hourly in 10 minutes burst, with a sampling frequency $Fe = 10240$ Hz. An embedded threshold, just higher than the atmospheric pressure, allows to save only significant signals. With this threshold, approximately 300 to 400 bursts of 10 minutes are obtained every month. For each sensor, the maximal pressure observed over the 10 minutes burst, provides an observation of P_{max}, our variable of interest or response variable. P_{max} is given after removing the offset due to atmospheric pressure.

The preliminary campaign carried out in 2015-2016 winter lasted four months, yielding 461 observations. In 2018-2019, the first successful tests were conducted in June and the main campaign extended from October 2018 to April 2019. A malfunction shut the station down between the 2018/12/07 and 2019/01/17, period

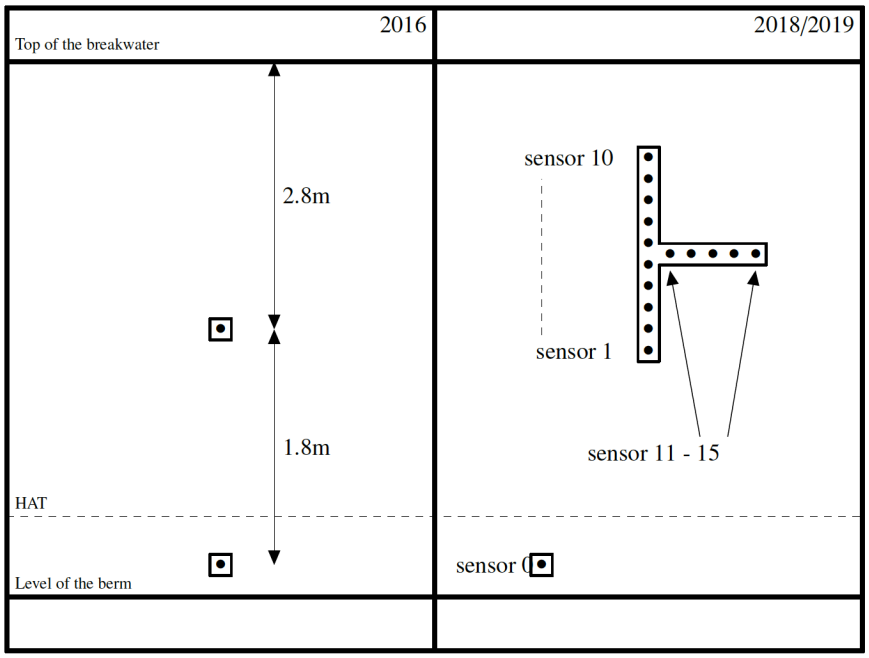

Figure 3.7: Disposition of the sensors for both campaigns with the level of the berm, the level of the Highest Astronomical Tide

(a) (b)

Figure 3.8: picture of the sensors in (a) the 2016 campaign (b) the 2018-2019 campaign.

during which, the waves conditions were mostly moderate. Overall, this second campaign resulted in 1390 observations.

The network of 16 sensors used during the campaign of 2018-2019 aims at giving an insight on the pressure spatial distribution.

The spatial distribution is also used to evaluate the force by linear meter exerted on the wall. The calculation is made by integrating the instantaneous vertical distribution of pressure using a trapezoidal integration rule assuming pressure linearity between sensors. The linear profile is extended up to the top and down to the bottom to obtain the full force. Note that with the trapezoidal integration rule, sensor 0 has a major weight in the determination of the force as $z_1 - z_0 = 1.9$ m while the next $\Delta z = 0.2$ m.

Finally, bursts have been automatically processed in Damico et al. [2020] identifying 152999 impacts overall in 2018-2019. This allowed to analyse the link between the maximal force and pressure by impact and relate it to the sea state parameters.

External explanatory variables

The variable of interest is studied in the light of the following six external explanatory parameters, whose measurement location is indicated in Figure 3.2 :

- $H_{1/3}$: Significant wave height determined as the mean of the highest third of waves measured over 30 minutes, every hour, at the buoy A,
- $T_{1/3}$: Significant wave period determined as the mean of the highest third of waves period measured over 30 minutes, every hour in A,
- θ : Mean swell direction, determined from 30 minutes of observation, every hour in A,
- wl : water level as measured in B at the time of the burst, hourly,
- ws : mean wind speed over 10 minutes as measured at C every hour,
- wd : mean wind direction over 10 minutes as measured at C every hour

3.2.3 Statistical models

Linear model

The relationship between the environmental explanatory variables and the response variable P_{max} is studied with the following multiple linear regression :

$$P_{max_i} = \beta_0 + \beta_1 H_{1/3_i} + \beta_2 T_{1/3_i} + \beta_3 \theta_i + \beta_4 wl_i + \beta_5 ws_i + \beta_6 wd_i + \epsilon_i \tag{3.1}$$

At each time stamp i, the observation of P_{max} is expressed in function of the i-th explanatory variables observation, plus a residual ϵ_i. The β_j linear coefficients associated to the explanatory variables are estimated using a least square method.

Wave parameters, such as wave height and wave period, are likely to be correlated. We may also assume that wave height may, for instance, be affected by water level. Therefore, generally speaking, a correlation between the variables can exist. In this case, the relative importance of each variable is not

the determination coefficient (R^2) of the corresponding univariate regression and another method has to be employed to determine the variability share accountable for each variable. By averaging the variable importance over all the ordered combinations of variables, the so-called LMG metrics [Lindeman RH, 2006, Groemping, 2006] determines the share of variability attributable to each variable. In parallel, the colinearity between variables has to be checked to ensure that it is low enough to be acceptable for a linear model. For that purpose, the Variance Inflation Factor [Rawlings et al., 2001] is employed. A VIF below a threshold of 3 is usually accepted (see Cenfetelli and Bassellier [2009], Kline [2015], Hair [2011]).

Based on Equation 3.1, all the six explanatory variables are assumed to affect the response variable (i.e., the 10-min maximum wave impact pressure). Nevertheless, this influence may be very weak depending on the variable considered. Therefore, we first tested the null hypothesis $\beta_j = 0$, considering the variables for which $p - value > 0.05$ as likely insignificant. Then, based on the share of variability, estimated with LMG and this $p - value$, the least significant variables in the model were identified. A new model is fitted afterwards by removing them. The improvement achieved with this new model is evaluated with two indicators: the adjusted R^2, a measure of the explained variability, and the Akaike Information Criterion [Akaike, 1998], an estimator of the model quality. Both indicators take the actual number of variables into account and are therefore suited to compare the initial and reduced model.

GAM models

The statistical model, studied in this paper, is essentially a black box, which calculates the maximal pressure from the knowledge of wave integrated parameters in 20 m depth and other variables such as local water level and wind conditions. As a result, this model involves complex physical processes such as wave propagation, wave breaking, wave impact, etc., which are essentially non linear. Hence, the use of a nonlinear model, here the General Additive Models Hastie [2017] based on the following equation :

$$P_{max_i} = f_1(H_{1/3_i}) + f_2(T_{1/3_i}) + f_3(\theta_i) + f_4(wl_i) + f_5(ws_i) + f_6(wd_i) + \epsilon_i \tag{3.2}$$

In Equation 3.2, the functions $f_j()$ are spline functions, determined by the thin plate regression Wood [2003] with no specific degree of liberty *a priori* imposed.

With nonlinear models, the share of variability can no longer be estimated with partial R^2. Instead, we used a non-parametric extension of R^2 [Williamson et al., 2017]. The significance of each variable is also evaluated. As for linear models, only terms with a $p - value < 0.05$ are considered as significant. Based on these two indicators, the least significant variables are removed and a new GAM model is fitted. The improvement of the new model is tested with the Generalized Cross-Validation indicator [Golub et al., 1979]. The global adjusted R^2 is also considered.

In the linear model, the interaction between two explanatory variables can be represented by a plan in the space defined by the two variables and the response variable P_{max}. In non-linear models, variable interactions can be considered at different level of complexity. Here, for the sake of clarity, we only modelled the interactions of two explanatory variables leading to :

$$P_{max_i} = f_1(H_{1/3_i}) + f_2(T_{1/3_i}) + f_3(\theta_i) + f_4(wl_i) + f_5(ws_i) + f_6(wd_i) + f_{1,2}(H_{1/3_i}, T_{1/3_i}) + f_{1,3}(H_{1/3_i}, \theta_i) + f_{1,4}(H_{1/3_i}, wl_i) + f_{1,5}(H_{1/3_i}, ws_i) + f_{1,6}(H_{1/3_i}, wd_i) + f_{2,3}(T_{1/3_i}, \theta_i) + f_{2,4}(T_{1/3_i}, wl_i) + f_{2,5}(T_{1/3_i}, ws_i) + f_{2,6}(T_{1/3_i}, wd_i) + f_{3,4}(\theta_i, wl_i) + f_{3,5}(\theta_i, ws_i) + f_{3,6}(\theta_i, wd_i) + f_{4,5}(wl_i, ws_i) + f_{4,6}(wl_i, wd_i) + f_{5,6}(ws_i, wd_i) + \epsilon_i \quad (3.3)$$

The splines are now determined with a tensor product regression method [Wood, 2006]. The $p - value$ is used to remove the least significant functions and a reduced model is fitted as previously, and evaluated by the GCV and adjusted R^2.

Rise time and pressure impulse

Rise times and the impulse pressures statistics computed from the data of the 2018/2019 measurements campaign are also briefly analyzed in this paper. The rise time rt is defined as the time between the beginning of the impact and the pressure peak for the highest pressure recorded in the burst. Pressure impulse, which corresponds to the integral of pressure in time during impact is here approximated by $2 \times rt \times P_{max}$. Likewise, a multivariate analysis is conducted on those two variables of interest using the same explanatory variables.

3.3 Results

3.3.1 Data analysis

Response variable

The distribution of P_{max} at sensor 0 is presented in Figure 3.10. The majority of impacts is below 1 bar. Only 7 impacts are in the range 2 to 3 bar. Among those 7 impacts, 4 happened during the same storm, in the night of the 2016/02/09. Only one of these P_{max} was recorded at the upper sensor P1 (see Figure 3.7 left), the 2016/02/09/ at 4 am. The 2019/01/21 at 4 am an impact of 4.47 bar was recorded at sensor P0 in moderate wave and wind conditions (i.e., $H_{1/3} = 1.5$ m, $T_{1/3} = 8.2$ s, $ws = 4.6\, m.s^{-1}$, $wl = 4.39$ m). This value is one of the largest reported in the literature for field studies, after 6.9 bar reported in Rouville et al. [1938] at Dieppe in 1938 and 7.45 bar reported by Bullock et al. [2005] at Alderney in 2004.

On Figure 3.10 the distributions of the maximal pressure recorded at sensors 0, 1 and 10 are presented. Burst where $P_{max} = 0$ are excluded for each sensor. Therefore, the number of observations decreases from sensor 0 to sensor 10, meaning that the higher sensors are often untouched while lower sensors record wave impacts. Sensor 0 recorded most of the impacts with several larger than 1 bar. At higher positions (i.e., sensors 1 and 10), impacts of more than 1 bar are very rare.

The vertical distribution of the mean value of the response variable is presented in Figure 3.11 (a). Overall, we observe a roughly linear decrease with elevation with a maximum at P_0. The horizontal distribution in

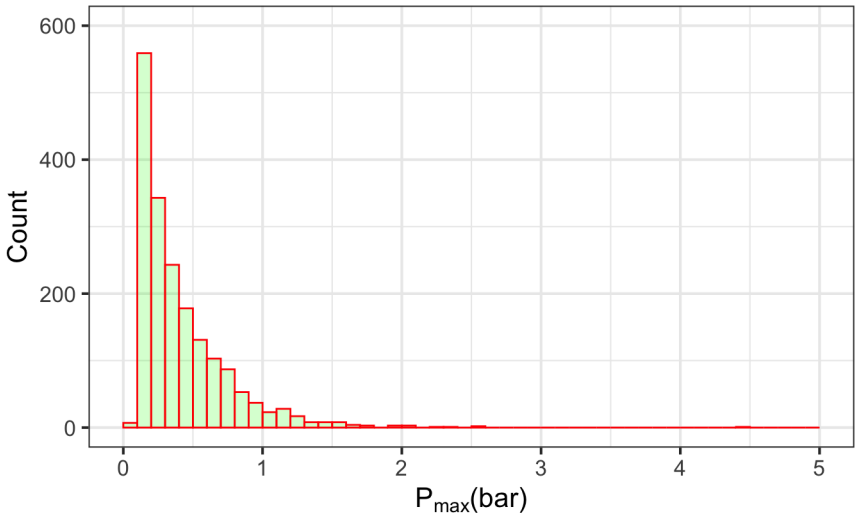

Figure 3.9: Histogram of P_{max} at sensor 0 over both measurement campaigns

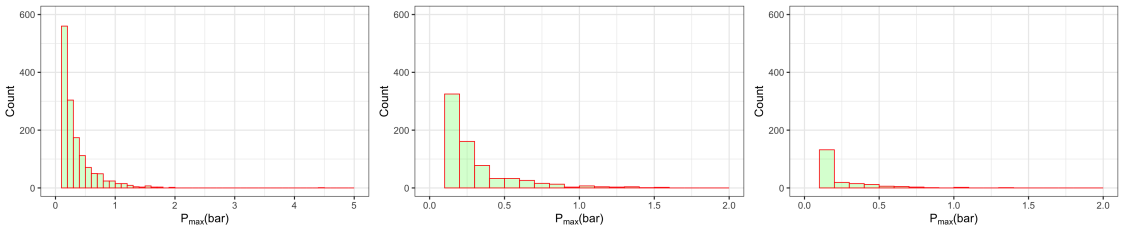

(a) (b) (c)

Figure 3.10: Histogram of P_{max} based on the observations of the 2018-2019 campaign : (a) sensor #0, (b) sensor #1, (c) sensor #10

Figure 3.11 (b) also shows a slight increase of the mean maximum pressure while moving away from sensor P_5.

Examples of pressure signals are presented in Figure 3.12, illustrating two recurrent signal patterns observed in this experiment. In (a), many strong impacts can be observed in groups, while in (b), only one major impact is recorded. The 2016/02/09 (Figure 3.12 (a)) was a particularly energetic storm with significant wave heights up to 7.5 m, water level up to 4.6 m and wind speed up to 21 $m.s^{-1}$. On the other hand, the 2016/03/11 (Figure 3.12 (b)), a significant wave heights of 2.1m, a water-level of 4.8m and wind speed of 1.6 $m.s^{-1}$ were recorded.

In the zoom windows, Figures 3.12 (c) and (d), two types of impact can be distinguished. The five impacts in (c) have similar pressure signature, with a relatively rapid rise followed by a slower decrease, a stabilisation at relatively high value before going back to zero. In (d), a very sharp peak with a very rapid rise and fall is followed by a low steady pressure value before going back to zero. To compare the different impacts, the ratio of pressure peak to quasi-steady level can be used. This ratio was determined for 81 impacts of more than 1 bar from the 2016 database (Figure 3.7). Most impacts are similar to the one presented in Figure 3.12(c), and the mean ratio is 1.66 with a standard deviation of 26%. Among these 81

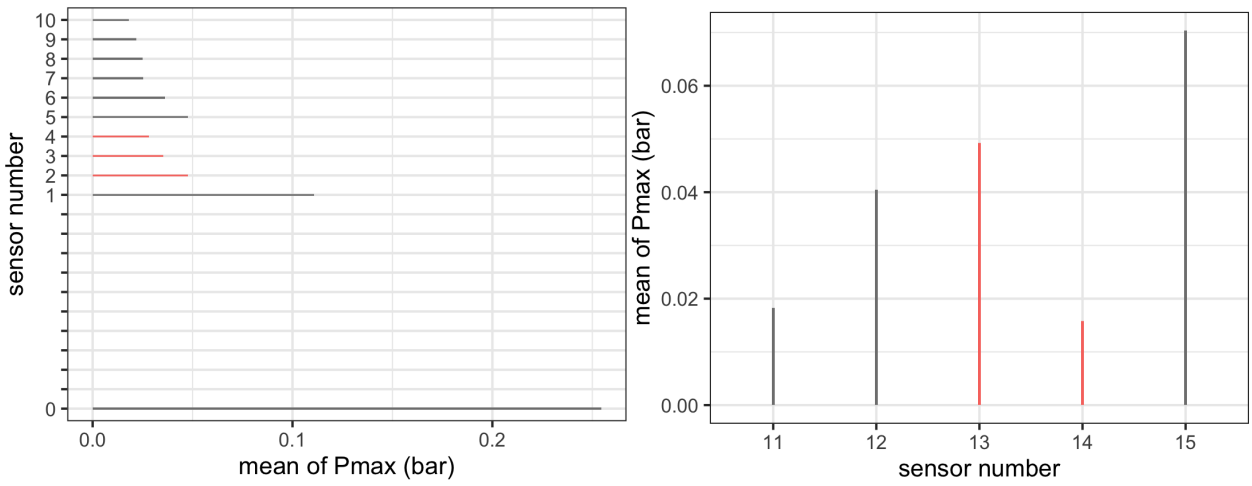

(a) (b)

Figure 3.11: Mean value of P_{max} on (a)the vertical, (b) the horizontal in the 2018-2019 campaign. The sensor in red have been in error for various amounts of time and for different reasons.

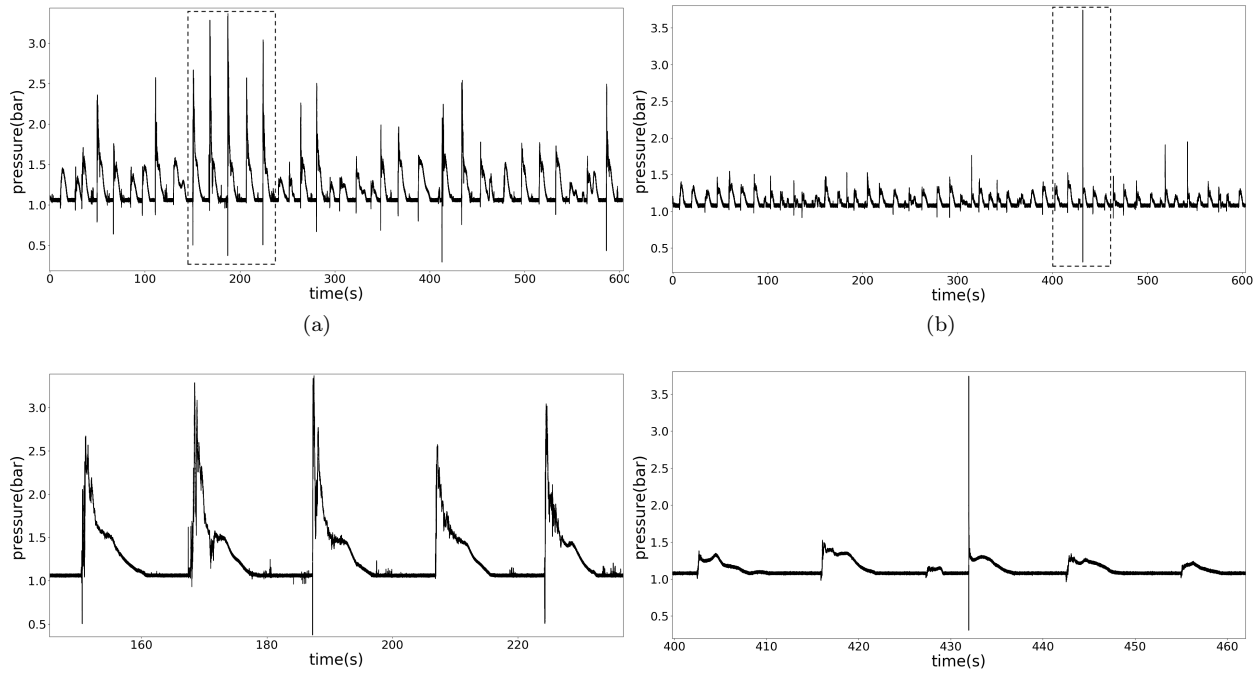

(a) (b)

(c) (d)

Figure 3.12: Examples of typical strong impact pressure signals recorded at the Artha breakwater. (a) 10 minutes burst recorded the 2016/02/09 at 4am (b)10 minutes burst recorded the 2016/03/11 at 5am. (c) and (d) correspond to the zoom delimited by the dashed rectangles in (a) and (b)

impacts, 8 presented a shape similar to (d). For these impacts, the mean ratio is 10 with a 3.5% standard deviation. They all present oscillations following the impulsive pressure peak, as seen in figure 3.13, with a

mean peak frequency around 15 to 20 Hz.

Figure 3.13 presents the pressure signal associated to the largest peak measured. This particular impact presents similar properties as the one presented in Figure 3.12 d) with a very sharp pressure peak and well-defined following oscillations. In Figure 3.14 the number of points show that the response frequency of the sensor is sufficient to detect some of the fastest phenomenon. Nevertheless the pressure reaches a threshold in this record. It correspond to the sensitivity range of the sensor

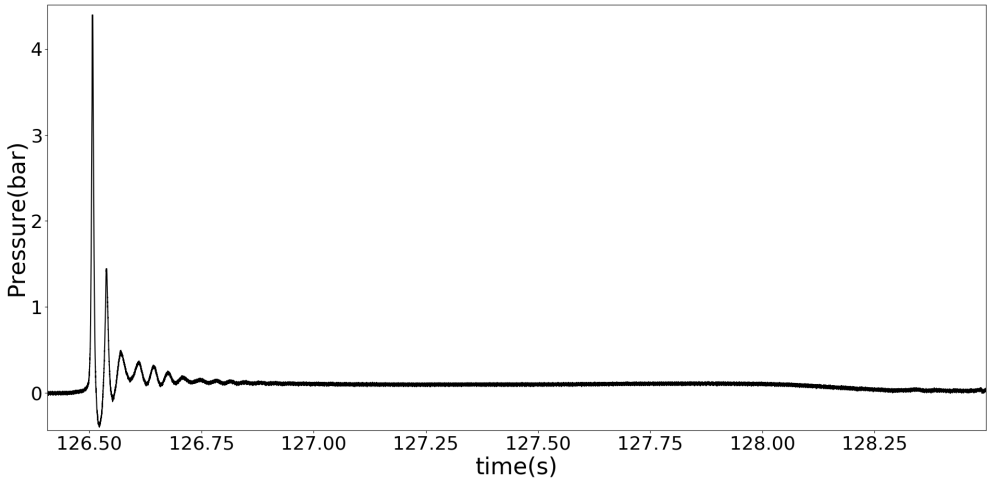

Figure 3.13: Pressure signal for the largest peak measured at the Artha breakwater, at sensor 0, the 21/01/2019 at 04 am

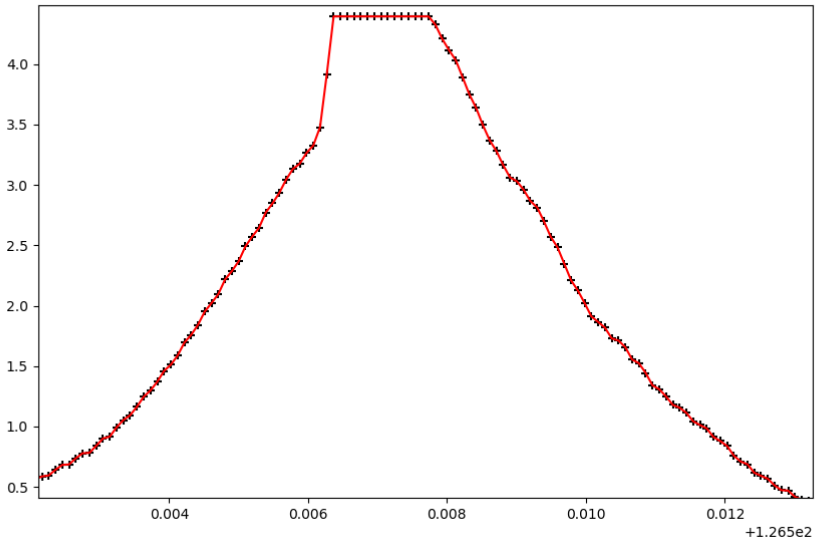

Figure 3.14: Detail of the pressure signal for the largest peak measured at the Artha breakwater, at sensor 0, the 21/01/2019 at 04 am

Figures 3.15 and 3.16 present the pressure signals observed on each sensor during two particular impacts representative of the two former classes. The impact of Figure 3.15 was recorded during storm conditions : $H_{1/3} = 5.2$ m, $T_{1/3} = 14.5$ s, $ws = 12.9\, m.s^{-1}$ while the one presented in Figure 3.16 corresponds to the highest impact pressure in the dataset obtained, as already mentioned, in moderate conditions. The associated force signal is shown on the right in both figures.

These figures show several interesting features. First, in both impacts, there is a shift in time in the pressure peak, the latter appearing first on the lower sensor and then rising gradually. For the impact of the 2019/01/23 6 am, the upward propagation speed of the pressure peak is $5.6\, m.s^{-1}$ in average, while the 2019/01/21 4am, it is of $15.4\, m.s^{-1}$. These speeds are in the same order of magnitude as previous in-situ studies [Bullock G. et al., 2004, Rouville et al., 1938]. Note that the signal can differ widely in shape from one sensor to another which may make it ambiguous to measure the time lag for instance, in Figure 3.16, the easily identifiable peak at sensor 0 is no longer present on sensor 1. The two impacts presented have also different characteristics in terms of pressure uniformity, the one observed on 2019/01/23 6 am, generating a much more uniform pressure (Figure 3.15 (a)) than the other one which displays a localized peak (Figure 3.16 (a)). Subsequently, the force time history is significantly different. Therefore, the first impact generated a large force (i.e. $\geq 100 kN.m^{-1}$) during about 3 s while the second one is much shorter ($\geq 100 kN.m^{-1}$ for only a few ms) in time.

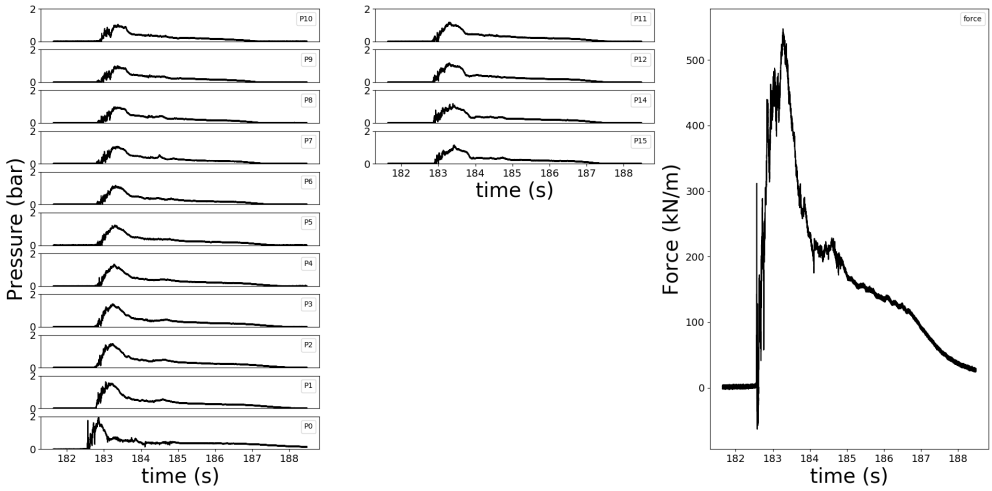

Figure 3.15: left and middle : Pressure signal during the maximal impact of the 2019/01/23 6 am at each sensor on the vertical and the horizontal (except sensor 13 in error). Right : Force signal associated with the impact represented on the left

Figure 3.17 which shows the complete force signal of the 2 bursts including the two analysed impacts confirms the exceptional nature of the impact recorded in (b). This figure also shows that storm conditions favor the frequent occurrence of large forces. This statement is further highlighted in Figure 3.18 showing the maximal force in function of the maximal pressure by impact for the 152999 impacts obtained in Damico et al. [2020]. On this plot, we note the existence of two sets of points. First, the upper cloud, for which large forces and large pressure are rather associated to large waves. Second, the points on the dashed line which correspond to events in which only sensor P0 records a non negligible pressure (cases where significant pressure is observed only at one of the upper sensors have not been identified). The impact of the 2019/01/21

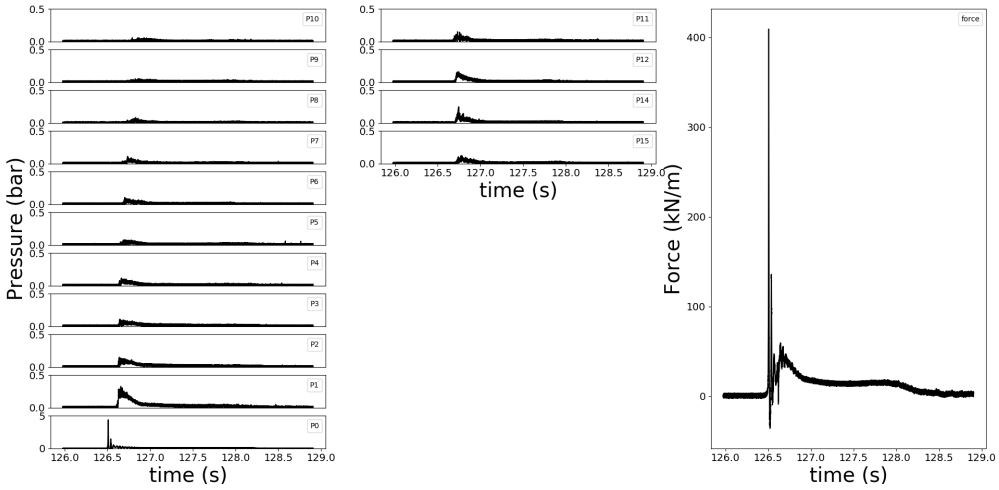

Figure 3.16: Left and middle: Pressure signal during the maximal impact of the 2019/01/21 4 am at each sensor on the vertical and the horizontal (except sensor 13 in error). Right : Force signal associated with the impact represented on the left

at 04 am, previously identified for its short and intense impulsive peak, is on the far right of this line. The points on the dashed line correspond to the weakest forces for a given P_{max}. They tend to occur for moderate wave conditions and mostly short risetimes.

Explanatory variables

In the explanatory variables dataset, the following remarkable values can be noticed. The significant swell height at the buoy reached 7.5 m the 2016/02/09 at 3 am and a swell period of 19.5 s was recorded the 2018/11/18 at 3 am. All $H_{1/3} > 6$ m in this dataset are from the same storm event which occurred the 2016/02/09. Regarding water-level, the maximum value is 5.01 m reached the 2019/01/23 at 5 am.

Figure 3.19 presents the histogram of the six explanatory variables for different thresholds of the response variable. The first column plots correspond to the distribution of the explanatory variables for all the impacts recorded by the station. As stated in Damico et al. [2020], the embedded pressure threshold which triggers the data acquisition, is only slightly larger than the atmospheric pressure. These plots show how explanatory variables are almost naturally distributed. Note that as the campaign duration is limited and due to the embedded threshold triggering the station acquisition, the data are slightly filtered as evidenced by the water level plot. The second column shows the plots for a threshold of 0.1 bar on the response variable; hence, the values of explanatory variable favouring moderate and strong impact pressures. Logically, the smallest wave heights are less present. The wave incidence is in average slightly shifted to the north. The lowest periods disappear as well as the low water levels. The changes in the wind parameters distribution is less obvious. Finally, in the last column plots, restricting the dataset to wave impact pressures larger than 1 bar, wave heights are in majority in the range 3-6 m, wave incidence is almost restricted to 0-20°with a peak in 10°, the period is comprised between 12 and 15 s, with a few events around 17 s or lower than 10 s and higher water levels are more frequent. Regarding wind parameters, looking at the initial speed distribution, the weight of higher wind speeds is now more important and the wind direction is almost only onshore.

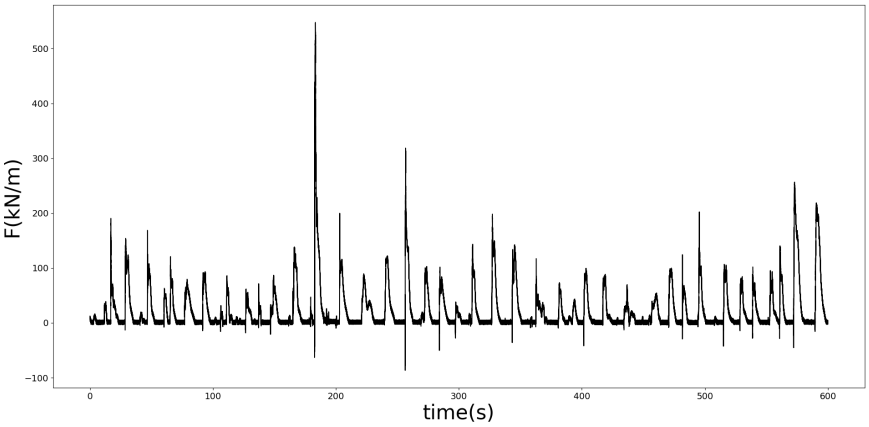

(a)

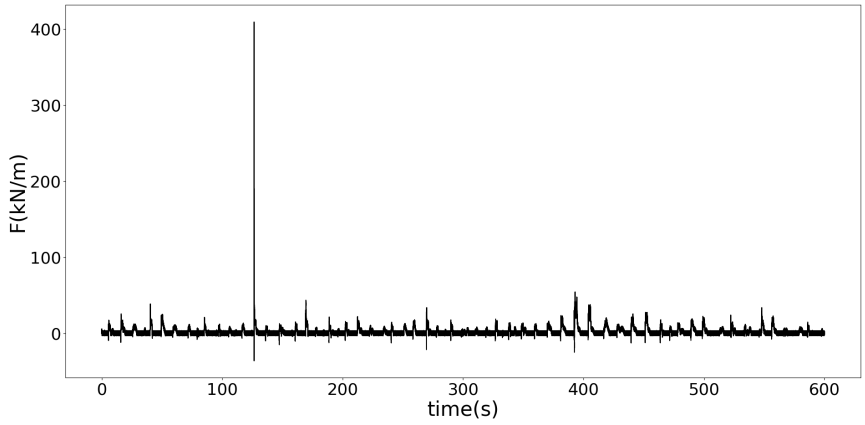

(b)

Figure 3.17: Force signal during a burst of acquisition, the 2019/01/23 at 6am in (a) and the 2019/01/21 at 4am in (b)

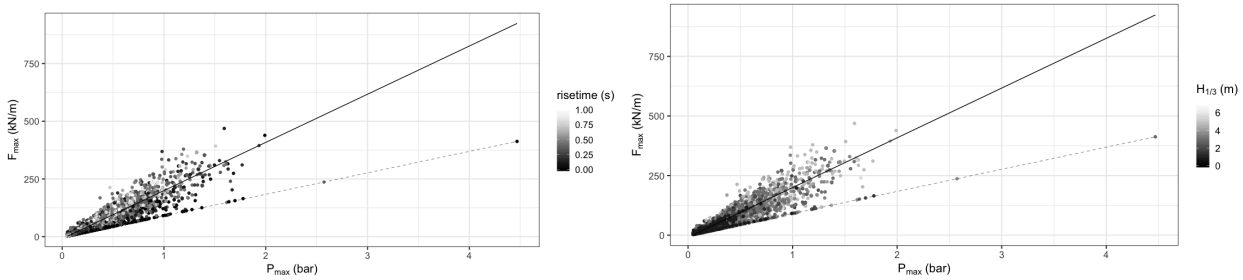

(a) (b)

Figure 3.18: Estimated linear force between sensor 0 and sensor 10 in function of maximal pressure by impact, colored by (a) risetime, (b) significant wave height. Dashed line is the linear inferior limit (linear coefficient : 92.76), full line is the result of the linear regression removing the points sitting on the dashed line (linear coefficient : 208.69)

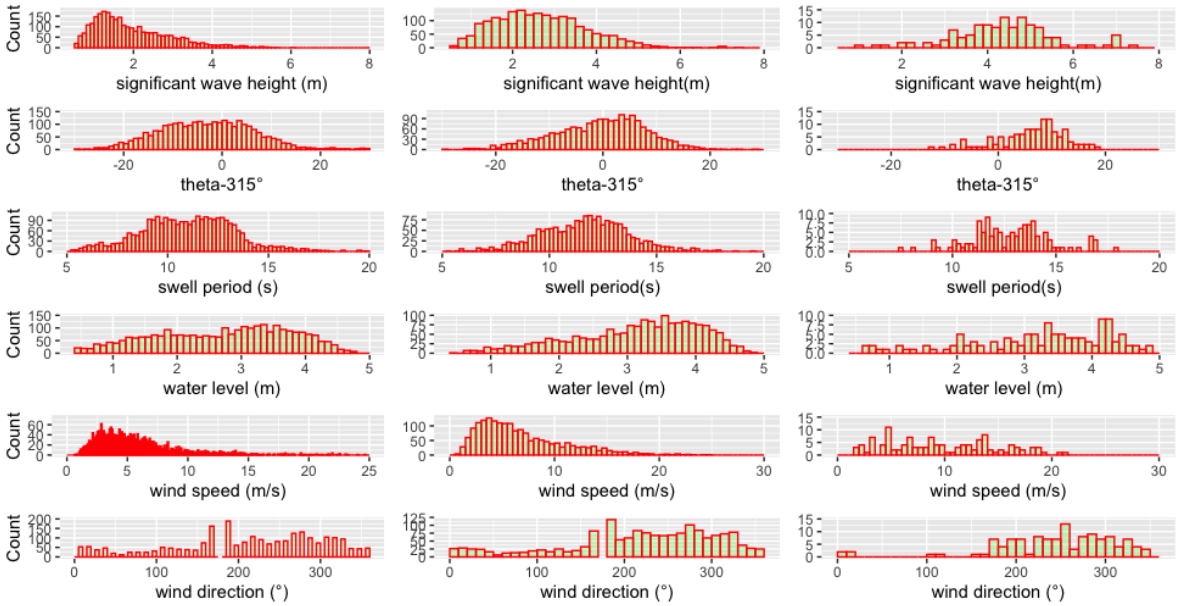

Figure 3.19: Histogram of explanatory variables with different thresholds for the response variable : 0, 0.1 and 1 bar

3.3.2 Statistical models

This part aims to statistically relate response and explanatory variables.

Linear model

The results obtained from the LMG indicator show that $H_{1/3}$ is by far the most important variable controlling the value of the response variable (Figure 3.20). Wave incidence is the second variable with this linear model. Swell period, water level and wind speed are similar in terms of explained variance with the LMG indicator. Only wind direction has a much lower influence on P_{max}. But according to the $p-value$ (Table 3.1), both wind parameters are unlikely to influence P_{max} within the framework of linear models.

The VIF indicator (table 3.1) is below 3 for all the variables showing that the colinearity between the explanatory variables is negligible.

Table 3.1: VIF and LMG values with estimates ($\hat{\beta}$) and $p-value$ for each variable for the full model

var	VIF	LMG	$\hat{\beta}$	p-value
$H_{1/3}$	2.2	0.60	0.20	0.00
θ	1.3	0.14	0.01	0.00
$T_{1/3}$	1.7	0.08	0.01	0.00
wl	1.1	0.08	0.10	0.00
ws	1.7	0.07	0.00	0.92
wd	1.2	0.02	0.00	0.69

Based on the $p-value$ and LMG indicator, the wind parameters can be removed and another model with fewer explanatory variables is created. A similar adjusted R^2, ($R^2_{adj,full} = 0.5159$ versus $R^2_{adj,reduced} =$

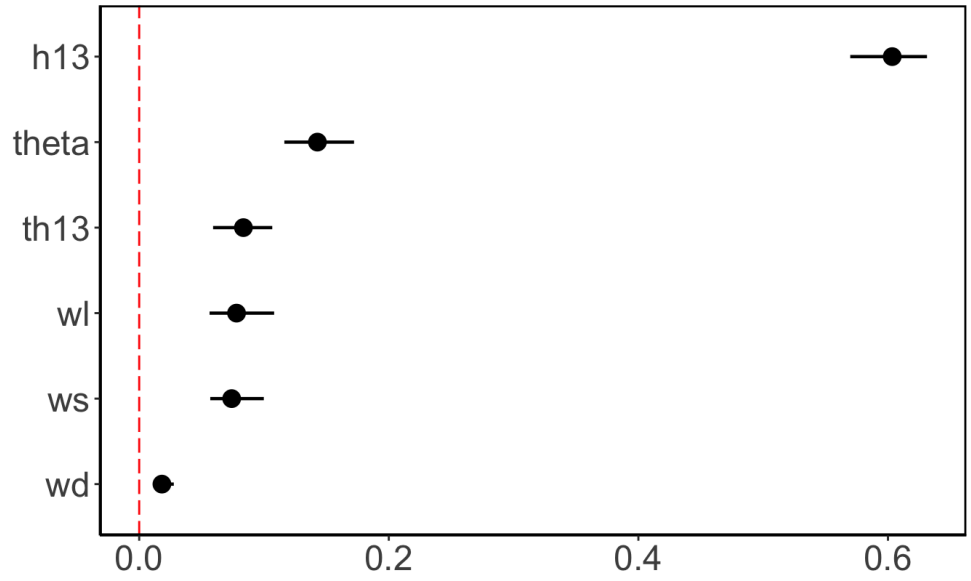

Figure 3.20: Relative importance of explanatory variables for P_{max} with bootstrap 95% confidence interval. $R^2 = 51.75\%$, metrics are normalised to sum to 1

0.5164), and a slightly increased AIC, ($AIC_{full} = -70.9$ versus $AIC_{reduced} = -74.8$), indicate that the model is only slightly improved. In this reduced model, the 95% confidence interval for the coefficient associated with $H_{1/3}$ is : [0.19 ; 0.21] ([0.0067 ; 0.0095], [0.0069 ; 0.0189], [0.09 ; 0.11], for θ, $T_{1/3}$ and wl respectively). Therefore, at fixed values of the other explanatory variables, P_{max} increases of about 0.2 bar (0.0081, 0.013, 0.1 bar) for a 1 m (1°, 1s, 1m) increase in $H_{1/3}$ (θ, $T_{1/3}$, wl, respectively).

GAM models

A similar procedure is applied for non-linear models. The relative importance of explanatory variables is shown in Figure 3.21. With this non-parametric R^2 equivalent, $H_{1/3}$ is still by far the main explaining variable. But, the order of importance of the following variables is different compared to the linear model. In particular, water-level appears as the second most significant variable in the non linear model before wave incidence, which is still significant and wave period, whose influence appears weak.

Wind parameters still appears insignificant with a $p - value > 0.05$. As previously, a new model is build excluding the wind variables. The improvement is negligible ($GCV_{full} = 0.0592$ versus $GCV_{reduced} = 0.0586$ and $R^2_{adj,full} = 0.5630$ versus $R^2_{adj,reduced} = 0.5632$).

In Figure 3.22 (a), the predicted P_{max} in function of $H_{1/3}$ are represented while the other explanatory variables are kept to their mean. The points are the observations in the $H_{1/3}$ - P_{max} plan. The reduced GAM model shows a slight non linear trend, which compared to the linear model, will predict slightly higher pressures for the highest waves. At least three outliers can be identified in this plot with $P_{max} > 1.5bar$ for $H_{1/3} < 2.5m$. The GAM model dependency in θ is very close to a linear one as evidenced in Figure 3.22 (c), whereas, it exhibits a sudden slope change between 4 and 5 m for the variable wl (Figure 3.22 (b)). This significant change in the model for high water levels may explain the difference between the linear and non

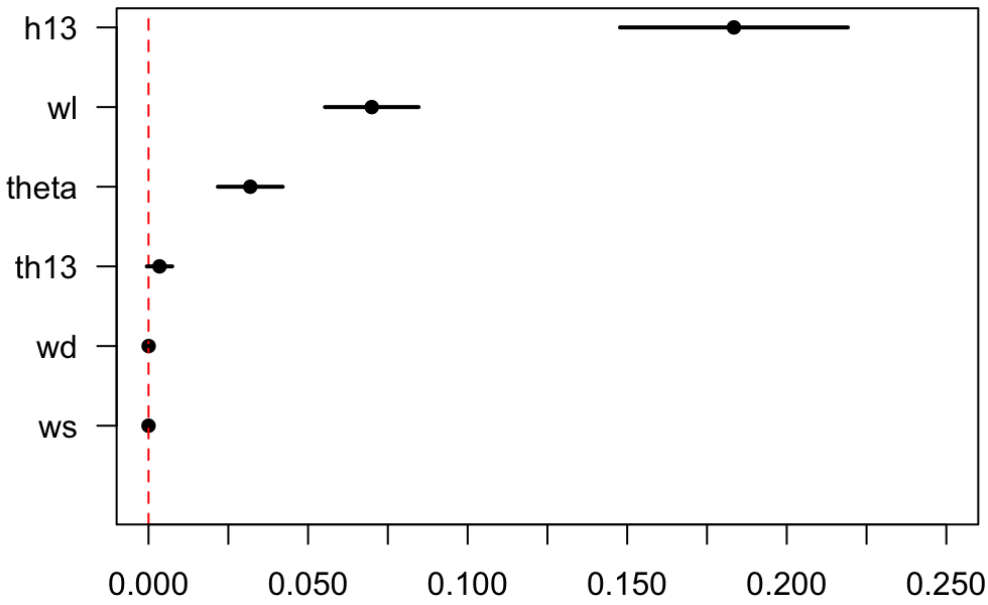

Figure 3.21: Variable importance as determined by the VIMP method. The dotted red line indicates the 0

linear models regarding the rank of importance of the water level.

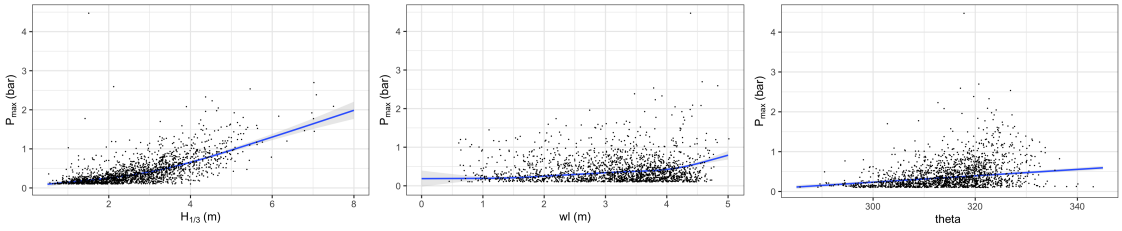

(a) (b) (c)

Figure 3.22: (a) Scatter plot of P_{max} versus $H_{1/3}$. The blue line is the reduced GAM model $(f_1(H_{1/3}) + f_2(mean(T_{1/3})) + f_3(mean(\theta)) + f_4(mean(wl)))$ (b) Scatter plot of P_{max} versus wl. The blue line is the reduced GAM model $(f_1(mean(H_{1/3})) + f_2(mean(T_{1/3})) + f_3(mean(\theta)) + f_4(wl))$ (c) Scatter plot of P_{max} versus θ. The blue line is the reduced GAM model $(f_1(mean(H_{1/3}))+f_2(mean(T_{1/3}))+f_3(\theta)+f_4(mean(wl)))$

The effect of the explanatory variables two by two is not fully taken into account with the previous model. A new model including the interaction between variables two by two is thus also created. After removing the least significant terms, the following model is considered :

$$\begin{aligned} P_{max_i} = f_1(H_{1/3_i}) + f_2(T_{1/3_i}) + f_3(\theta_i) + f_4(wl_i) + f_5(ws_i) + \\ f_{1,2}(H_{1/3_i}, T_{1/3_i}) + f_{1,3}(H_{1/3_i}, \theta_i) + f_{1,4}(H_{1/3_i}, wl_i) + \\ f_{2,4}(T_{1/3_i}, wl_i) + f_{3,4}(\theta_i, wl_i) + f_{3,5}(\theta_i, ws_i) + \\ f_{4,5}(wl_i, ws_i) + \epsilon_i \end{aligned} \quad (3.4)$$

To study how explanatory variables act together, the predicted P_{max} are plotted in the $H_{1/3}$ - wl plan in Figure 3.23 without and with interactions. On Figure 3.23 (a), the GAM model without interaction is plotted. The isocontours show an increase of P_{max} with increasing values of $H_{1/3}$ or wl separately, nevertheless, the largest gradient occur when $H_{1/3}$ and wl increase simultaneously. It means that, for the same significant wave height, higher P_{max} are generated when water-level rises (for instance high tides situation). We also note that the curving of the isolines is the most significant above $wl \approx 4$ m which is the level of the concrete berm at the foot of the vertical wall (Figure 3.5).

In Figure 3.23 (b) the values on the isolines varying from -0.6 to 0.4 represent the interaction effect on the predicted P_{max} while all the other variables are held to their mean. The interaction term shows significant values mainly for H_s over 5 m at any water level and for the highest water levels in moderate wave conditions (note that those are two regions of the $H_{1/3}$-wl plan with relatively fewer points and thus the interpretation should be taken with caution). For large waves, this interaction terms tends to increase the pressure at low water levels, decrease at average water levels and then increase again for higher water levels.

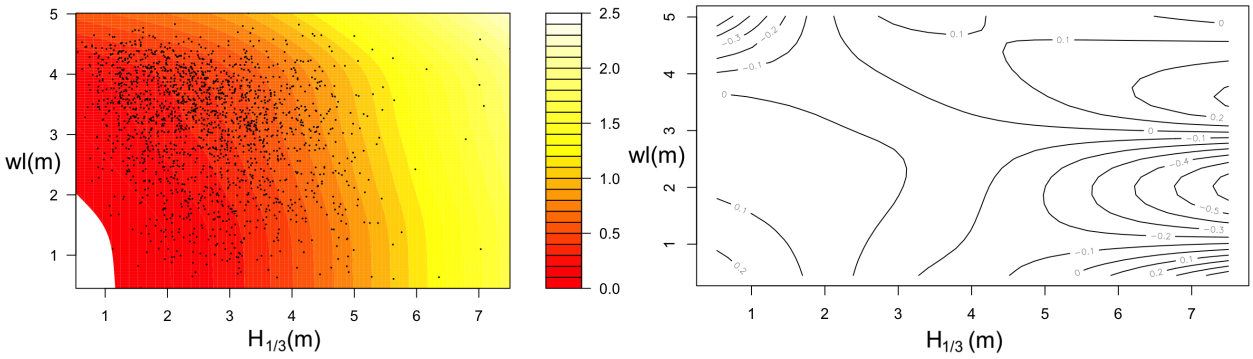

(a) (b)

Figure 3.23: (a) : Representation of P_{max} in the $H_{1/3}$-wl plan as predicted by the GAM model without interactions (other variables are set to their mean) (b) : Variation of predicted P_{max} only due to the interaction term in the GAM model with interaction

3.3.3 Rise times and pressure impulse

As seen in Figure 3.24 the distribution of P_{max} in function of the rise time rt is consistent with results found in the literature [Blackmore and Hewson, 1984, Bullock et al., 2007, Cuomo et al., 2010]. Thus, impacts with long rise time are weaker while impacts with high values of P_{max} tend to have shorter rise times. In our observations, approximately 86.5% of the impacts are located under the contour $P_{max} = 3100/risetime$ which was the upper bound in Blackmore and Hewson [1984] while 0.3% are above the contour $P_{max} = 31000/risetime$ which bounded the dataset in Bullock G. et al. [2004]. The multivariate analysis on rt and $P_{max} \times rt$ returned very weak values of R^2 for the linear as well as the GAM models (2% at best). Therefore the variability in rt and $rt \times P_{max}$ cannot be explained by the explanatory variables in this dataframe.

Figure 3.25 shows the distribution of the pressure impulse with the wave height and the water level, considering a dataset restricted to large pressure values (92 impacts over the 2018/2019 measurement cam-

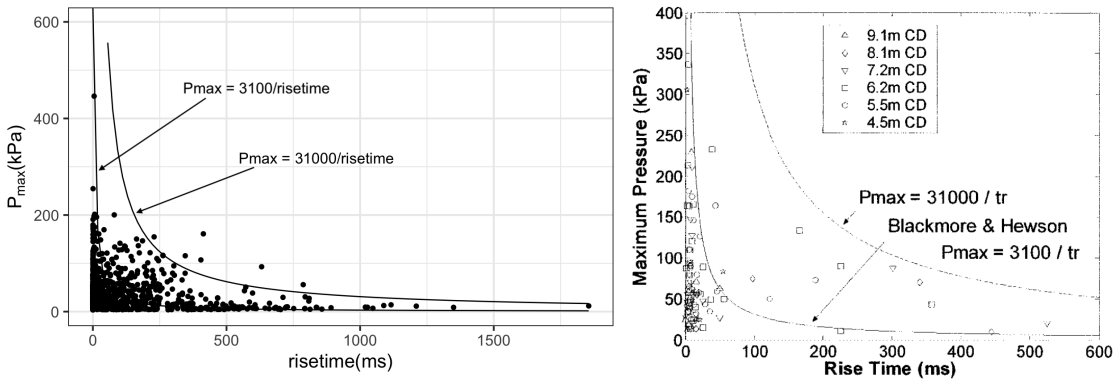

(a) (b)

Figure 3.24: (a) 2018/2019 observations in the P_{max}, rt plan (b) from [Bullock G. et al., 2004]: "Relationship between maximum pressure and rise time in the field"

paign). Values of the pressure impulse start to be noticeable only for $H_{1/3} \geq 2.5$m. For $2.5 \leq H_{1/3} \leq 3.5$m, large values of pressure impulse (≥ 0.3 Pa.s) only occur for high water levels. For $H_{1/3} \geq 3.5$m, they are observed in any water level conditions but mostly for a water level between 3 and 4m.

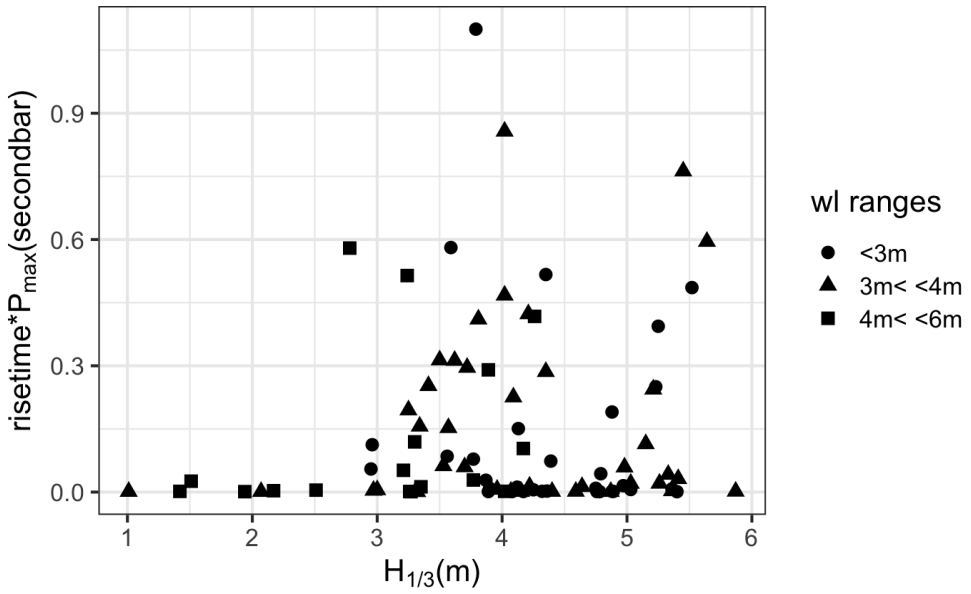

Figure 3.25: Variation of pressure impulse (estimated by $P_{max} \times rt$) against $H_{1/3}$ for different water levels. Dataset restricted to impacts of more than 1 bar.

3.4 Discussion

All the studies reporting in-situ measurements of waves impacts have highlighted the difficulty associated to measurements in this extreme environment. Continuous measurements over a long period are challenging and therefore not frequent. As a result, most in-situ measurements were restricted to one or two years [Blackmore and Hewson, 1984]. Two exceptions lasted longer though : the Dieppe experiment Rouville et al. [1938] and the Alderney experiment Bird et al. [1998]. Regarding the amount of data collected and the range of wave conditions experienced, over two winters at the Alderney experiment, Bullock et al. [2001] collected 50 20-minutes bursts at a 500 Hz sampling rate. In this dataset, pressures up to 3.96 bar were observed with a corresponding significant wave height at the toe of the breakwater of $H_s = 2.88$m. Later at the same location, Bullock G. et al. [2004] reports 8 months of measurements with H_s up to 3.1 m and a maximal pressure of 3.37 bar. In Rouville et al. [1938], the largest swell event involved an offshore wave height of 4.5 m with a period of 8.6 s and only examples of impacts are provided, among which the second largest impact pressure ever recorded. In Blackmore and Hewson [1984], wave heights up to 1.3 m were recorded along with 112 impacts, all lower than 0.48 bar.

In the present experiment, two years of data have been collected so far but the particularly exposed nature of the site and the efficiency of the station, allowing a quasi-continuous recording, has already provided a greater number of impacts. Hence, 1851 10-minutes bursts at 10kHz, reaching pressure of more than 0.1 bar over atmospheric pressure have been collected, among which 122, included pressures of more than 1 bar. During the 2018-2019 campaign alone, this makes more than 400 impacts of more than 1 bar. This unique dataset provides the opportunity to calculate the impact pressures statistics presented in this paper. Moreover, these impacts were generated in wave conditions ranging from $H_s = 0.5$ m to 7.50 m so covering a larger range than in previous studies. The direct vicinity of a directional wave buoy, tide gauge and semaphore additionally provides a unique set of synchronized external variables in order to build a statistical model relating impact maximum with the related environmental conditions. To our knowledge, this is the first time that such a model based on field data is proposed.

In the model using multiple linear regression, the pressure maximum is explained mostly by the significant wave height (relative importance 60%), followed by the wave incidence (14%) and then the significant wave period, the water level and the wind speed (all around $7 - 8\%$). In the non linear GAM model, the water level appears as the second most important variable still far behind the significant wave height. Except for that noticeable exception, the variable ordering is similar as in the linear model.

Wind speed was only significant (but at a small level) with the GAM model with interactions whereas wind direction is insignificant for all statistical models. Therefore, the influence of wind in the impact process in the field appears to be very small compared to the influence of the other variables. The influence of wind has not been published in any in-situ campaign mentioned in this paper. Yet it has been taken into account for large scale, open air experiments by Hofland et al. [2011]. The tank was submitted to local wind conditions and hindered the repeatability of impacts due to small perturbations on the wave face. It was taken into account as a Boolean variable and its influence was shown in the results.

P_{max} of more than 2 bar have been mainly observed in two types of conditions: storm events with large significant wave heights or with moderate wave heights and water level of more than 4 m. In the second case, the impacts present distinctive oscillations and high impulsive peak to steady level ratio.

(a) (b)

Figure 3.26: Photographs of a wave impact during a storm event at the sensor location on December 9 2019 around 4pm. $H_s = 5.9m$, $T_p = 15s$, $wl = 2.9m$, courtesy of Bernard Bayle

The two classes are consistent with the classification proposed in Oumeraci et al. [2001] and already described previously. This classification predicts a behavior change of the Artha breakwater depending on the water level and the wave height. Most of the impacts are generated by high waves. No matter the water level, in this case, mostly broken waves are expected based on Oumeraci et al. [2001]. This is confirmed in Figure 3.26 showing a broken wave impact in this kind of conditions. Additionally, in the PROVERB classification, the pressure signal corresponding to broken waves impacts show slight irregularities after the first pressure maximum which are also present in Figure 3.15. The statistical models established in this study are able to predict the pressure maxima in this first type of impact properly. In this case, the pressure maxima are mostly proportional to the offshore significant wave height and the pressure signal is similar in shape within this group.

According to the Proverb classification [Oumeraci et al., 2001], the impulsive impact type is likely to appear for very large water levels and moderate wave energy. An example of the condition favoring the occurrence of this type of impacts is given in Figure 3.27. Impacts belonging to this second class are not frequent and are likely to involve wave breaking directly on the wall. This type of impacts is also characterized by very localized high magnitude short pressure peaks (Figure 3.16) which may be the cause of the localized damages recurrently observed on the breakwater masonry. Our measurements show that these impacts are also associated with characteristic pressure oscillations which may be the signature of air entrapment Bagnold [1939], Bullock et al. [2007]. The observed frequencies around 20Hz and up to 50Hz are lower than those observed in laboratory with thin and thick entrapped air pocket (i.e., $o(100)$Hz in Hattori and Arami [1993]). The scale, seawater density, the presence of remaining air bubbles of various size due to previous wave breaking and the possibility of lateral air escape can all explain the lower observed frequency. As seen in figures 3.12, sub-atmospheric pressure have been measured for numerous impacts, in two part of the pressure signal. Either during the oscillation following the impulsive peak or just before the rise of pressure at the very beginning of the impact. The later is also reported in Hattori and Arami [1993] who invokes the very fast upward motion of water at impact as a possible explanation. This impact type is not well predicted by the statistical models developed in this study. This group needs more observations to be better understood and may also require higher level models such as machine learning algorithms to reach a possible prediction. This direction is left for a future work.

(a) (b)

Figure 3.27: Photographs of wave impacts at the sensor location in moderate wave condition and high water level (11/05/2018 1h45pm, $H_s = 2.70m$, $T_s = 13.5s$, $wl = 4.213m$)

Thanks to the pressure sensor array, wave impact pressure distribution is known and the mean distribution, as well as specific impacts distribution, was studied. Overall the lower sensor is always the closest to water level and the mean profile shows decreasing pressures from the bottom sensor to the top. This is in agreement with previous studies, including Goda [1975], Cuomo et al. [2010], showing that maximal pressure is located around mean water level. The very high discrepancy between the lower sensor and the upper array for a few particular impacts is consistent with the very localised pressure peak observed for flipthrough impacts and high aeration impacts. Several studies have reported this type of pressure profile, among which Bullock et al. [2007], Hofland et al. [2011]. The horizontal distribution has also shown longshore variability likely at least partly due to the wall curvature. The limited number and the particular spatial distribution of sensors added to the curved shape of the Artha western roundhead wall are two limitations for the direct comparison with experiments on vertical walls in controlled environments. Moreover, also due to the former points, it is also likely that the actual maximal pressure was not captured in our experiment.

The estimated load applied on the structure also showed important difference between very impulsive impacts and slower ones (i.e., Figures 3.15 and 3.16). With the latter, the force lasts obviously longer which has implications for the structural response. The maximum magnitudes could also be compared, however, in the case of Figure 3.16, the estimation of the load using a linear assumption is biased by the sensors spatial distribution and the localized pressure in the second case and thus, the maximum force value is likely to be overestimated. Apparently, the magnitude reached by the two forces is comparable in both cases ($500kN\,m^{-1}$against 400). Nevertheless, the difference is striking when non-dimensionalizing by $\rho g H_s^2$ (with $H_s = 5.2\,m$ and $1.5\,m$ respectively). In this case, the respective relative magnitudes are 1.85 and 17.8. These values are consistent with the values proposed in the two right bottom panels presented in the PROVERB classification, namely around 2 and 8. Nevertheless, a strict comparison is not relevant due to the overestimation of the load in the impulsive case and because the PROVERB classification used the breaking wave height as reference which was not measured in our study.

Large and long duration forces are likely to be required to possibly induce large structural element

displacement. Here we show that these conditions correspond to storm conditions with large waves. Such an accident fortunately never occurred so far for the Artha breakwater, which is the main protection for the city of Saint Jean de Luz against flooding, while few meters high 50 tons concrete block displacements originating from the block armor unit have been already reported. With respect to the structural stability, preliminary calculations show the critical role of the uplift force, which was unfortunately not measured in this study. For instance, the impact of 2019/01/23 at 6 am, lead to an unstable condition when extrapolating the uplift force by assuming a continuous pressure at the corner and a linear profile.

The multivariate analysis on risetime rt and $rt \times P_{max}$, which is an approximation for the pressure impulse, showed a low correlation with the explanatory external variables. This is a surprising result as the pressure impulse is expected to be less chaotic than the maximal pressure [Bagnold, 1939]. It may be related to the presence of the block armor which acts as an additional filter influencing the wave shape in a complex way compared to controlled wave conditions in laboratory. This particular point will require additional work to be fully understood. Figure 3.25 (a) shows that we have already recorded the largest pressure impulses reported in the literature represented by the few points above the $31000/rt$ line. This illustrates the interest of the site, favoring a large range of wave conditions, especially considering that measurements are still ongoing. We expect therefore to obtain valuable information on the most extreme impacts in the next few years.

As already stressed, the position of the sensors is one of the main limitations of this study. It was not possible to install the structure supporting the 15 sensors on a lower part of the vertical wall due to practical constraints. As a result, the lowest sensor is always the one the closest to the mean water level and it regularly detects the highest pressures which is coherent with the present knowledge about wave impact. Yet several factors increase the unpredictable nature of the phenomenon and therefore the elevation of the peak pressure. The shape of incoming waves is by essence a stochastic phenomenon. The disposition of the blocs is also random. Finally, swell direction, the curvature of the crown wall and the fact that the wall is not strictly vertical, are additional factors potentially explaining deviation to the previous rule. Another limitation of this study is the acquisition frequency. Indeed Kimmoun et al. [2010] used a sampling frequency up to $40kHz$ to properly discretize very sharp pressure peaks. Higher peak pressure and other fast phenomena could have been missed due to the response frequency of the sensors. Actually higher frequency sensors were initially installed on the upper array. Unfortunately, they were delivered with the wrong environmental requirement and were quickly corroded before any measurements could be performed. The remote nature of the installation makes it complicated to access the station in case of failure, in particular during the winter season. Some failure occurred and generated some discontinuities in the acquisition. Progressive improvements of the station is ongoing to avoid such failures. It is therefore expected that a much larger and comprehensive dataset will be available in a near future and provide a unique opportunity to better understand this complex process in nature.

3.5 Conclusions

High-frequency wave impact pressure measurements have been carried out at the Artha breakwater in 2015/2016 and in 2018/2019. 1851 10-minutes long bursts were recorded including an impact of $4.5\,bar$. A surprisingly low value compared to the largest impacts observed in Rouville et al. [1938], Bullock et al.

[2005].

The maximal pressure over 10 minutes is considered as the response variable. Six explanatory variables were continuously measured over the same period. A statistical analysis of this dataset was conducted based on multiple variable linear,non-linear and non-linear with interactions models. These models show that the significant wave height has a dominant influence overall. Hence, at the Artha breakwater, the linear model predicts an increase of 0.25 bar for 1 m in wave height. Waves incidence (linear) and water level (non-linear) are the explaining variable coming next while wave period appears less important and wind not significant at all. Non linear effects have been identified, in particular for high water levels, and several interactions of variables were statistically significant.

The analysis of the pressure signal shows the existence of two main classes of impacts associated to large values of the response variable. The first class, observed during storm conditions gathers strong and long duration impacts with relatively uniform pressure in space, likely due to broken waves. The second class, associated to moderate conditions and large water level values, shows very localised pressure peak in space and time, likely due to wave directly breaking onto the wall. The two classes also differ by their peak to steady level ratio, the second one showing much larger values. The very impulsive impacts belonging to class two also present well defined damped oscillations. The impacts in the first class make up for most of the dataset and are therefore well predicted by the statistical model. The second class is much rarer and show bad correlation with environmental variable. A more precise understanding of these outliers and the conditions in which they occur will be achieved in the future by a systematic classification of impact types and study of waves transformation over the block armour.

Finally, the PROVERB classification appears as a reliable tool in the present study to predicts the changes from one class to the other with water level and wave conditions.

Chapter 4

Transformation of the wave field over a composite breakwater, in-situ measurements and numerical simulation

Contents

4.1 Introduction

In chapter 3, a statistical correlation between the environmental conditions and the wave impact pressure has been showed. Nevertheless outliers have been observed and unexplained variability remains. The statistical

model of chapter 3 uses as input parameters : offshore wave parameters, water level in the bay and wind velocity. In particular, it does not include wave transformation processes which occur between the offshore wave buoy location and the breakwater. As mentioned by Peregrine [2003] for instance, the wave shape before impact highly controls the pressure profile. Hence, wave reflection, refraction, dissipation and transmission should have a significant influence on the impact load on the structure. The first objective of this chapter is to better understand the transformation of the wave field from the offshore wave buoy to the vertical wall of the breakwater in order to draw hypothesis regarding the remaining variability not explained by the statistical model in chapter 3.

The data presented in chapter 3 form one of the most extensive wave impact database ever recorded on a composite breakwater. In the studies described in Bird et al. [1998], Bullock et al. [2007], Bullock G. et al. [2004] and derived from the latest extensive in-situ wave impact pressure measurements, results were not compared with existing engineering formula used for breakwater design. To fill this gap, we will compare the predictions of the statistical model of chapter 3 with the widely used formula for vertical wall described in Goda [1975]. In order to perform this comparison, the maximal wave height expected in front of the breakwater for a given sea state is required. It is the second objective of this chapter to obtain this parameter.

Wave transformation over very steep and highly fractured rocky environments has been scarcely studied in the field. Therefore this experiment has an interest with regards to the knowledge of wave transformation over this type of media. The Artha breakwater is a man made structure on which it is relatively easier to install sensor than on a natural cliff. For the immersed sensors, the only advantage of the blocks compared to a natural rocky seabed is that they offer a flatter surface to fix them. While not a natural environment, the Artha breakwater is build on an existing reef and the elements of the block armour are displaced by the waves during severe storms in winter [Bougis et al., 2016]. This makes this site particularly interesting as presenting similarities with natural rock cliffs while certainly easier to instrument in a lasting way.

Most in-situ experiments dealing with wave transformation were conducted on low sloping beaches [Huntley et al., 1977, Guza and Thornton, 1982, Ruessink et al., 1998, Senechal et al., 2011]. The experiment conducted by Poate et al. [2016] on steep foreshore slope ($\tan(\beta)>0.1$) gravel beach allowed them to propose a formula to estimate wave run-up in this type of environment. The knowledge of the run-up process in steep rocky beaches or on man-made structures similar in terms of geometry is more limited. Indeed, the harshness of the conditions in this type of environment make it particularly difficult to conduct in-situ measurements. Laboratory experiments are relatively easier. In particular, in Van der Meer and Stam [1992] wave run-up on smooth and rocky gentle slopes is compared. The run-up on rocky slopes is obviously diminished compared to smooth slopes. For steeper slopes, the influence of the surf similarity parameter appears to be dominant. Dodet et al. [2018] studied the wave field in the intertidal zone of rocky beaches in cliffs environments with slopes $0.1 < tan(\beta) < 0.4$ based on in-situ pressure measurements. An array of pressure sensors was used to estimate the run-up ($R_{02\%}$). A diminution of the wave run up is shown, likely explained in part by the bottom roughness.

This chapter presents pressure measurements performed in the block armour of the Artha breakwater in October/November 2018. The objective was to better understand the wave field in the vicinity of the structure. These measurements are completed with the high frequency impact pressure measurements routinely carried out on the wall. Potential correlations between the wave height at the toe of the breakwater and the offshore swell parameters are assessed. The significant wave height profile and reflection coefficient

are then determined and analysed. The number of submersion events at the lower high frequency pressure sensor on the wall of the breakwater is evaluated as an indicator of run-up on the vertical wall. The results of the in-situ measurements campaign are complemented by numerical simulations using the SWASH model Zijlema et al. [2011].

In section 4.2, the measurement campaign, post-processing methods and numerical model used in this chapter are presented. Then, the results are detailed in section 4.3 and discussed in section 4.4. At the end of this section, as formerly indicated, a comparison between the statistical model developed in chapter 3 and Goda's formula [Goda, 1975], using the maximal wave height determined from numerical simulation, is finally proposed.

4.2 Method

4.2.1 Experimental setup

Wave field measurement

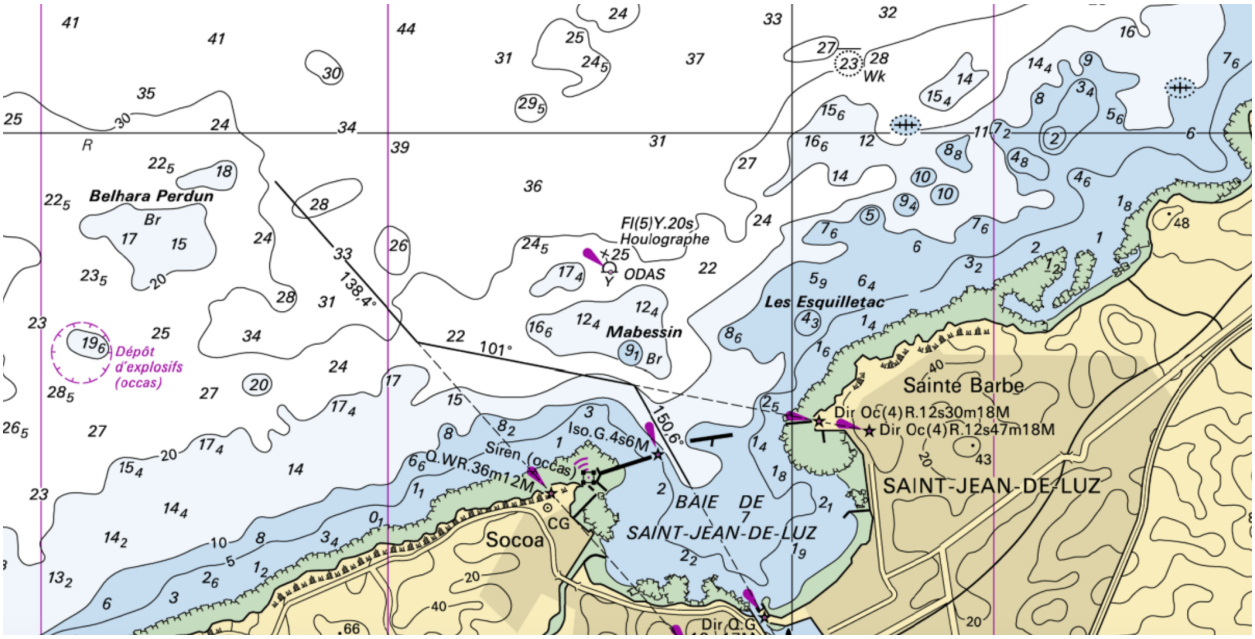

Figure 4.1: Bathymetry chart of the environment studied (source : SHOM website)

The bathymetry nearby the Artha breakwater is particularly heterogeneous (figure 4.1) and as a consequence, wave transformation is likely to be complex in this area. Additionally the block armour presents very steep parts and is very irregular due to the size of the blocks and their continuous displacement under the action of the most energetic storms.

In order to characterise the wave field in the vicinity of the structure, a field measurement campaign was organised in October/November 2018 involving several sensors. An Acoustic Doppler Velocimeter (ADV) and four pressure sensors (RBR Solo - PS0, PS1, PS2 and PS3) were placed on a first transect at depth of -14.5

m ,−12.9 m, −8.1 m, −4.5 m and 2.5 m respectively (Figure 4.2). The second transect was implemented in order to assess the long-shore wave field variability.

The pressure sensors used in this campaign are compact single channel loggers with standard sampling capacity of 2 Hz. The measurement range is $[0, 50]$ bar with a 0.025 bar resolution. The sensors were embedded in a protecting tube fixed on a stainless steel corner anchored in the concrete blocks as shown in Figure 4.3. Pressure was recorded continuously.

The ADV was installed at the foot of the breakwater block armour on a tripod weighted down by 100 Kg and connected to the blocks by a metallic chain. The maximum sampling rate is 4 Hz, and the measurement range $\pm 5\ m.s^{-1}$. The ADV carries an integrated piezo-resistive pressure sensor with a 300 m range and a 0.005% of full scale precision. In this campaign, the ADV recorded pressure and local east, north and upward velocity components at 2Hz by 20 minutes bursts every 2 hours.

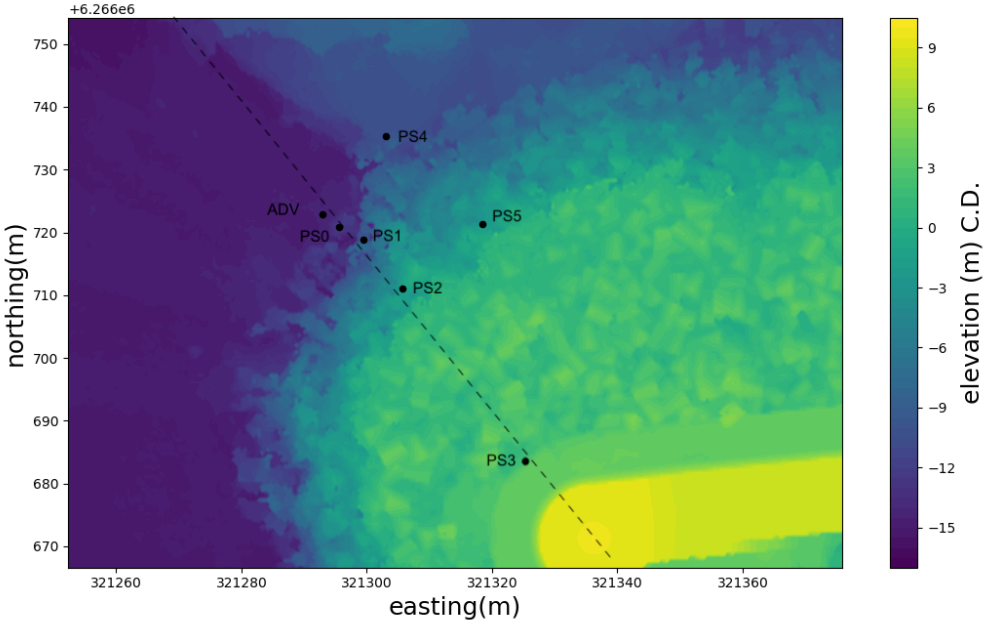

Figure 4.2: Artha Bathymetry (May 2017) and topography (March 2016) with the position of the sensors implemented in October 2018

The installation of the sensors was carried out by qualified divers under the guidance of a member of the scientific team on the boat. They followed the implantation plan as best as possible given the danger to operate underwater nearby the block armour. Even though the operation took place during a very calm day in term of wind and swell, the wave induced movement underwater in the vicinity of the blocks significantly increased the complexity of the intervention. The planimetric position of the sensors was determined with a basic GPS held at the vertical of the sensor on a floating device. The GPS precision and the rope verticality were two sources of error for the positioning of the sensors. The difficulty to operate in this environment resulted in slight differences in the sensor location compared to the initial plan. Hence, the directional current meter was installed a little bit closer to the lowest block and PS1, closer to PS0 than initially planned.

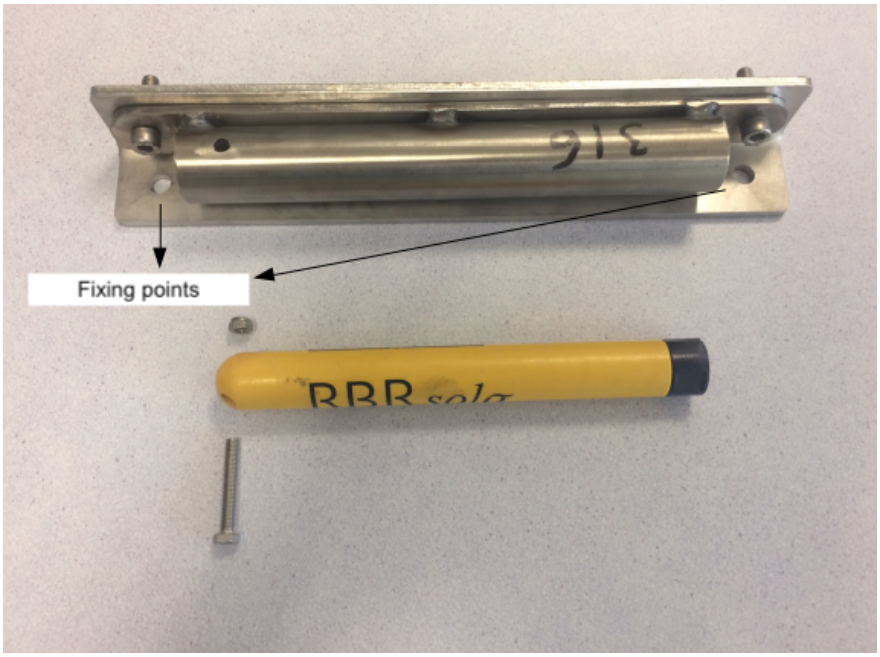

Figure 4.3: Picture of the stainless steel structure (top) and a pressure sensor RBR solo (bottom)

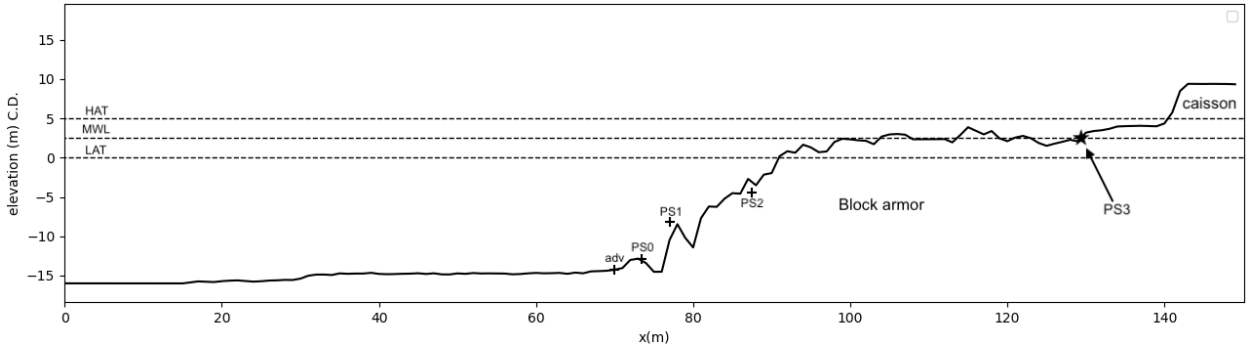

Figure 4.4: Cross section of the main transect showing the five sensors

Sensors were installed the 04/10/2018 and recovered the 21/11/2018. The range of wave heights, periods and directions as well as water level observed during the campaign are presented in Table 4.1.

PS3 was not recovered. This sensor was located in an area submitted to wave breaking which probably tored the whole supporting device. Additionally, one of the screw fixing the directional current meter to the tripod was stripped from its location, allowing slight movements of the instrument. This resulted in uncertainties for the measured velocity, which was finally not considered in the analysis.

Wave impact count on the wall

To assess the validity of the numerical model used in this chapter, we would like to compare the signal recorded on the wall with the high frequency pressure sensors used to study the impact with the output of

n/var	min	max
$H_s(m)$	0.41	3.96
T_p (s)	5.88	18.18
$\theta_P(^\circ)$	278.43	355.78
$MWL_{socoa}(m)$	0.28	4.48

Table 4.1: Table presenting the parameter for scenarios N1 to N5

(a)

(b)

Figure 4.5: Underwater view of a : the directional current meter, b : the pressure sensor PS2 in its housing

the model which is basically a run-up at this place. The measurement of the run-up at the Artha breakwater vertical wall was not something planned initially. Therefore a proxy for the run-up level had to be found. The experimental set-up described in chapter 3 provides high frequency pressure measurements simultaneous to the immersed pressure sensor array. The immersed sensors main transect is aligned, as best as possible given the experimental conditions, with the high frequency sensors and the center of the roundhead. While the instantaneous impact pressure is sensitive to the stochastic nature of the wave signal, the number of impacts on the wall is likely more stable when computed on a representative duration for a steady incident

wave field. The number of impacts is the proxy chosen to compare with the SWASH model output.

The pressure sensor considered for the impact count is the lowest one, namely P0. For each pressure burst during the measurement campaign, the number of impacts is extracted. The impact count is incremented for every maxima observed over a threshold of 0.1 bar. A few bursts were not recorded as described in chapter 3 and therefore kept as 0. The correlation of the impact count and the free surface signal obtained with the model SWASH is carried out in section 4.3.2.

4.2.2 Post-processing methods

Wave buoy data

In chapter 3, offshore wave parameters are provided by the measurement from the buoy of the CANDHIS network and the post-processing software developed by Kergadallan et al. [2020]. In this chapter, in order to be consistent, we wanted to use the same frequency bands at the buoy and at the pressure sensor. Therefore, the raw spectra at the buoy is used to determine Offshore wave parameters. The datawell directional wave buoy records 30 min burst every hour. We have access to $S(f)\,\mathrm{d}f$ the free surface elevation variance of the raw spectra at the buoy for each burst. The first order moment of the signal is then :

$$m_0 = \int_{f_1}^{f_2} S(f)\,\mathrm{d}f\,\mathrm{d}f \tag{4.1}$$

With f_1 the cutoff for low frequency and f_2 the cutoff for high frequency. The offshore significant wave height H_s given by:

$$H_s = 4\sqrt{m_0} \tag{4.2}$$

Peak period (T_p) and peak direction (θ_p) are also extracted as period and direction at the maximal amplitude in the raw spectra.

Post processing of pressure data collected in the blocks

In order to obtain consistent data with the offshore buoy, the records are split in 30 minutes bursts. A small pressure offset has to be taken into account for each sensor. Based on sea level pressure measurements at the nearby Socoa semaphore (slp), a pressure measurement made outside of the water at the end of the campaign by each sensor (p_{ref}) and the sea level pressure at the time of p_{ref}, (slp_{ref}), the pressure offset p_{offset} for each sensor is given by :

$$p_{offset} = \frac{slp * p_{ref}}{slp_{ref}}$$

We then have :

$$p = p_{mes} - p_{offset}$$

With p_{mes} the raw pressure given by the sensor and p the pressure after the offset correction.

Based on the linear Airy theory, pressure at a given altitude z is :

$$p = -\rho g z - \rho g \eta K_p(z) \tag{4.3}$$

and

$$K_p(z) = \frac{\cosh k(z+h)}{\cosh kh} \tag{4.4}$$

With negative z downward. By removing the tide trend (considered linear over 30 min) we get :

$$p_{det} = \rho g \eta K_p(z) \tag{4.5}$$

with η the free surface, so :

$$\eta = \frac{p_{det}}{\rho g K_p(z)} \tag{4.6}$$

With the amplitude of the discrete Fourier transform of $\frac{p}{\rho g}$ denoted A, the 0th order moment is :

$$m_0 = \int_{f_1}^{f_2} \frac{(A/K_p)^2}{2\,\Delta f}\,\mathrm{d}f \tag{4.7}$$

Finally, with $f_1 = 0.05$ Hz and $f_2 = 0.17$ Hz, the measured significant wave height is : $H_s = 4\sqrt{m0\Delta f}$ with Δf the frequency resolution of the discrete Fourier transform.

Given the uncertainties on the velocity already mentioned, only pressure measurements were considered at the directional current-meter. The post-processing procedure is identical to the one of the pressure sensors in the blocks.

Reflection coefficient

The reflection coefficient was estimated based on the three probes method of Mansard and Funke [1980]. The latter allows to separate the incident and reflected parts of the signal based on a Fourier decomposition and the study of the phase shift at three probes of known position. This method suppose limited depth variation between the three probes. It is not the case here. The steep bathymetric slope implies an increase of the wave amplitude and a phase shift (decrease of the wave length). These feature cannot be taken into account by the three probes method. The phase and amplitude modification due to bathymetric variation are eliminated with the least square method of the three probes procedure. The reflection coefficient is then the ratio between reflected and incident significant wave heights H_{sr}/H_{si}. The coefficient was estimated at the three pressure probes in the block armour, an area where dissipation affects the wave energy balance. Therefore, the reflection coefficient estimated is local and not completely representative of the whole reflection induced by the structure.

The distance considered for this analysis is calculated along the transect axis. This is a potential source of error as the probes were not perfectly aligned along this axis. We also observed a maximal temporal deviation of 1 s between the pressure sensors at the end of the measurements. This indicates a small temporal shift whose rate depending on the sensor is unknown. This temporal deviation is of the order of the temporal resolution (0.5 s). There is no evidence that the temporal shift is linear and therefore it can not be corrected continuously over the whole campaign. As a consequence, the reflection coefficient was only determined up

to the 02/11/2018 where the deviation is still expected to be smaller than the temporal resolution.

4.2.3 Numerical model SWASH

The numerical model used to study the wave propagation in this very heterogeneous environment is the model SWASH developed at TU Delft [Zijlema et al., 2011]. It is a non-hydrostatic, free-surface, rotational flow model which can be used in one or two horizontal dimensions. SWASH may either be run in depth-averaged mode or multi-layered mode in which the computational domain is divided into a fixed number of vertical terrain-following layers. Each terrain following layer are depth averaged. This model is suited to describe wave propagation in the nearshore domain even in complex environment presenting steep bathymetry and therefore large depth (i.e., kd up to 16 for three layers, with k the wave number and d the still water depth). Wave interaction with the structure is also one of the capabilities of this model.

The governing equations are :

$$\frac{\partial \zeta}{\partial t} + \frac{\partial hu}{\partial x} + \frac{\partial hv}{\partial y} = 0 \tag{4.8}$$

$$\frac{\partial u}{\partial t} + u\frac{\partial u}{\partial x} + v\frac{\partial v}{\partial y} + g\frac{\partial \zeta}{\partial x} + \frac{1}{h}\int_{-d}^{\zeta}\frac{\partial q}{\partial x}dz + c_f\frac{u\sqrt{u^2+v^2}}{h} = \frac{1}{h}(\frac{\partial h\tau_{xx}}{\partial x} + \frac{\partial h\tau_{xy}}{\partial y}) \tag{4.9}$$

$$\frac{\partial v}{\partial t} + u\frac{\partial v}{\partial x} + v\frac{\partial v}{\partial y} + g\frac{\partial \zeta}{\partial y} + \frac{1}{h}\int_{-d}^{\zeta}\frac{\partial q}{\partial y}dz + c_f\frac{v\sqrt{u^2+v^2}}{h} = \frac{1}{h}(\frac{\partial h\tau_{yx}}{\partial x} + \frac{\partial h\tau_{yy}}{\partial y}) \tag{4.10}$$

Where t is time, z pointing upward with $z = 0$ at still water level. ζ is the free surface displacement from the still water level and $h = \eta + d$. u and v are the depth-averaged flow velocities along x and y, respectively. q is the non-hydrostatic pressure (normalised by ρ_{water}), g is gravitational acceleration, c_f is the dimensionless bottom friction coefficient, and τ_{xx}, τ_{xy}, τ_{yx} and τ_{yy} are the horizontal turbulent stress terms. Zijlema et al. [2011]

The friction is a function of the Manning coefficient (n) :

$$c_f = \frac{n^2 g}{h^{1/3}}$$

And the turbulent stress terms are given by:

$$\tau_{xx} = 2\nu_t\frac{\partial u}{\partial x}$$

$$\tau_{xy} = \tau_{yx} = \nu_t(\frac{\partial u}{\partial y} + \frac{\partial v}{\partial x})$$

$$\tau_{yy} = 2\nu_t\frac{\partial v}{\partial y}$$

With the turbulent mixing length model :

$$\nu_t = \ell_m^2\sqrt{2(\frac{\partial u}{\partial x})^2 + 2(\frac{\partial v}{\partial y})^2 + (\frac{\partial u}{\partial y} + \frac{\partial v}{\partial x})^2}$$

SWASH is in constant developments and several features are regularly added. For instance, the mean flow through a porous medium can be modelled by the volume-averaged Reynolds-averaged Navier-Stokes (VARANS) equations. The overall resisting force induced by the porous medium is based on the empirical formula described in Van Gent [1995].

In the following we will use two approaches to model the influence of the blocks on the wave field :

1. one simply based on the bottom friction,

2. and the second, using a porous medium.

4.2.4 Model calibration

In this section the calibration of the numerical model is described. Different set-up will be considered and detailed hereafter (see sections 4.2.4 and 4.2.4).

The performances of the model will be evaluated with two indicators according to Willmott [1981] : the classical Root Mean Square Error and the Willmott score defined as :

$$1 - \frac{\sum_0^n ((P_i - O_i)^2}{\sum_0^n (|P_i - \overline{O}| + |O_i - \overline{O}|)^2}$$

With P_i the model predictions and O_i the observations.

The variable chosen to evaluate the model performance is the significant wave height as it is a key parameter in this chapter. Therefore, all further reference to RMSE and Willmott score in this section are relative to the significant wave height. To calculate the spatial evolution of the significant wave height , the procedure is similar to the one of the measurements except that the Fourier transform is made on the free surface at each point of the domain instead of on the pressure signal. The same frequency range as for measurements is used to determine the first order moment.

Set-up 1 : large domain and calibration on the Manning coefficient

A large first domain stretching between the buoy and the breakwater is first considered (Figure 4.6). This 1250 m long model has a 1 m horizontal resolution. The water column is split in two layers.

Over this domain, several features of the bathymetry are present that can influence the wave transformation, in particular for large period swells. From the buoy to the toe of the breakwater, indeed, the sea bottom is mainly composed of a rocky seabed with irregular patches of sand. The block armour is made of randomly placed 50 tons concrete blocks. In this first set-up, the effect of this complex bathymetry is modelled through the friction coefficient (Manning coefficient). In the simulations, the following values were considered for the Manning coefficient, from 0.005 to 0.015 for the offshore part and from 0.2 to 0.4 in the blocks.

As shown on Figure 4.7, RMSE value does not vary significantly with the Manning coefficient applied to the area before the block armour. For that reason, we choose to consider a conservative value of 0.01 for this part.

Stronger variations of the RMSE are observed with the Manning coefficient in the blocks. For this parameter, the best model performance is obtained with a high Manning coefficient of 0.25.

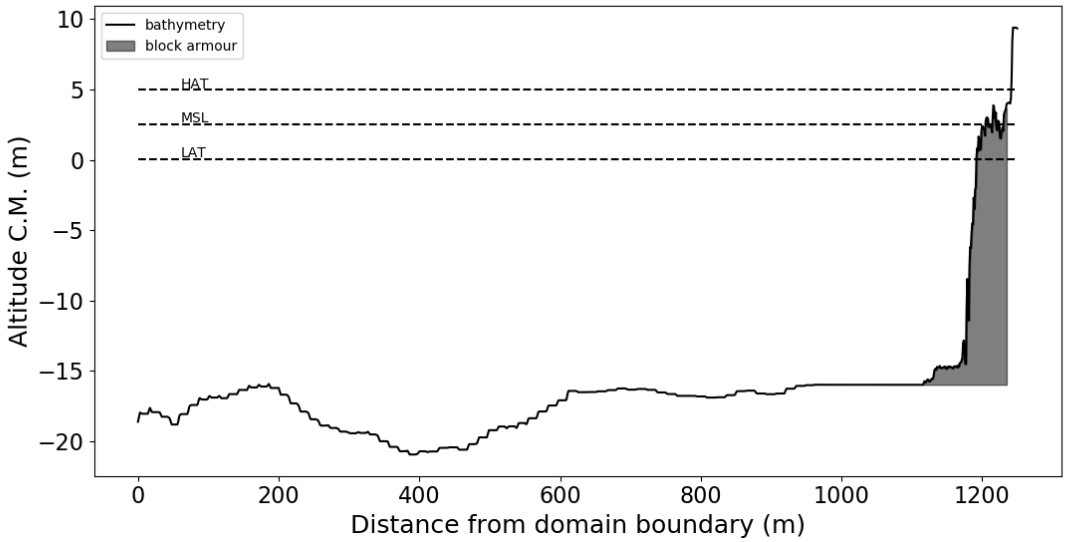

Figure 4.6: Sea bottom variation in the numerical domain extending from the wave buoy to the breakwater

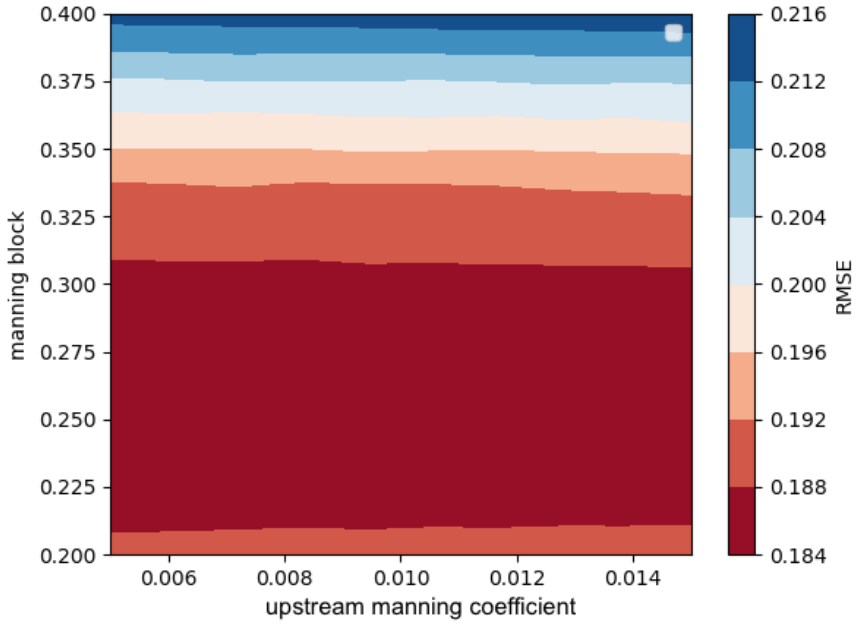

Figure 4.7: RMSE of significant wave height in function of the Manning coefficient in the block armour (y axis) and upstream the block armour (x axis)

Those two coefficients fixed, nine scenarios, covering various conditions of offshore significant wave heights and water levels are simulated in order to evaluate the performance of the model. Note that those scenarios correspond to conditions that actually occurred during the measurement campaign in October/November

2018. The parameters of these nine scenarios are presented in Table 4.2 and Table 4.3.

Strong variations of the normalised RMSE are observed with relatively high values for the first five scenarios (Figure 4.8). It is a bit difficult to understand this result. Nevertheless, we remark that scenarios N7-N9 involve waves coming from a more west direction compared to the other ones. Scenario N6 involves high water level and high waves. The rest of the conditions gives significant discrepancy with the measurements. According to these results, it is likely that the Manning coefficient is not sufficient to describe the complex processes occurring in this area, and especially in the block armour. Consequently, a shorter domain with a porous block armour and a higher resolution is tested in the next section.

n/var	n1	n2	n3	n4	n5
date	10/10 11h	10/10 09h	10/10 07h	10/07 11h	10/07 14h
$Hs_{buoy}(m)$	1.55	1.75	1.52	3.58	3.28
$Tp_{buoy}(s)$	13.33	14.29	13.33	11.76	10.53
θ_{Pbuoy}	306.6	306.4	305.8	318.1	320.6
$MWL_{socoa}(m)$	0.94	2.97	4.31	0.83	2.86
$H_{forcing}(m)$	1.86	1.96	2.05	4.3	4.3
$H_{adv}(m)$	1.60	1.80	1.94	NA	NA
$H_{ps0}(m)$	1.52	1.67	1.92	3.53	3.66
$H_{ps1}(m)$	1.68	1.79	2.00	3.84	3.81
$H_{ps2}(m)$	2.70	2.50	2.22	4.92	4.19
Cr_{3s}	0.14	0.13	0.26	0.48	0.37

Table 4.2: Table presenting the parameter for scenarios N1 to N5

n/var	n6	n7	n8	n9
date	10/07 17h	10/11 13h	10/11 15h	10/11 19h
$Hs_{buoy}(m)$	3.54	0.75	0.80	0.88
$Tp_{buoy}(s)$	10.52	13.33	12.5	11.11
θ_{Pbuoy}	318.6	289.2	291.8	298.3
$MWL_{socoa}(m)$	4.25	0.49	1.25	4.29
$H_{forcing}$	3.6	0.74	0.65	0.76
$H_{adv}(m)$	NA	0.50	0.52	0.72
$H_{ps0}(m)$	3.22	0.58	0.57	0.67
$H_{ps1}(m)$	3.30	0.65	0.59	0.70
$H_{ps2}(m)$	3.34	1.15	0.83	0.85
Cr_{3s}	0.35	0.18	0.22	0.21

Table 4.3: Table presenting the parameter for scenarios N6 to N9

Set-up 2 : high-resolution domain and porous medium

The second set-up extends 50 m from the bottom of the block armour to the top of the caisson (Figure 4.9). This 150 m long domain is meshed with 300 cells, hence a resolution of 0.5 m. The water column is described with 10 layers to better account for the presence of the porous medium. The upstream boundary is set as weakly reflective and the downstream boundary to a Sommerfeld radiation condition [Orlanski, 1976]. With this set-up, a 20 minutes simulation corresponding to a given sea state lasts about 10 minutes on a laptop with 8 Go of RAM at 2.6 GHz.

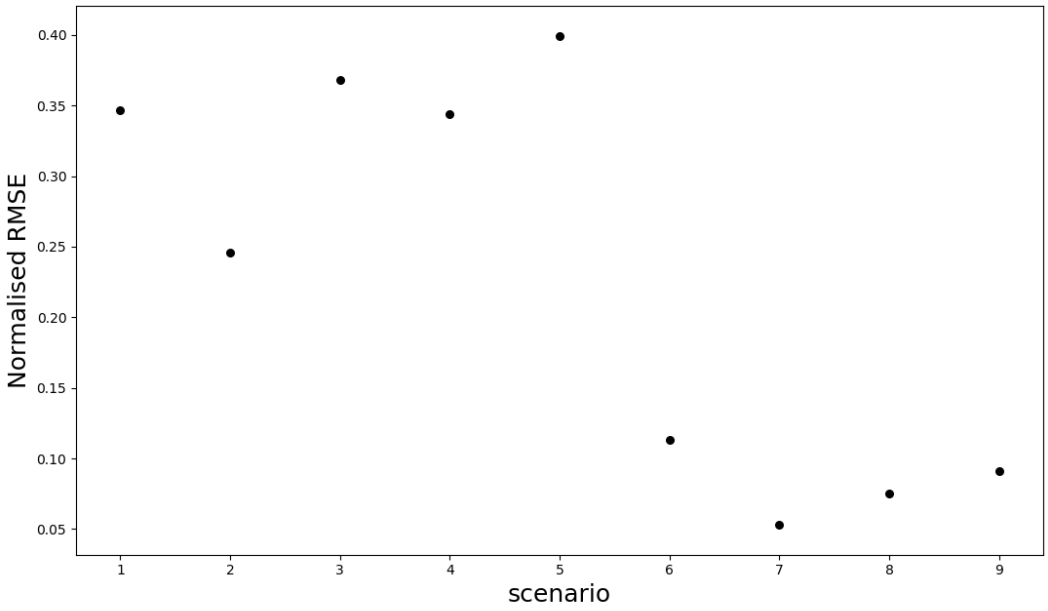

Figure 4.8: Normalised RMSE for each scenario in the large domain simulations with fixed Manning coefficients

The profile presented in Figure 4.9 is an average of twenty profiles spaced by 1m on each side of the sensors axis, and finally smoothed on a 5 points sliding average. The grey area, representing the porous medium, is therefore an envelop of the actual block armour. Note that the inaccuracies due to the positioning technique and to the determination of the profile can explain the apparent vertical shift observed between the position of a few sensors and the upper limit of the porous medium. Nevertheless, considering the overall difficulties to deal with such an harsh environment, the result finally obtained appears acceptable.

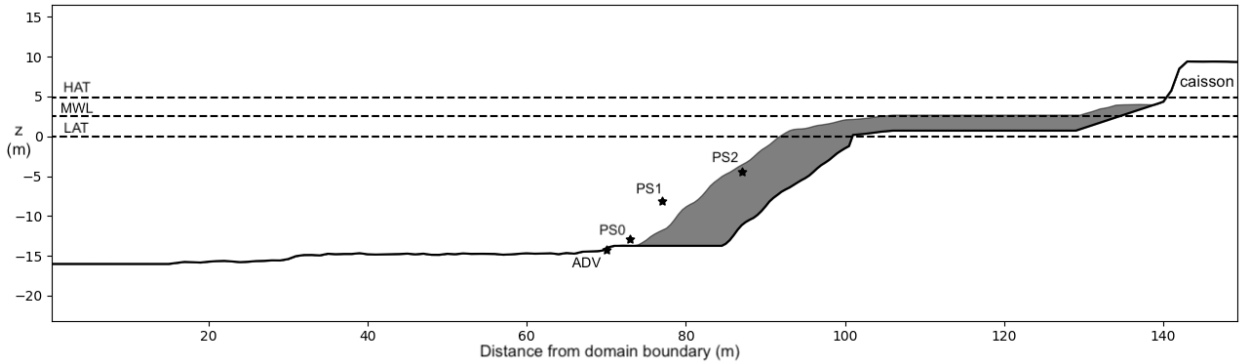

Figure 4.9: Set-up 2 with the porous media in grey and the location of the different sensors.

The blocks protecting the breakwater, which weight 50 tons, are randomly placed and often moved

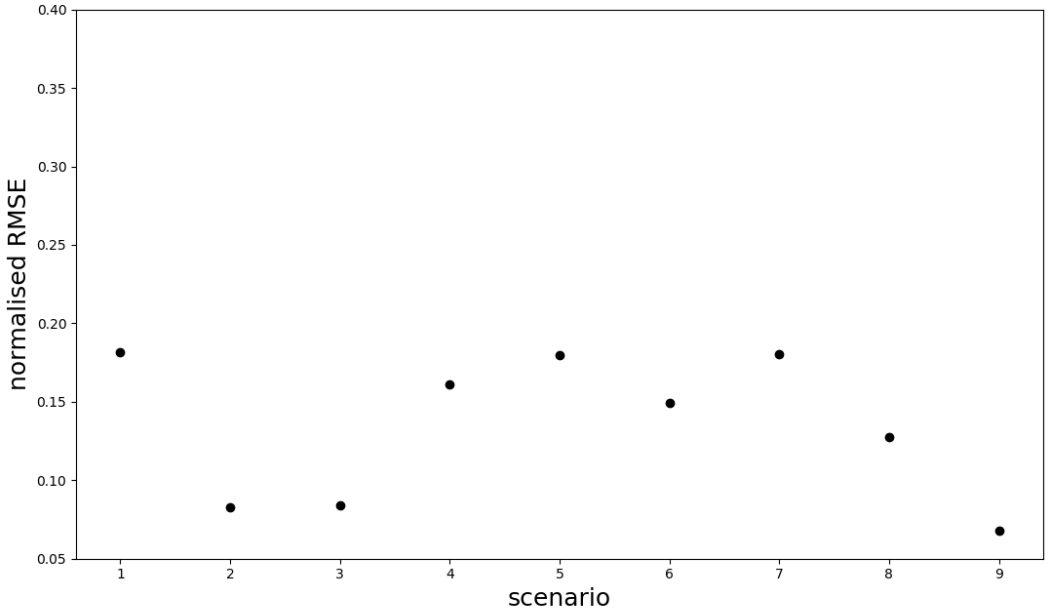

Figure 4.10: Normalised RMSE for each scenario in the high resolution domain

over quite long distance by storms as formerly indicated. Therefore, a detailed scan would be necessary to estimate the porosity field. This extensive work would have been very time consuming. Here, we decided to rely on a constant value determined after testing several values around 0.4, which is usually adopted for block armour. The best performances, with regard to RMSE and Willmott score, were surprisingly obtained with a porosity of 0.25. This unusual low value may be explained by the very heterogeneous aspect of the block armour likely resulting from the procedure employed to drop the blocks (literally dropped from a vessel without further precautions) as well as the strong wave action in this area. This value will be the one used in all the following simulations.

With this shorter domain, the wave parameters measured by the buoy cannot be used directly as forcing. Moreover, the toe of the breakwater, which is the upstream boundary of this second set-up, is submitted to likely strong wave height modulation due to reflection. To solve this issue, we tried to optimise the significant wave height forcing (referred to in 4.2 and 4.3 as $H_{forcing}$). For each scenario, a range of forcing significant wave heights is tested and the value returning the best RMSE and Willmott score, is retained. With this procedure, RMSE between 0.05 and 0.2 are obtained (Figure 4.10), which indicates better and more stable performances than for the long domain (Figure 4.8). Note that to simplify the procedure, we considered the wave period measured at the wave buoy.

4.2.5 Set-up 2 : Numerical reflection, run-up and surf zone extent

The reflection coefficient can also be computed using the numerical model. Here, in order to further compare with the measurements, we first estimated this coefficient using the free surface signal at the location of the

sensors using the same the three probes method as described previously.

In a second time, the profile of reflection coefficient are determined with a sliding three probes method. Starting at the left boundary the three probes is applied at three points spaced by 5 m. The reflection coefficient can be calculated up to 10 m from the furthest submersed point. In the swash zone the reflection coefficient determined with this method is not a reliable parameter.

As indicated previously, to validate the model in the vicinity of the vertical wall, the number of impacts measured by the high frequency pressure sensors will be compared to the number of flooding events (namely, when the free surface reaches the pressure sensor P_0 altitude) computed in the SWASH simulation.

For both the pressure signal (Figure 4.11 (a)) and the simulated run-up at P0 (Figure 4.11(b)), the number of events has been counted with an up and down crossing method. A threshold is also implemented to eliminate the events of low intensity (i.e., impacts of less than 0.01 bar and run-up of less than 10 cm) which bring unnecessary complexity.

The comparison between the number of events is delicate as the two signals are not of the same nature. The sampling frequency is also different (Figure 4.11). Nevertheless, events are related to the wave period, which value is much higher than the sampling rate of both signals. Therefore, even with different sampling rates, the comparison appeared to be possible and relevant.

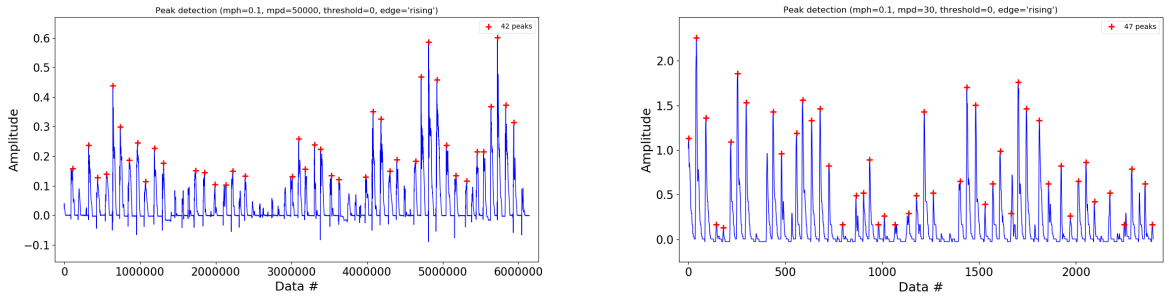

(a) a (b) b

Figure 4.11: (a)Raw pressure signal at sensor P0 on the wall of the Artha breakwater. Each red cross indicates the detection of an impact. (b)Free surface signal at the position of sensor P0 in a SWASH simulation. Red crosses indicate the detection of a flooding event.

The extension of the surf zone in a relevant parameter which can help us better interpret our data including the impact pressures. The SWASH model can be used to give this information. To that purpose, at each time step, unbroken and broken waves are tracked with a binary marker in each cell. The first upstream and last downstream point where wave breaking is detected are extracted, and give the extent of the surf zone for each scenario.

4.3 Results

4.3.1 Experimental results

Wave forcing

The time series of the significant wave height measured at the directional current meter (ADV), PS1 and offshore buoy are presented figure 4.12. The difference between H_s at the directional current meter and at PS1, two locations close to each other, remains small as expected.

Between the offshore buoy and other the sensors, if the trend is similar, there are also as expected non negligible differences.

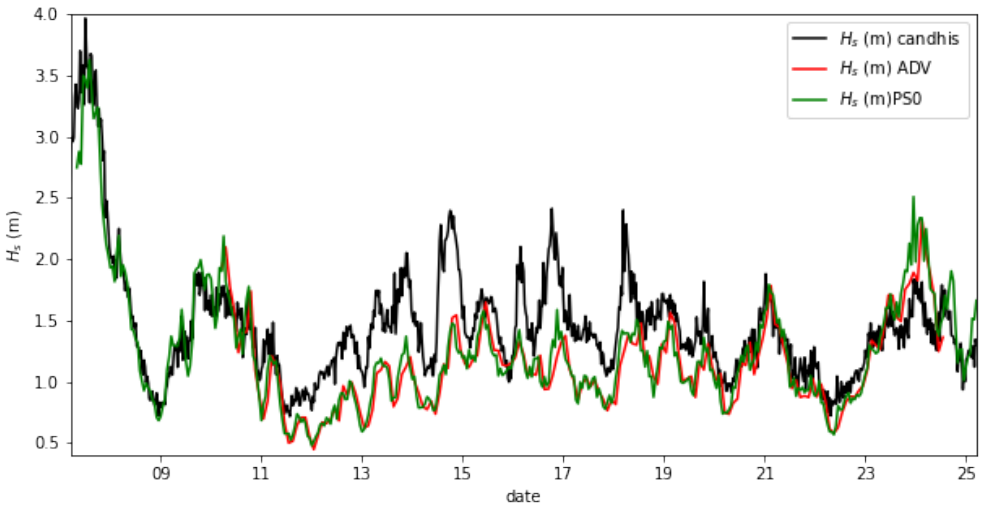

Figure 4.12: Comparison of significant wave heights at the directional wave buoy, at the directional current meter and at PS0 in October 2018. Refer to Figure 4.2 for sensor position.

The variables likely to influence wave propagation between the buoy and the breakwater are : swell direction, period and water level. The scatter plot presented in figure 4.13 discriminates wave direction by varying the colour of the symbol. The sea states with higher energy show two trends which depend on the wave incidence. For the northernmost sea states (i.e. $\theta_p \geq 295°$), the coefficient of the regression line is 0.9 slope with $R^2 = 75\%$; while for the remaining events, less north, the slope coefficient is 0.4 with $R^2 = 44\%$. Hence, for the most western sea state direction, less than half of the variability is explained. Therefore, if the influence of wave direction is obvious, no simple practical law can be drawn from those data. Note that the effect of water level and period was also investigated in a similar way but their respective influence was found weaker.

Wave reflection

Figure 4.14 shows the time variation of H_s at the different sensors installed during the campaign. Two groups with similar behaviour can be identified, namely sensors ADV, PS0, PS1, PS4 on one side and PS2 and PS3 on the other side. The discrepancy observed between those two groups implies that a significant

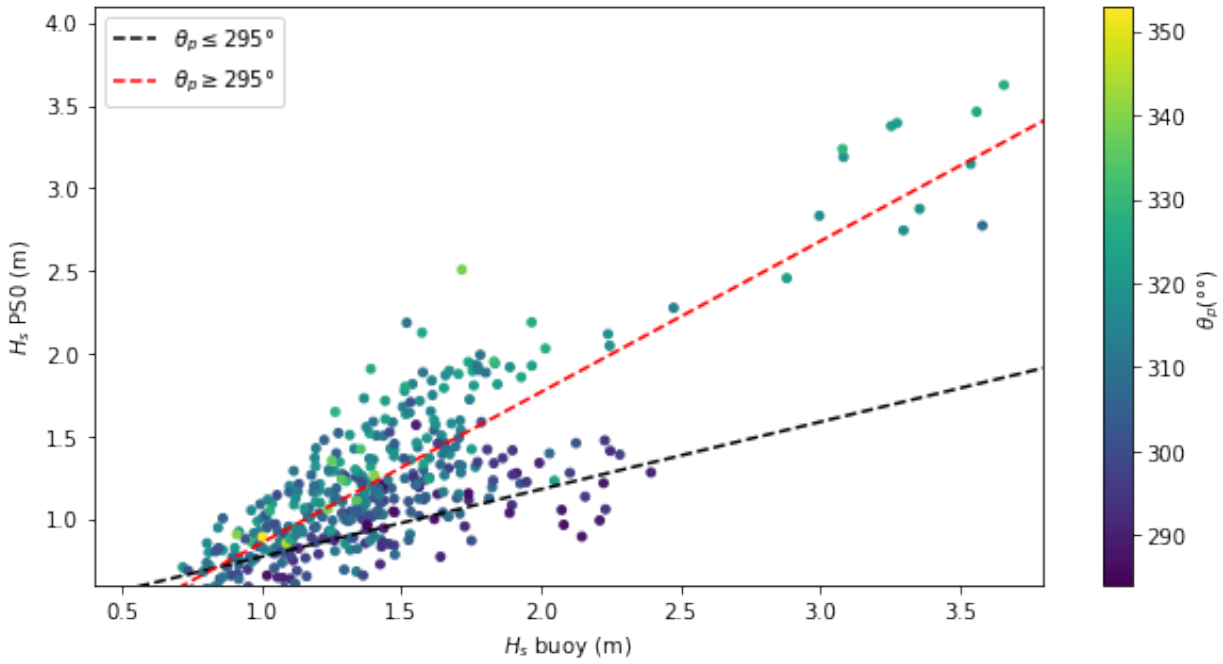

Figure 4.13: Scatter plot of significant wave height at the buoy versus at PS0 with peak swell direction at the buoy indicated in colour. Regression lines differentiating $\theta_p \leq 295°$ and $\theta_p \geq 295°$ are plotted in black and red respectively.

modulation of the wave field is taking place between these 2 locations.

With such rapidly varying bathymetry, reflection is expected to play an important role in the wave field distribution. The reflection coefficient $R_{3S} = H_{Sr}/H_{Si}$ was determined based on the three probes method at sensors PS0, PS1 and PS2 and is represented in Figure 4.15 in function of the water level, including all the data collected in the field campaign. A reflection coefficient between 0.2 and 0.6 is obtained, which is in the expected range [Muttray et al., 1999, 2007]. R_{3S} is indeed found to decrease with increasing water level up to about 3.5m. Beyond this value, the reflection coefficient seems to reach a stable value. The influence of the water level is quite obvious with a R^2 of 71%. The strong dissipation and steep bathymetric variation in the area affect the evaluation of reflection by the three probes method. The value estimated here is not representative of the entire reflection happening at the structure.

4.3.2 Numerical results

Figure 4.16 presents the spatial evolution of H_s for the different scenarios, determined from the raw spectrum of the free surface at each point of the domain. It includes incident and reflective components. The effect of the reflection appears as a modulation of the significant wave height in this figure. The stationary waves generated by the reflection of individual waves (introduced in its simplest form in chapter 2) combines with shoaling effects. Summing the contribution of all the individual waves and considering that the energy is concentrated around the peak frequency result in the sharp peak, observed for H_s, above the top of the steep block slope, and this for almost every case. Nevertheless, the latter appears sharper for lower water levels,

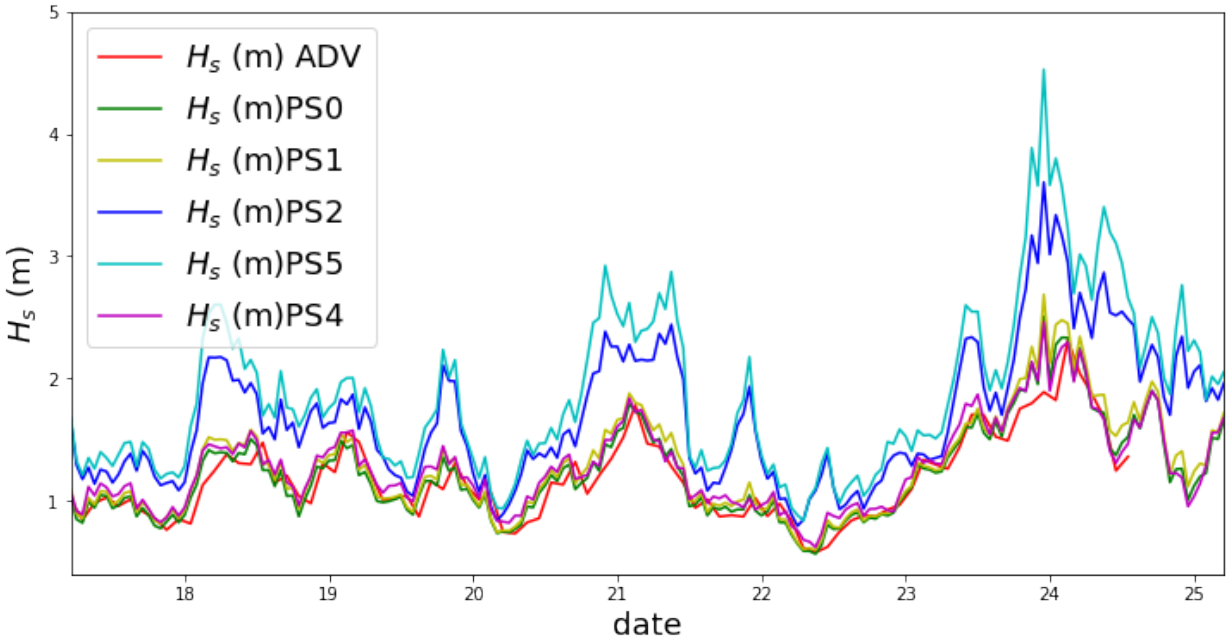

Figure 4.14: (a)Time evolution of significant wave height as measured at the directional current meter and the different pressure sensors in October 2018.

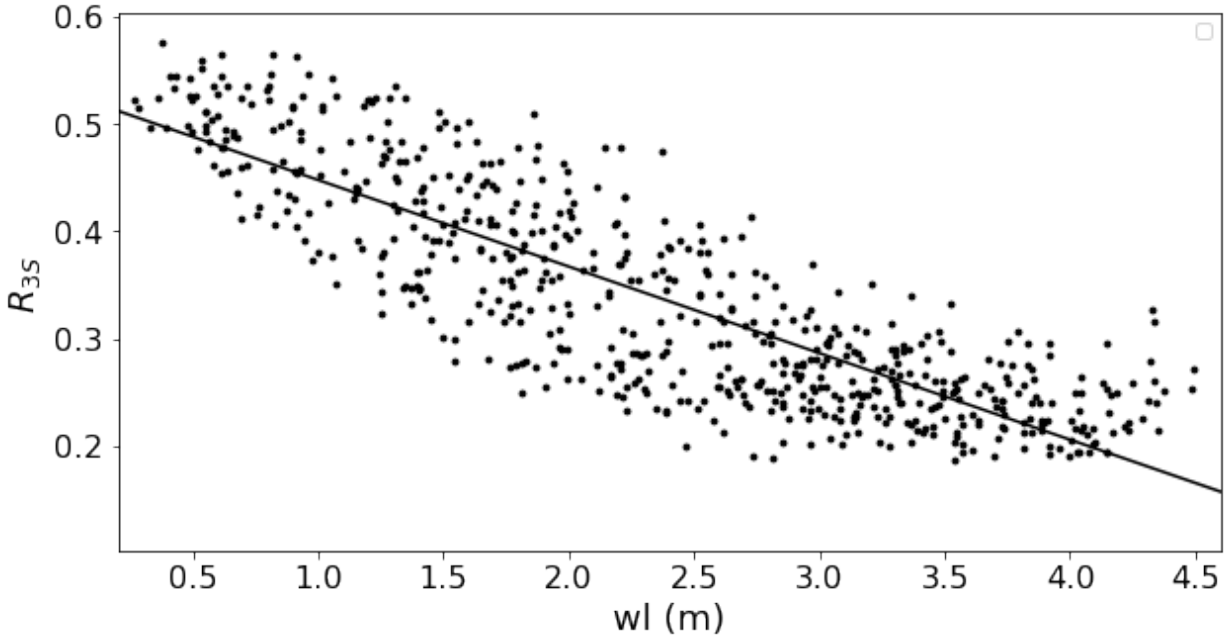

Figure 4.15: Reflection coefficient $R_{3S} = H_{Sr}/H_{Si}$ computed with the three probes method at sensors PS0, PS1, PS2 in function of water level.

for which reflection and shoaling are concentrated on the steep block slope.

The model performance appears satisfactory with an overall better RMSE and Willmott score than with

the initial domain. Qualitatively, as can be seen on Figure 4.16, the model reproduces the trend of the observations quite well, although larger differences are still observed for a few cases.

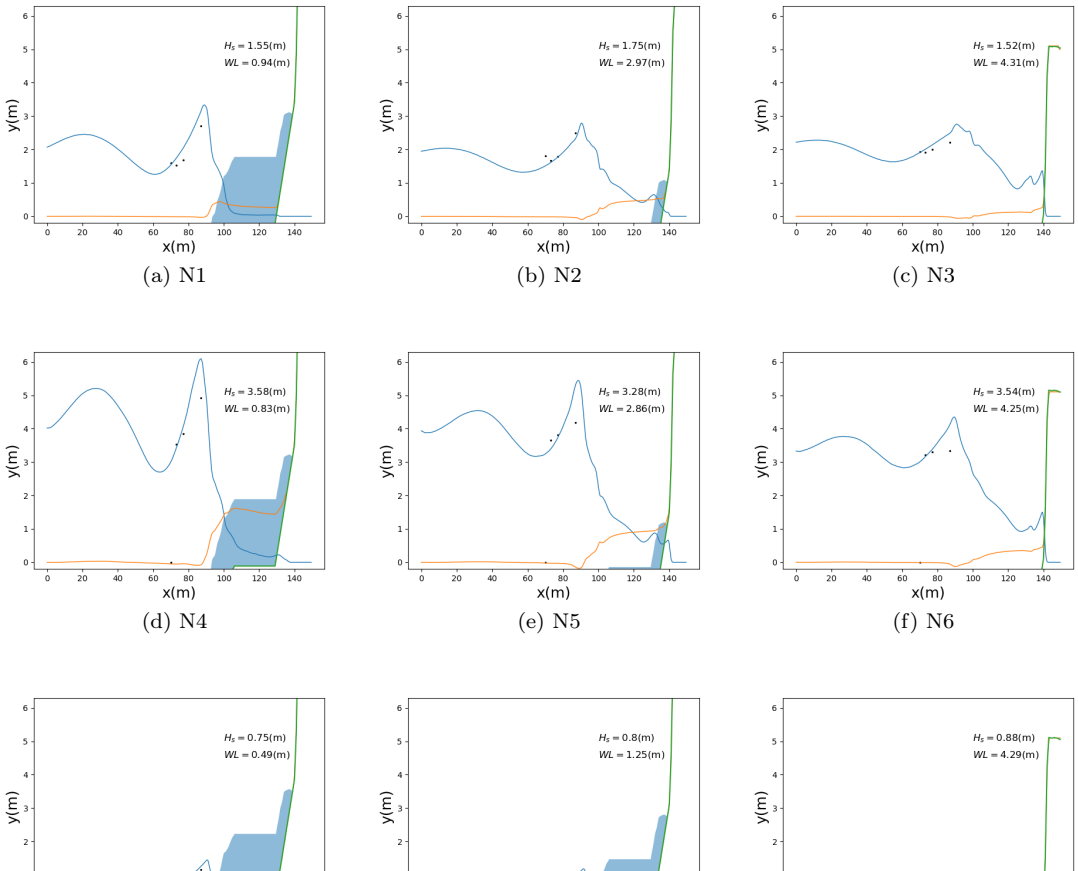

(a) N1 (b) N2 (c) N3

(d) N4 (e) N5 (f) N6

(g) N7 (h) N8 (i) N9

Figure 4.16: Spatial evolution of H_s computed and measured (i.e., at the ADV, PS0, PS1 and PS2 positions) for all the scenarios.

The reflection coefficients computed with the SWASH model considering the three probes PS0, PS1 and PS2 are now superimposed to the observations in figure 4.17. The performance of the model on this aspect appears quite satisfactory (normalised RMSE of 0.16). Therefore, even though the wave field has likely a significant 3D component in this area, the present simplified 2DV approach is shown to reproduce correctly the reflection pattern, and that for the whole range of water levels.

Figure 4.18 quantifies the incident and the reflected H_s using a moving three probes computation on the SWASH results. The sum of incident and reflected H_s appears smaller than the total significant wave height as determined from the raw spectra (i.e., H_{stot}) obtained with SWASH. It is expected as the three probes method does not resolve the phase but rather focus on the amplitude (cf chapter 2) and the phase disappears in the method. As a consequence, the standing wave visible on the raw signal, which is a phase related effect

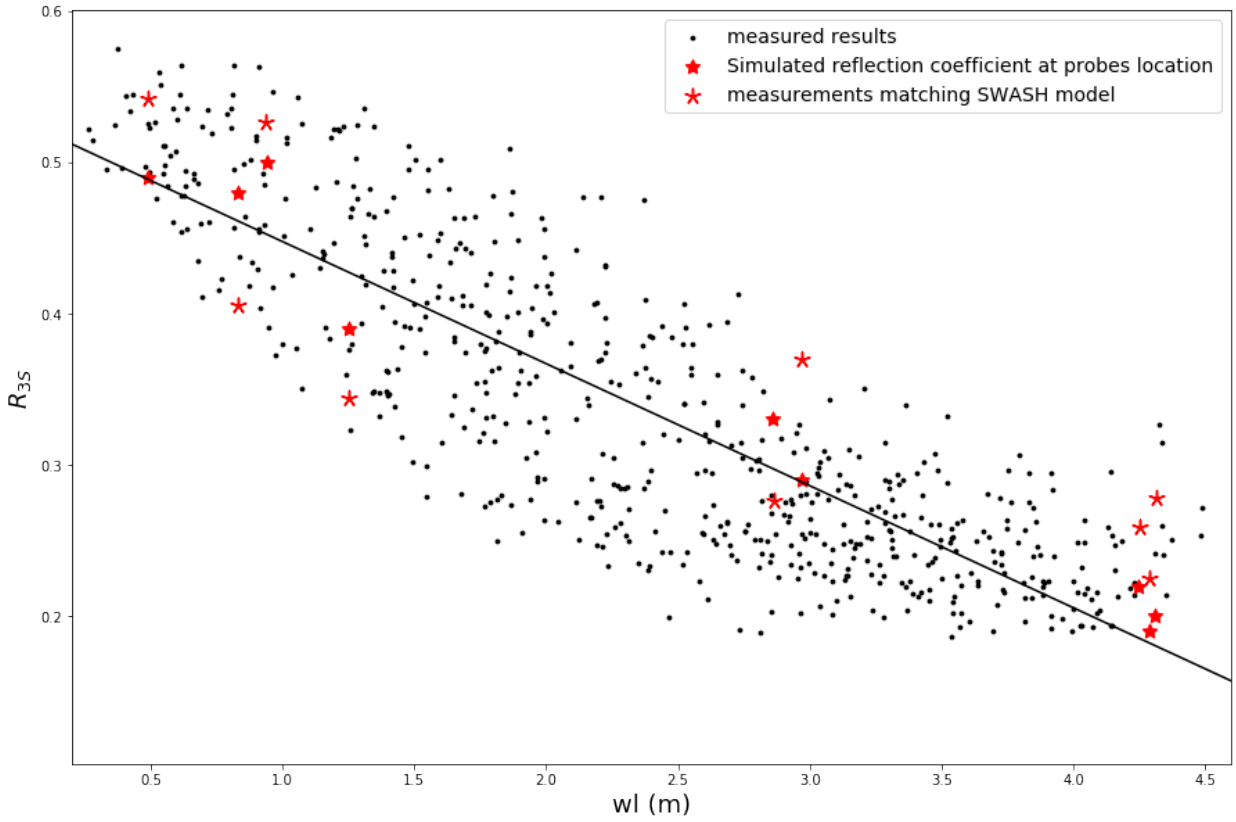

Figure 4.17: Reflection coefficient computed with SWASH for the 9 reference cases superimposed to the measured reflection coefficients

(section 2.5), disappears with the three probes analysis. It is mainly observed on the upstream part of the signal on Figure 4.18 where the spatial modulation completely disappears with the three probes analysis. Over the block armour, the difference between the two analysis becomes smaller as wave breaking becomes likely dominant for the evolution of the significant wave height. The red curve also allows to measure the effect of the shoaling above the mound with the sudden increase of H_{s_i}. The position of the maximum of the blue curve, before the flat part of the bathymetry, implies that there is a strong reflection on the mound slope itself.

The spatial evolution of the reflection coefficient presented in Figure 4.19 is coherent with the former analysis. It also shows that the upstream reflection coefficient is overall lower compared to the rest of the domain. It means that the overall reflection coefficient of the structure is lower than the one measured at the sensors (i.e. x $80m$). This is consistent with the dissipation of the waves starting before the sensors location.

Figure 4.20 presents the number of events detected (i.e., the impacts for the observations and run-up for the model) in function of the water level for the different scenarios. The correspondence between the model and the observation appears satisfactory for low water levels and high water levels. The difference seems more important (about 50%) for intermediate water levels involving impacts such as observed in the scenario number 5 ($H_s = 3.28$ m, $WL = 2.86$ m). We also note that the SWASH results are always under the observed values.

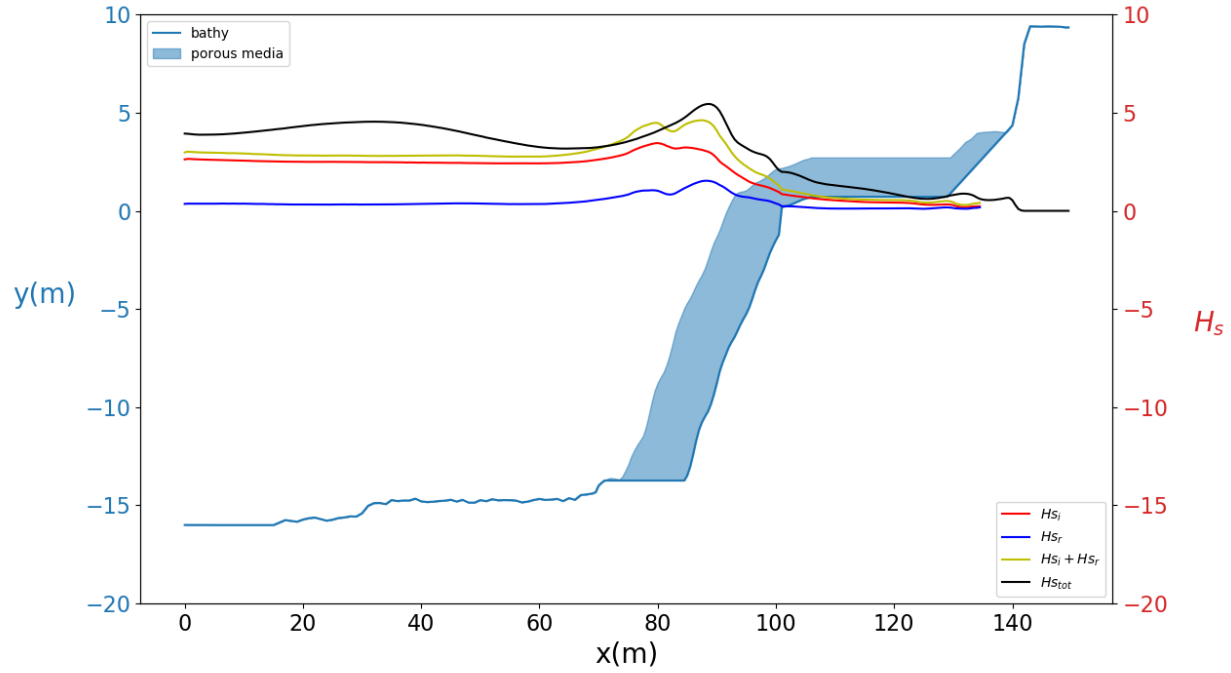

Figure 4.18: Spatial evolution of H_s incident, reflected and the sum of the two, calculated by the three probes methods (resp. Hs_i, Hs_r, and $Hs_i + Hs_r$), and using the raw spectrum given by SWASH (Hs_{tot}) for the scenario N5 ($H_s = 3.28$ (m) $WL = 2.86$ (m)) .

The extent of the surf-zone is presented Figure 4.21. For scenarios 7 to 9 ($H_s \approx 1$ m), wave breaking is only observed for water levels of more than 4 m. For scenario 1 to 3 ($H_s \approx 1.5$ m), wave breaking is occurring at the top of the steep part of the block armour and is quickly dissipated. Finally, for scenarios 4 to 6 ($H_s \approx 3.5$ m), for the lowest water level, broken wave are dissipated before reaching the vertical wall while the surf-zone is shifted downstream with higher water levels. When wave breaking is detected (i.e. scenario 1-6 and 9), the peak of H_s seen on Figure 4.16) is located on the upstream part of the surfzone as defined in Figure 4.21.

4.4 Discussion

4.4.1 Wave forcing

Pressure measurements were conducted in the block armour of a composite breakwater. Five pressure sensors out of six initially placed have been recovered. The directional current meter could only be used as a pressure sensor. The measurements cover a wide range of conditions with offshore significant wave heights of more than 4m at the beginning of the experiment.

The analysis of the data showed that the transfer function from the offshore domain to the toe of the breakwater is complex. The offshore spectral parameters are all likely to interact in a different way with the complex bathymetry between the buoy and the breakwater. The significant influence of wave direction has

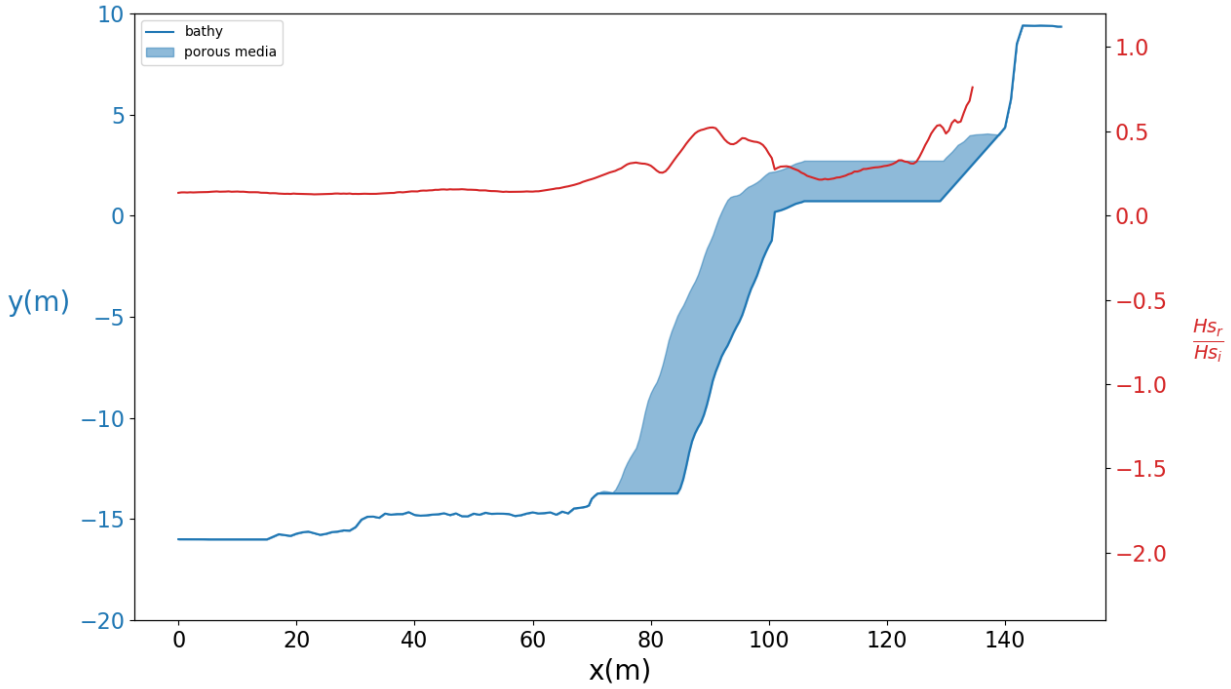

Figure 4.19: Spatial evolution of the reflection coefficient for scenario N5

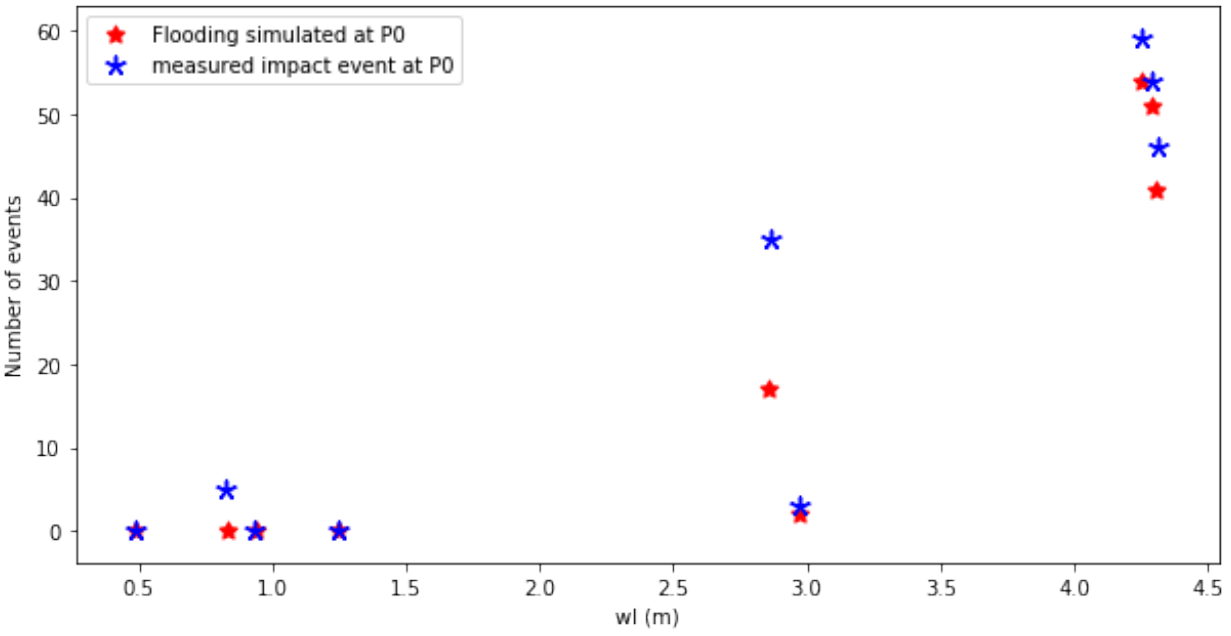

Figure 4.20: Number of flooding events in the SWASH simulations versus number of impact measured on the wall

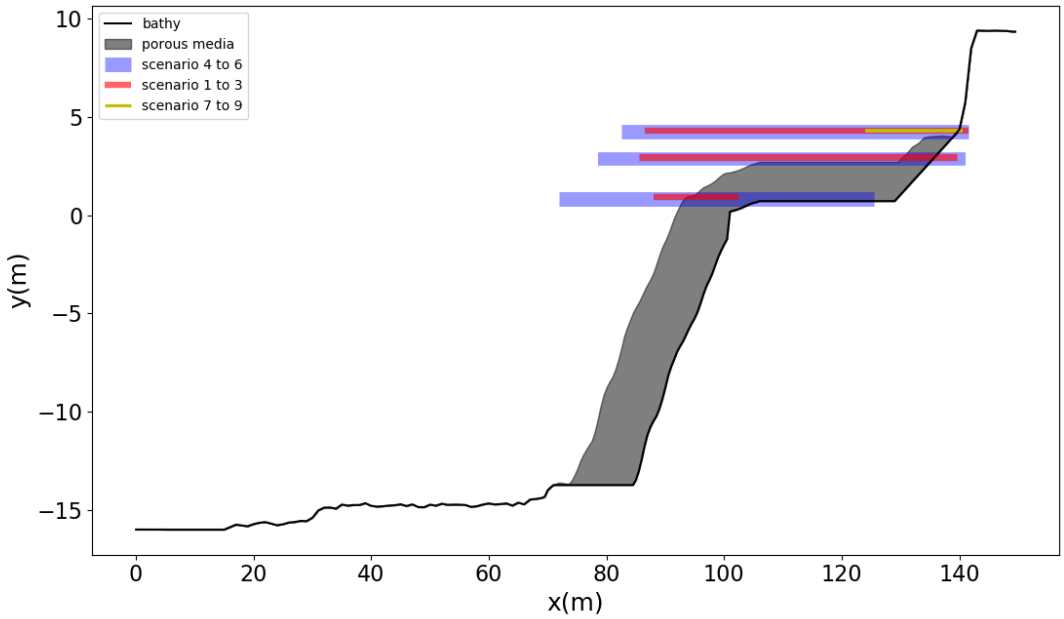

Figure 4.21: Extent of the surf-zone for each scenario. The width of the line stand for significant wave height at the buoy and altitude of the line is the water level of the corresponding scenario.

in particular been shown.

A simple 2DV numerical model (SWASH) has been implemented using a porous medium to represent the block armour. One of the main limitation of this approach is the uncertainties of the wave forcing. The bathymetry offshore of the Artha breakwater is complex and various parameters influence wave propagation from the offshore domain to the breakwater area. A 3D model, able to account for the effects of the complete bathymetry, is currently being setup, but it is heavy in terms of computation time and, for that reason, the 2DV approach keeps some interest. Especially considering that despite the limited knowledge on the forcing and on the structure porosity, the 2DV SWASH model was able to reproduce the main features of the measurements.

4.4.2 Hydrodynamics in the block armour

The effect of water level on wave reflection was clearly shown. Interestingly, an inflection point around water levels between 3.5 m and 4 m (i.e. the berm level) can be identified on Figure 4.17. Up to the level of the berm, the reflection coefficient is regularly diminishing likely due to an increased dissipation of energy in the block armour (see bathymetry profile Figures 4.23 and 4.4). Very few observations are available above this level, but the reflection coefficient in that water level range is more stable and might even increase with the highest water level. In these conditions involving large depths, waves reach more easily the reflective vertical wall. The evolution of reflection with water level is also quite well reproduced by the model. It implies that reflection is mainly controlled by cross-shore processes as the current model is run on a single profile.

The reflection coefficients were determined by the three probes method at sensors PS0, PS1 and PS2.

These sensors were fixed on the concrete blocks where dissipation is shown to be important (Figure 4.21). This reflection coefficient is therefore not representative of the global reflection happening along this transect. The spatial evolution of the reflected wave suggests that there is a strong reflection on the steepest part of the block armour (Figure 4.18).

The model gave correct results regarding the run-up on the vertical wall which is the last stage of the wave propagation in our particular case study (i.e., considering the incident wave). In the field measurements, the proxy for the run-up was the number of impacts at P0 (i.e., the lowest high frequency pressure sensor). Impacts and flooding events show consistency for most of the cases studied. Nevertheless, an impact on a wall usually implies very fast upward vertical motion of water that cannot be properly taken into account by SWASH. This complex hydrodynamics is likely to have an influence on the reflection process. To describe such processes, higher grade models like full Navier-Stokes VOF models could be used but again at the cost of heavy CPU.

The extent of the surf zone (Figure 4.21) confirms that energetic waves actually break above the steep slope of the block armour. Therefore, we can safely assume that most of the impacts signals recorded, were generated by broken waves. This is an interesting fact which explains the relative low pressure values collected. Our database is therefore representative of a broken waves environment with very energetic conditions. To our knowledge, this is the first time that such a comprehensive database is proposed.

But this does not imply that non-broken wave impacts cannot occur. Indeed for the highest water levels when the vertical wall is in the surf zone, some moderately energetic waves could be able to propagate up to the wall and break directly at this place. These rare events may exmplain the outliers impact observed in chapter 3.

4.4.3 Comparison with Goda's formula

With a better knowledge of the wave field in the area, and thanks to the model set-up, it is now possible to compare the results of the statistical model with existing empirical formula widely used in engineering. For instance, the formula established in Goda [1975] gives the wave impact pressure and force on the vertical wall of a breakwater given design wave conditions. It was calibrated based on 21 sliding and 13 non-sliding upright sections of prototype breakwaters case study. The original Goda formula was later revised in Takahashi [2002] to take the impulsive pressure into account.

Additionally, the non linear statistical model developed in chapter 3, can give an acceptable prediction of the maximal pressure expected over 10 minutes. It was shown to be reliable especially for the most frequent impacts, namely those likely involving broken waves, associated to relatively slow impact pressure signals.

Moreover, this statistical model somehow integrates all the information included in our dataset. Therefore, a comparison with a design formula which rely on a static equivalent pressure concept representing the envelope of the load seems relevant to us.

The specificity of the Artha breakwater geometry are observable when comparing Figures 4.22 and 4.23. Among the geometrical parameters used for the determination of p_1 (i.e., the maximal pressure on the wall as proposed by Goda), the value of h is obvious but the parameter d is not as easy to define. For simplicity sake, we choose $d = MWL - 2$ m, which is the approximate average altitude of the flat part of the block armour (i.e. the berm). The large width of the flat block armour part is also well identifiable while it is not present in the case of a standard composite breakwater as seen in Figure 4.22. Parameters B and h_c are

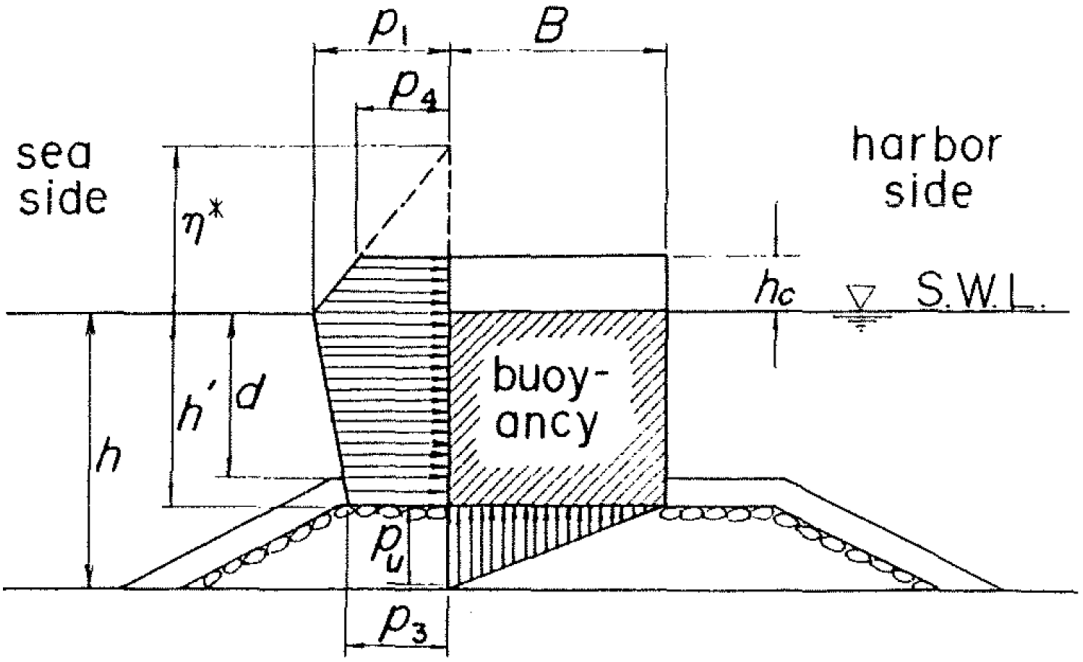

Fig. 4.21 Goda pressure formula

Figure 4.22: Sketch of the parameters used in the Goda formula on a standard composite breakwater [Takahashi, 2002]

presented in Figure 4.23 but not used in the determination of p_1.

Obviously, the singular design of the Artha breakwater and the limited extend of the sensor array are two limitations for this comparison.

In Goda's formula, the maximal pressure p_1 is expected at the mean water level [Goda, 1975, Takahashi, 2002]. It mostly depends on the so-called "design wave height" (H_d), defined as *"the highest wave height expected under the given wave condition"*[Goda, 1975] and *"the wave height and length applied to calculate the design wave forces are those of the highest wave in the design sea state"*[Takahashi, 2002]. Based on the numerical model presented in this chapter, it is possible to provide an evaluation of this parameter. The maximal wave height was determined for the nine reference cases. An additional case, with the following parameters : $Hs = 5$ m, $Tp = 14$ s, $wl = 4$ m, was also investigated to test more critical conditions. Nevertheless, note that even though coherent values were obtained, our model is not validated for this set of conditions.

The maximal wave height generated in the model is evaluated at the point where the maximal significant wave height is observed. This point can vary depending on the scenarios. Beyond this position, a decrease of the significant wave height is observed. At the point of maximal H_s, all the waves in the time series are identified by up and down crossing and H_{max} is extracted. The pressure on the wall according to the Goda

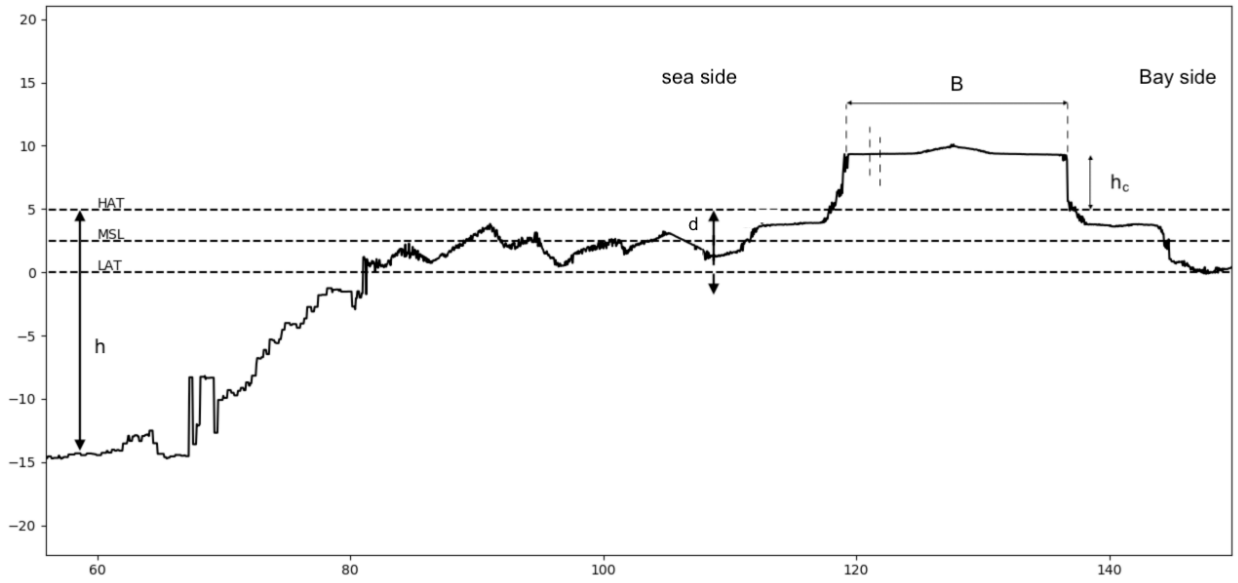

Figure 4.23: Raw profile of the western roundhead of the Artha breakwater along the axis of the pressure sensors. The parameters used in Goda's formula are indicated when the mean water level is at the highest astronomical tide level.

formula is then obtained following the procedure indicated in Takahashi [2002].

Chapter 3 has provided a statistical model aiming at predicting the maximal pressure expected on the section of the Artha western roundhead equipped with sensors. The significant wave height, peak period, peak direction and water level of the nine scenarios of this chapter are well known and can be used as input in this model. On the other hand, with the SWASH estimated maximal wave height, we now have all the parameters necessary to apply the Goda formula. The comparison between the two is displayed in figure 4.24.

The Goda's formula prediction increase almost linearly with H_{max} and depends only weakly on the water level. It means that H_{max} is not very sensitive to the water level as Goda's formula depends mainly on H_{max}. The statistical model, representative of the measurements, shows that P_{max} depends strongly on the water level but not only through H_{max}.

The predictions of the statistical model are globally lower than the predictions of the Goda formula, in particular for the largest waves (Figure 4.24). This was somehow expected, as the Goda formula was designed to evaluate the structural stability of breakwater and therefore must stay on the safe side. A significant overestimation by the Goda formula is mainly observed for $H_{max} > 4$ m, but for the three scenarios with smaller waves the predictions are much closer. With the statistical model, the influence of water level is obvious and appears very significant although variable for different H_{max}. In the case of $H_{max} > 6$ m, we also note that the safety margin of the Goda formula with respect to the statistical model is smaller for high water levels.

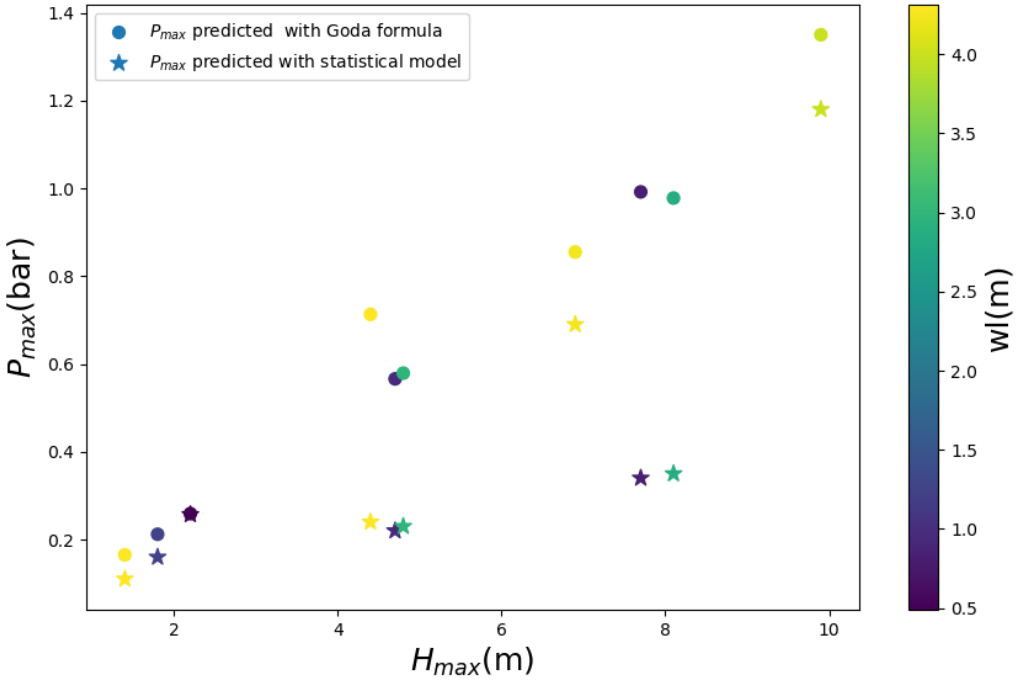

Figure 4.24: Maximal pressure predicted on the Artha wall according to the Goda formula (points) and to the non-linear statistical model (star)

It must also be underlined that the Goda formula was calibrated on breakwaters that have a classical geometry not like the Artha breakwater, characterised by an unusual berm. This is likely a source of difference between the two models.

The sensor array employed in the experiment is also likely to miss the highest pressures for a given impact, especially when aerated or highly impulsive impacts occurred. Nevertheless, the latter are rare and therefore have a very small weight in the statistical model. They are also not As shown in the previous chapter, they mainly generate very localised peaks which yield a small increase to the overall instantaneous force and force impulse, (cf chapter 3)

4.5 Synthesis

A field campaign has been conducted in the block armour of a composite breakwater. The results have shown important variation of the significant wave height in this area. These variations can be explained by a strong reflection on the steep foreshore. The results of the SWASH model are in good agreement with this hypothesis and the measurements. Reflection appeared to be correlated with water level for both, the model and the measurements. The model was then used to estimate the largest wave in front of the breakwater in nine cases for which the model has shown good coherence with the measurements and one additional storm case. Based on this estimate, a comparison between the result of the statistical model established in

chapter 3 and the Goda formula [Goda, 1975, Takahashi, 2002] return values globally of the same order with an overall overestimation by the formula. Nevertheless, the safety margin depends on the waves and water level conditions. It appears from this comparison, that P_{max} does not only depends on H_{max} even taking into account the dependency of H_{max} with the water level.

4.5.1 Perspectives

The first and main perspective for this chapter is the need for a 3D numerical model in order to determine the transfer function from the offshore buoy to the toe of the breakwater. Such a model will reduce the uncertainties concerning the forcing. The remaining unknown would then be the porous medium. A more precise knowledge of this medium would allow to fully evaluate the capacity of this type of model to reproduce the phenomenon measured during the campaign. While the results obtained here have shown acceptable agreement with the measurements, potential 3D effects have to be further investigated. With a better validation of the model, a wider range of conditions could be simulated, and in particular, the most extreme cases.

Chapter 5

Wave impact on cylinder with small wave height to radius ratio, a numerical investigation

Contents

5.1 Introduction

In chapter 3, the influence of external parameters on impact pressure was demonstrated. Given the variability of the phenomena, a detailed study of the wave field in the block armour was conducted in chapter 4. This allowed to provide an estimate for the biggest wave expected at the toe of the breakwater, for a given sea state. Based on that parameter, a comparison between the wave load predicted by the Goda formula [Goda, 1975] and a statistical model build on in-situ measurements at the Artha breakwater was proposed. It

showed that Goda's formula always overestimates the predictions of the statistical model. This is a logical conclusion as the purpose of Goda's formula is the design of the breakwater.

Nevertheless, other elements, and in particular the curved shape of the roundhead, are susceptible to play a role in the discrepancy highlighted. The statistical model is indeed based on measurements on this particular area of the breakwater. The effect of this shape on the pressure distribution has therefore to be studied. In this chapter, this work will be carried out numerically by using a Navier-Stokes model.

The literature on wave interaction with cylinders is wide. Indeed, piles are a very common structure in maritime engineering. Morison et al. [1950] first proposed a formula for engineering purpose, still currently extensively used. Nevertheless, this formula is not meant to describe specific cases in which much higher forces could be obtained especially due to breaking waves [Sawaragi and Nochino, 1984].

The literature review shows that the maximal line force for a breaking wave impact on a cylinder is often written as [Wienke and Oumeraci, 2005] :

$$f_i = C_s \rho R V^2 \tag{5.1}$$

With ρ water density, R cylinder radius and V the wave celerity. C_s is called the slamming coefficient, which in Wagner [1932] is equal to 2π and in Von Karman [1929] to π. The difference is due to the fact that The von Karman model does not account for deformation of the free surface. This deformation causes earlier immersion of the cylinder, resulting in a decrease of the impact duration and consequently, an increase of the impact peak pressure. This phenomenon is included in the model of Wagner. The latter developed a solution for the peak pressure when a solid object impacts a liquid in 2D, which results in $C_s = 2\pi$.

Goda et al. [1966] proposed the following widely-used formula to calculate the impact force of breaking waves on piles :

$$F_i = \lambda \eta_b \pi \rho R V^2 (1 - \frac{V}{R} t) \tag{5.2}$$

With $\lambda \eta_b$ the height of the impacted area and t, the time since the beginning of the impact.

Following Fabula [1957] and Cointe and Armand [1987], Wienke and Oumeraci [2005] showed that the impact force of breaking waves on cylinders could generate significantly higher forces compared to non breaking waves. This work was further improved by Ghadirian and Bredmose [2019]. In all these studies, the cylinder radius was relatively small compared to the wave dimensions (wave length and wave height).

In the case of an impact on a breakwater round head, the radius to wavelength ratio may be limited but not the wave height to diameter ratio. For example, the radius of the Artha breakwater roundhead is equal to 12 m and the vertical wall of the round head is 5.4 m high. As maximal waves of about 10 m can be expected in this area, the maximal impacting height to radius ratio is therefore 0.45 at the Artha breakwater (the whole wall being impacted), which is not included in the usual range studied. Therefore, in the present chapter, the focus will be on small impacting height to cylinder radius ratio, representative of the specific problem studied in this thesis. Additionally, breaking waves are considered as they are known to generate the most violent impacts. In particular, one of the goal of this work will be to test the validity of equation 5.2 for different diameters.

To carry out this study, simulations with the interFoam solver of openFoam are conducted. The latter model has been previously used to simulate wave structure interactions [Deshpande et al., 2012, Jacobsen et al., 2014, Brown et al., 2016]. Additionally, wave impacts on cylinders have already been simulated with waves2foam solver [Paulsen et al., 2013], which derives from interFoam. The ratio of the forced significant

wave height to cylinder radius is of 1.6 in their study whereas Cao et al. [2011], reported numerical tests with ratio of 1 or less, but in deep water and with waves far from breaking.

To test the effect of curvature on wave impact pressure, 3D wave impact simulations on a quarter of cylinder will be performed for varying diameters. In part 2 of this chapter, the numerical model, a validation case and the numerical setup are presented. In part 3, the results of the validation and the sensitivity of pressure and inline force to the obstacle diameter are shown as well as a comparison with Goda's formula [Goda et al., 1966] for the inline force.

5.2 Methods

5.2.1 Model description

The interFoam solver allows to simulate 2 incompressible, isothermal, immiscible fluids using a VOF method [Versteeg and Malalasekera, 2007, Ferziger et al., 2002]. The governing equations are the coupled continuity and momentum equations :

$$\frac{\partial(u_j)}{\partial(x_j)} = 0 \tag{5.3}$$

$$\frac{\partial(\rho u_i)}{\partial(t)} + \frac{\partial}{\partial(x_j)}(\rho u_j u_i) = -\frac{\partial(p)}{\partial(x_i)} + \frac{\partial}{\partial(x_j)}(\tau_{ij} + \tau_{t_{ij}}) + \rho g_i + f_{\sigma i} \tag{5.4}$$

Where u is the velocity, g_i the gravitational acceleration, p the pressure and τ_{ij} and $\tau_{t_{ij}}$, the viscous stresses. The density ρ is defined as follows:

$$\rho = \alpha\rho_1 + (1-\alpha)\rho_2 \tag{5.5}$$

With α the indicator function, equal to 1 within the phase of density ρ_1 and 0 within the phase of density ρ_2. The same equation holds for the viscosity. The surface tension $f_{\sigma i}$ is modelled as :

$$f_{\sigma i} = \sigma\kappa\frac{\partial\alpha}{\partial x_i} \tag{5.6}$$

where :

$$\kappa = -\frac{\partial n_i}{\partial x_i} = -\frac{\partial}{\partial x_i}\left(\frac{\partial\alpha/\partial x_i}{|\partial\alpha/\partial x_i|}\right) \tag{5.7}$$

The displacement of the interface is controlled by :

$$\frac{\partial\alpha}{\partial t} + \frac{\partial(\alpha u_j)}{\partial x_j} = 0 \tag{5.8}$$

The interface sharpness is ensured by the multidimensional universal limiter with explicit solution described in Deshpande et al. [2012]. The setting for this model are based on the openFoam reference case of the damBreak. The density of the two fluids are defined as $\rho_{water} = 1000\ Kg.m^{-3}$ and $\rho_{air} = 1\ Kg.m^{-3}$, and dynamic viscosity $\nu_{water} = 10^{-6}Kgm^{-1}s^{-1}$ and $\nu_{air} = 1.48 \times 10^{-5}Kgm^{-1}s^{-1}$. The surface tension term : $\sigma = 0.07Nm^{-1}$. The flow is considered laminar. The time step is let adjustable in function of a

maximal Courant number ($co = u_i \Delta t / \Delta x_i$) equal to 0.5

5.2.2 Comparison with a potential flow simulation Scolan [2010]

In Scolan [2010], an extensive study on a flip-through impact is conducted and provides a detailed understanding of the physical processes involved, including acceleration and localised pressure peaks. A comparison between the potential flow model used by Scolan [2010] and InterFoam is conducted here to determine the validity of the latter to reproduce the physics of the flip-through impact. The VOF model is run on a Cartesian mesh of 1000 x 800 cells. In this 2D domain, the lateral and bottom boundaries are walls with a no slip velocity condition and the upper boundary is open. Like in Scolan [2010], the free surface profile is initiated by equation 5.9, as can be seen in Figure 5.1, where later stages of the simulation are also shown.

$$y = h + Aexp(-N(x - L) * *2), 0 < x < L \tag{5.9}$$

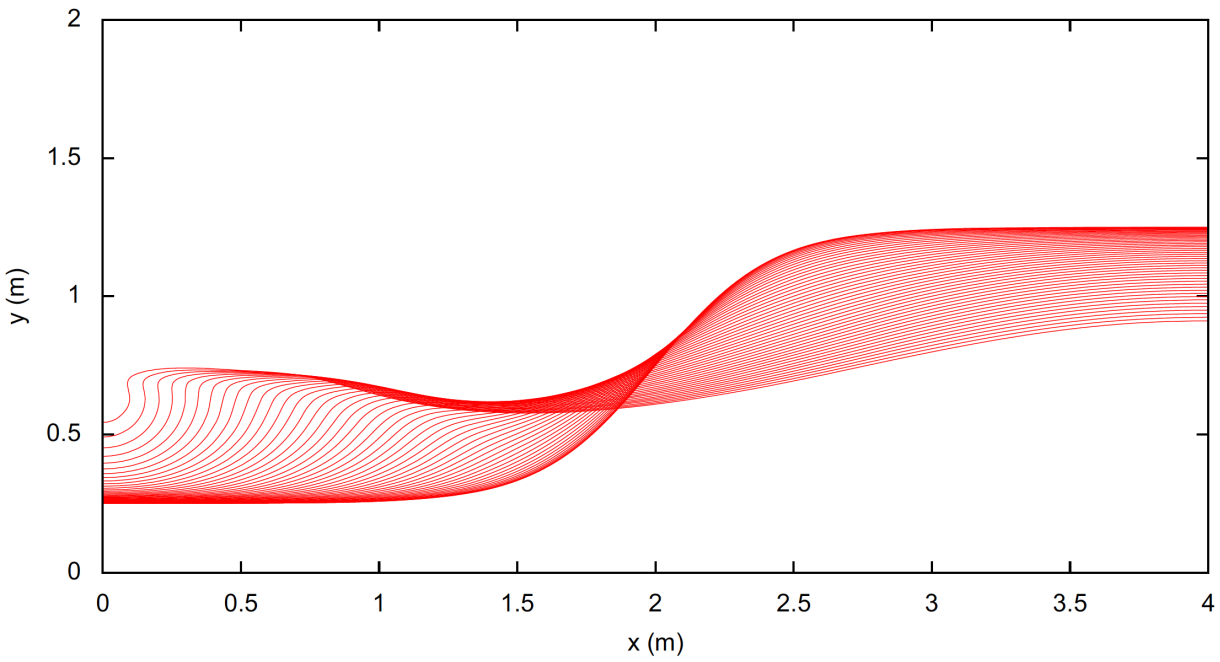

Figure 5.1: Wave profiles obtained in Scolan [2010] with initial condition is given at 5.9.

The validation is conducted with the following parameters for equation 5.9: $h = 0.16$ m, $A = 1$ m, $R = 0.5$ and $L = 4$ m. This setup is finely tuned to create a flip through impact. This impact, at the limit between a sloshing impact and an impact with entrapped air is characterised by high upward velocities on the wall and a very sharp pressure peak at the convergence between the trough and crest of the impacting wave. The parameters investigated for the validation are the interface shape and the impact pressure on the wall.

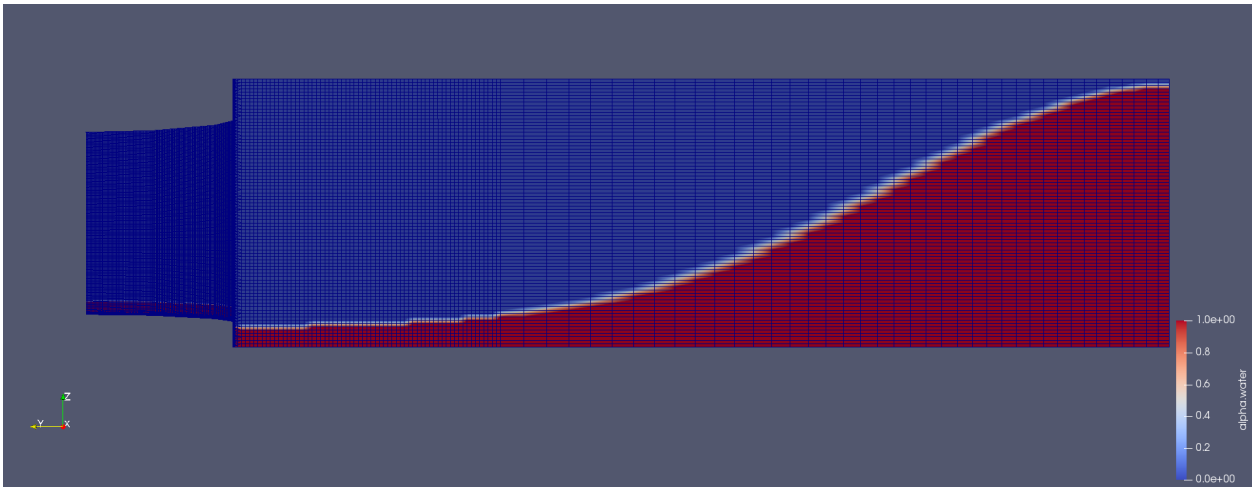

(a)

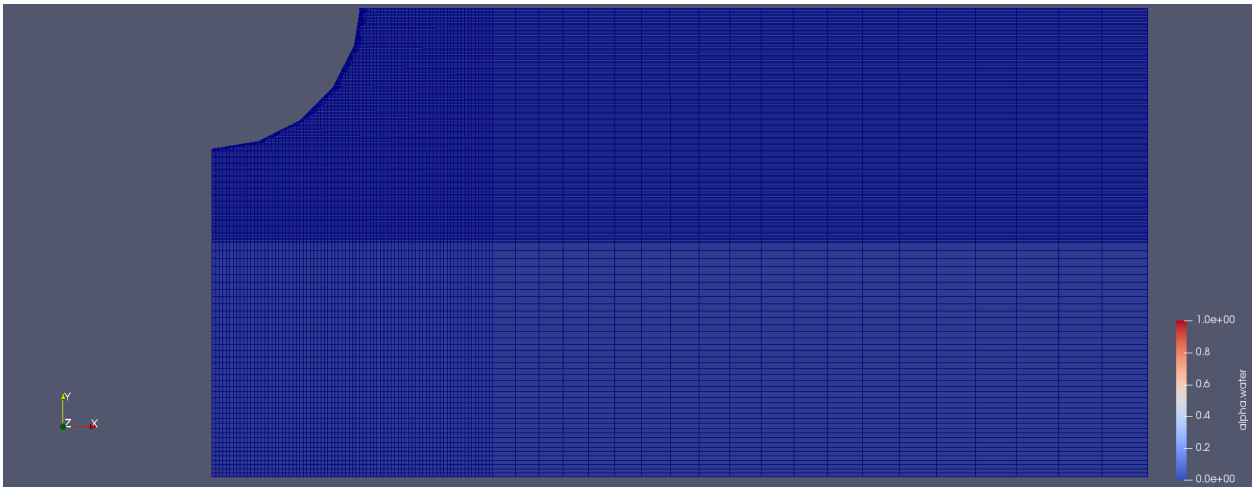

(b)

Figure 5.2: a): side view of the numerical domain with the initial free surface. b): Top view of the numerical domain

5.2.3 3D Numerical setup

The 3D numerical domain is initially defined as a $2 \times 1 \times 0.2\ m^3$ box with $150 \times 200 \times 80$ cells and 30% of the x-direction containing 80% of the cells while the remaining part has an expansion ratio of 2 (Figure 5.2). The cells distribution in the y-direction is such that 50% of the domain contains 80% of the cells and the remaining part has a factor 2 expansion ratio. With the snappyHexmesh tool, the fully parallel, split hex, mesh generator of openFoam, a quarter of cylinder is removed so that the xz plan tangent to the cylinder sit at $y = 0.7$ m (Figure 5.2).

15 simulations were conducted with radius between 0.10 m and 1.52 m to cover a wide range of wave height to radius ratio. The initial free surface is set with the same relation as for the validation case (Equation 5.9) but with a different set of parameters ($h = 0.015$ m, $A = 0.18$ m, $N = 12$ and $L = 0$ m). These parameters allows to generate a sloshing wave impact on the cylinder sitting 0.7 m from the right boundary. The

resulting domain is presented in Figure 5.2 (a) for the case with $D = 0.32$ m, D being the diameter of the cylinder. The lateral boundaries are set to a wall condition (i.e., no slip) and the upper boundary is still open. The setup allows to ensure that the impact on the cylinder is not influenced by reflection on the other boundaries.

An impact on a flat wall was also simulated with an the exact same forcing to provide a reference for later comparisons. In both cases, identical free surfaces are obtained just before impact, the difference starting as soon as the obstacle is reached. The numerical domain for this case is a $0.1 \times 0.7 \times 0.2$ m^3 box with $1 \times 200 \times 80$ cells with 50% of the y-direction containing 80% of the cells while the remaining part has an expansion ratio of 2. This setup allows to match the resolution of the refined mesh on the cylinder. The resolution on the boundary is indeed critical for the pressure distribution. As output, pressure is recorded for all computed time steps at 40 virtual pressure gauges in x=0 and y=0.7 and every 0.5 cm in the vertical direction.

It may be interesting to determine the location of the maximal pressure on the cylinder in function of the shape of the wave when impacting first the obstacle. For that, a supplementary simulation was conducted trying to generate a more critical impact at the first impacted line. To that purpose, the initial free surface defined by equation 5.9, was translated from $L = 0$ m to $L = 0.024$ m which allows to create a more violent case for $D = 0.32$ m.

5.2.4 Comparison with theoretical formula

A comparison of the simulated inline force at impact with the results of the theoretical formula is then proposed for different cylinder radius. In that comparison, the determination of $\lambda\eta_b$ and V, required in Goda's formula, appears crucial. Sawaragi and Nochino [1984] define $\lambda\eta_b$ as follows : *"The height of the vertical wave front is expressed by $\lambda\eta_b$ where η_b is the crest height above the mean water level. The parameter λ is called the curling factor of breaking waves.* In Wienke and Oumeraci [2005] *"The height $\lambda\eta_b$ is interpreted as the height of the impact area"* as shown on Figure 5.3.

In our case the determination of both $\lambda\eta_b$ and V is not straightforward. These values were determined based on two snapshots respectively 10 ms and 20 ms before the impact maximal pressure. At those instants, the wave through has already started to rise up the wall but the crest has not reached the wall. These two snapshots are assumed to properly represent the situation depicted in Figure 5.3. In figure 5.4, we propose four snapshots of the water/air interface before and during impact. The crest of the wave is not as easily identifiable as in Figure 5.3. Based on snapshots at time (a) and (b) of Figure 5.4, the height of the wave front is visually estimated (Figure 5.5). Nevertheless, here, due to artificial mechanism used to produce the wave, non negligible uncertainties arise for the value of $\lambda\eta_b$. Inaccuracies in the determination of the inflexion point on the top part of the wave and of the through level result in the uncertainty illustrated in Figure 5.5. Finally, note that V, also required in the formula, is taken as the velocity of the wave front just before impact.

For comparison with the formula, the computed force on the initial impacted line is obtained by integration of the pressure profile along the same line at each instant. Additionally, the lateral surface flow rate is obtained by integrating the flow lateral velocities over this line. Finally, the time integration of the surface flow rate and inline force over the duration of the impact give the total laterally expulsed water volume and force impulse, respectively.

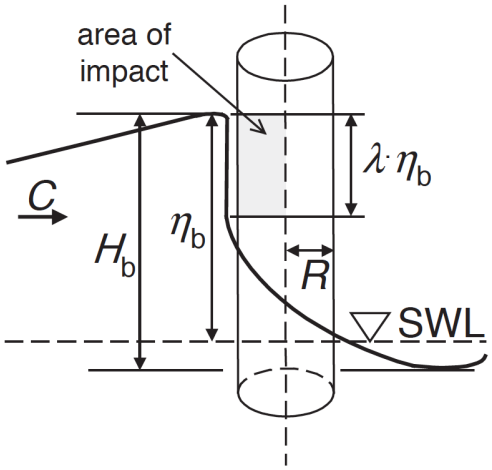

Fig. 3. Definition sketch.

Figure 5.3: Sketch of a wave impact on a cylinder as shown in figure 3 of Wienke and Oumeraci [2005]

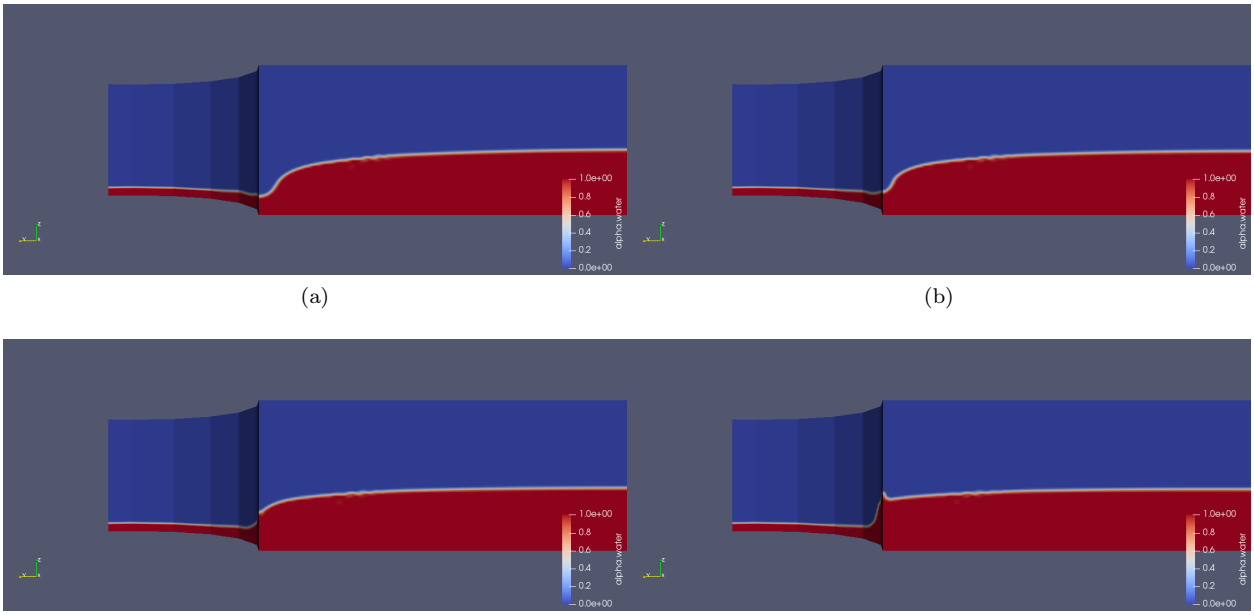

(a) (b)

(c) (d)

Figure 5.4: Snapshot at time (a) = 0.36s, (b) = 0.37s, (c) = 0.38s, (d) = 0.39s

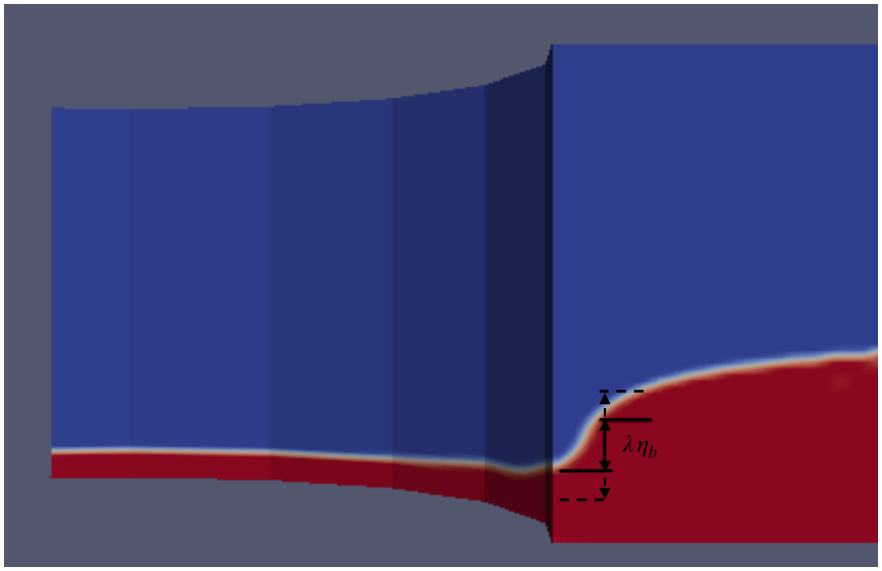

Figure 5.5: Visual estimation the impacting height at $t = 0.37$ s. Equivalent to figure 5.4 (b)

5.3 Results

5.3.1 Model validation in 2D

The pressure distribution at the left wall from 0.97s to 0.99s is presented for both the potential flow model of Scolan [2010] and the present InterFoam simulation in figure 5.6. The difference between the two is also presented on the right panel. Overall, the global distribution is similar but the pressure peak happens later and upward for the potential flow model.

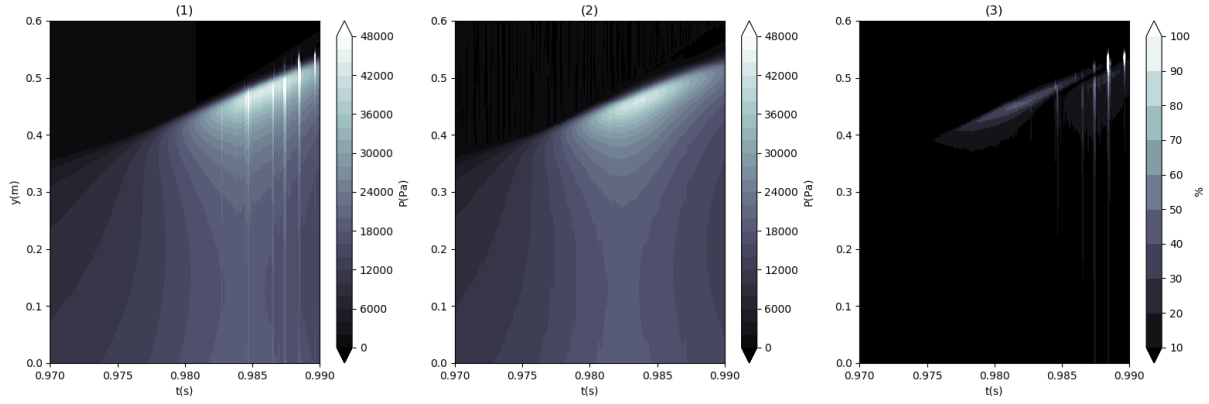

Figure 5.6: Distribution of pressure on the left wall of the domain from 0.97s to 0.99s (1) Potential flow (2) InterFoam (3) difference between the two

A detailed comparison of the interfaces at $t = 0.971$ s , $t = 0.976$ s, $t = 0.981$ s and $t = 0.986$ s is presented in figure 5.7. It should be noted that the vacuum of the potential model is approximated by a

very low density $\rho_{air} = 10^{-6}\ Kg/m^3$ in interFoam. A slight difference of a few centimetres is observed at each time plotted, the VOF model consistently in advance compared to the BEM simulation. Given the very high speeds generally observed in a flip-through impact, the ability of the model to compute accurately the interface can nevertheless be judgeg as acceptable.

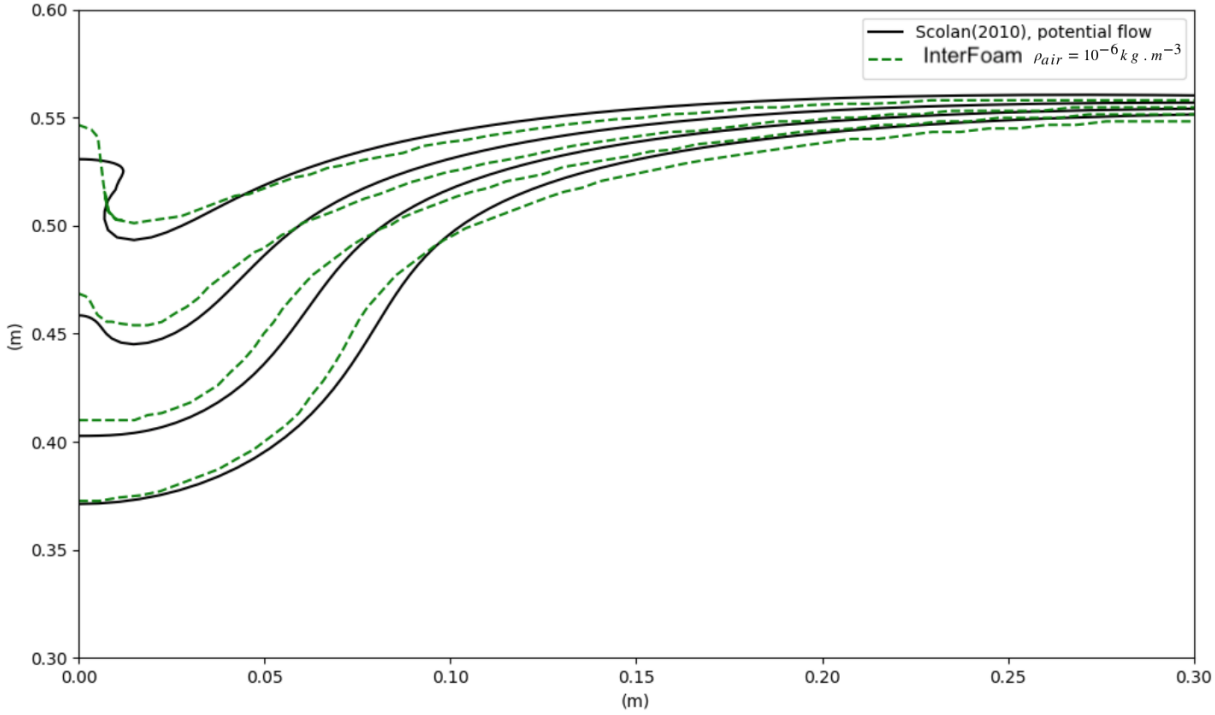

Figure 5.7: Comparison of free surfaces obtained with the two models along the wall at t = 0.971s , t = 0.976s, t= 0.981s, t = 0.986s

A comparison of the pressure distribution along the wall is presented in figure 5.8 at four instants around the maximal pressure. At $t = 0.981$s, the potential flow model presents weaker pressure compared to the VOF model and reaches higher pressure at $t = 0.986$ s. In the VOF model, the maximal pressure is reached between these two instants. The delay between the two peaks is of 3 ms and the discrepancy in their locations is 2 cm.

Hence, as in Martin-Medina et al. [2018], differences between the two models exist, but the main physical aspects of the flip-through are nevertheless retrieved with the VOF model used for this study and its performances are judged acceptable for the study conducted in the present work.

5.3.2 Characteristics of wave impacts on cylinders

The unfolding of the impact on a cylinder is briefly presented in Figure 5.9 or 5.10. It presents the interface before and during the impact at three different stages.

In this numerical experiment, the initial free surface is set so that the impulsive part of the impact pressure reaches up to more than 2 times the quasi static value. With the method explained in Figure 5.3, the impacting wave height, requested in equation (5.2), is estimated as $\lambda\eta_b/D = 0.125$ with an uncertainty

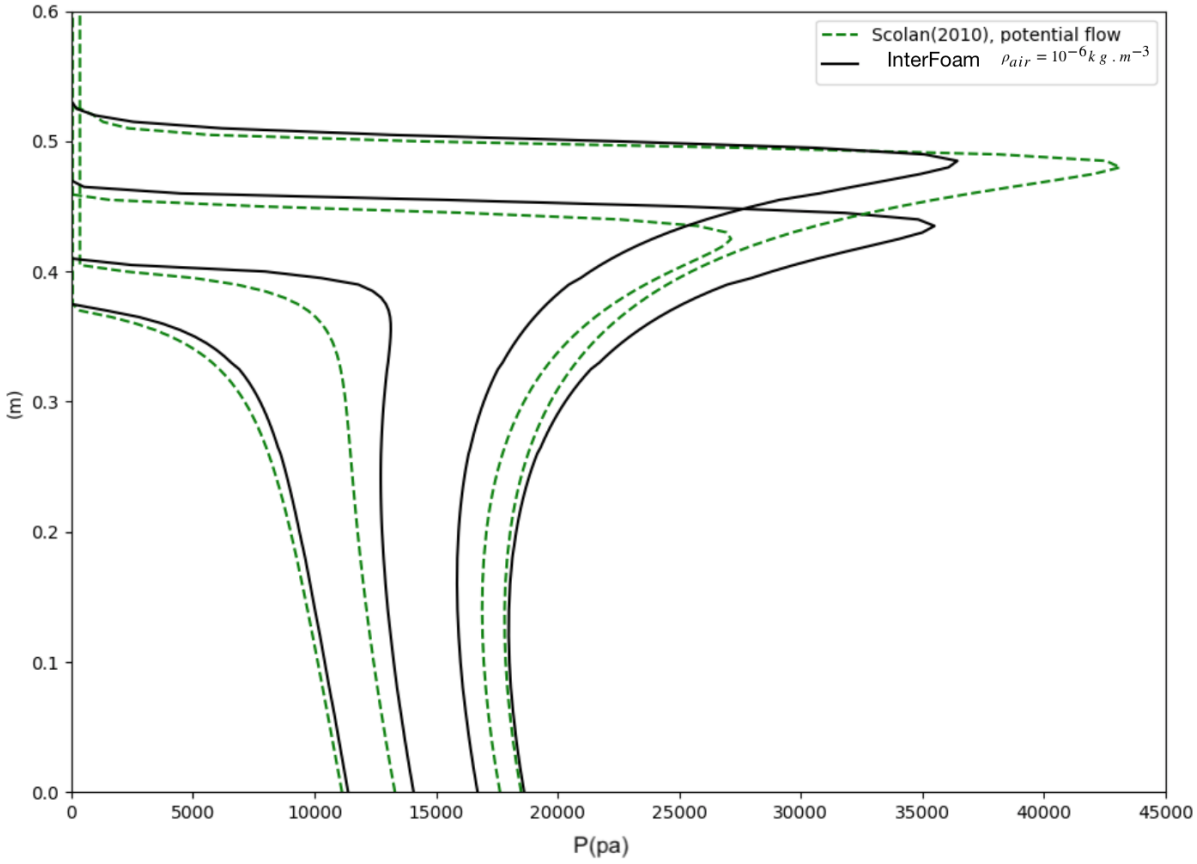

Figure 5.8: Comparison of pressure distributions obtained with the two models along the wall at t = 0.971 , t = 0.976, t= 0.981, t = 0.986

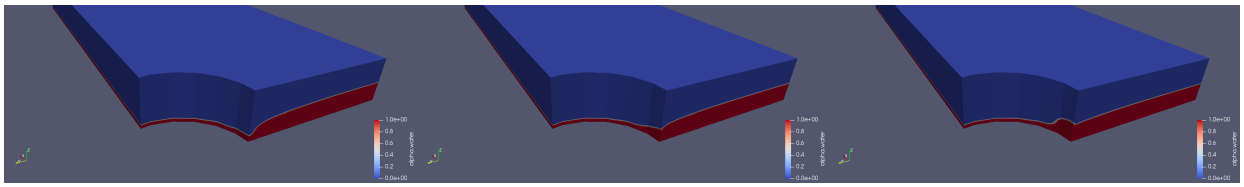

(a) (b) (c)

Figure 5.9: Snapshots of the 3D simulated wave impact on a cylinder, case $L = 0$ - Perspective view.

$0.094 \leq \lambda\eta_b/D \leq 0.156$. The celerity of the wave front is then estimated as $V = 0.8\ m/s^{-1}$ with an uncertainty : $0.6m.s^{-1} \leq V \leq 1m.s^{-1}$. This celerity is taken as reference velocity V_0 to further adimensionalize the results. We also define the reference time as $t_0 = \frac{\lambda\eta_b}{V_0}$.

The non dimensionalized pressure on the flat wall, presented in Figure 5.11, exhibits a maximum non-dimensionalized peak pressure of more than 4.7 while the maximal value recorded on the curved wall is about 3.6. The pressure peak locations on the wall is approximately the same (difference of less than 0.25). Overall, the signals looks similar but with lower values for the cylindrical case.

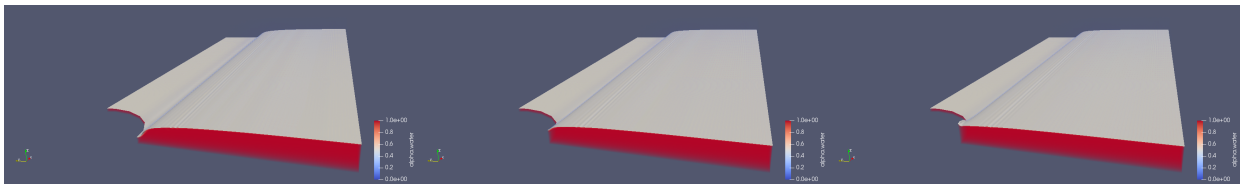

(a) (b) (c)

Figure 5.10: Snapshots of the 3D simulated wave impact on a cylinder, case $L = 0$ - Lateral view.

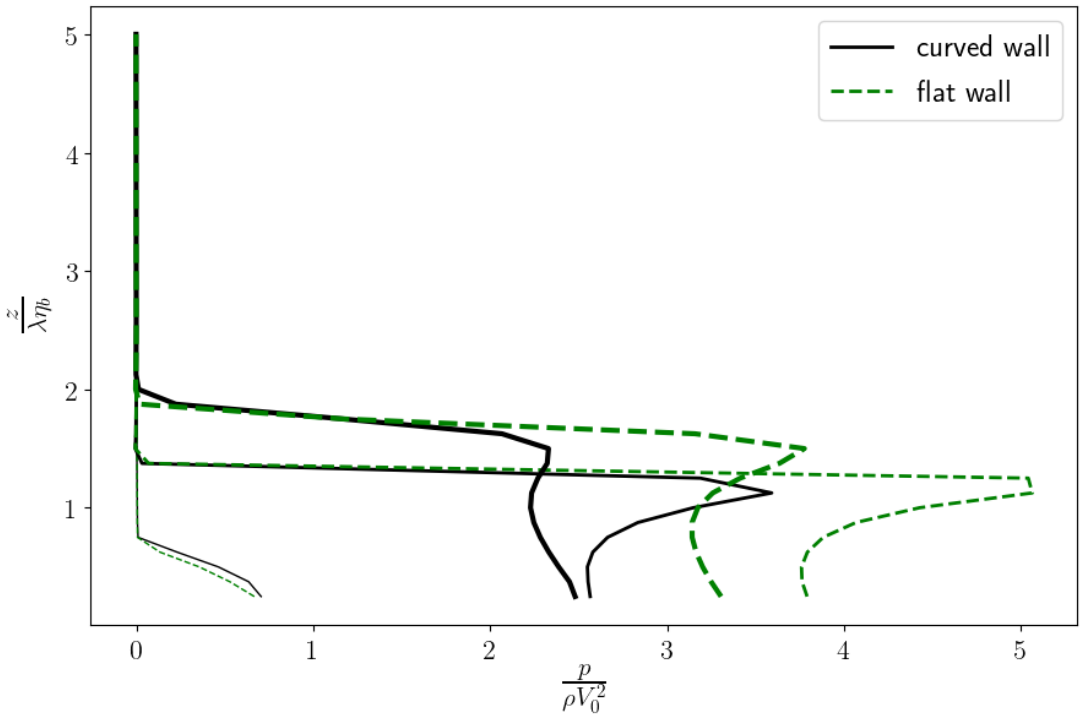

Figure 5.11: Comparison of the pressure distribution along the vertical at $t/t_0 = 7.18$, 7.76, and at the time of maximal pressure in the flat case (7.6) respectively 7.52 in the cylindrical case, the thicker line correspond to later stages of the impact

The same conclusion also holds in time (Figure 5.12). The peak pressure and the quasi static part are indeed weaker for the impact on the cylindrical surface at each vertical locations investigated along the wall. The maximal pressure is recorded around $\frac{z}{\lambda\eta_b} = 1.125$ for the curved case. At this position, the delay between the maximal pressures obtained in the two cases is of 3 ms. The ratio of maximal pressure reached in the cylinder case to the one of the flat case is between 0.68 and 0.86. Note that similar ratio are obtained for the second peak which appears in the quasi-static region.

As already mentioned, the impact considered here presents a ratio between the impulsive and quasi-static part around 2 on the initial impacting line in the cylindrical case. This is far from the highest value expected in the case of a flip-through impact Lugni et al. [2006]. By shifting the initial free surface defined by equation

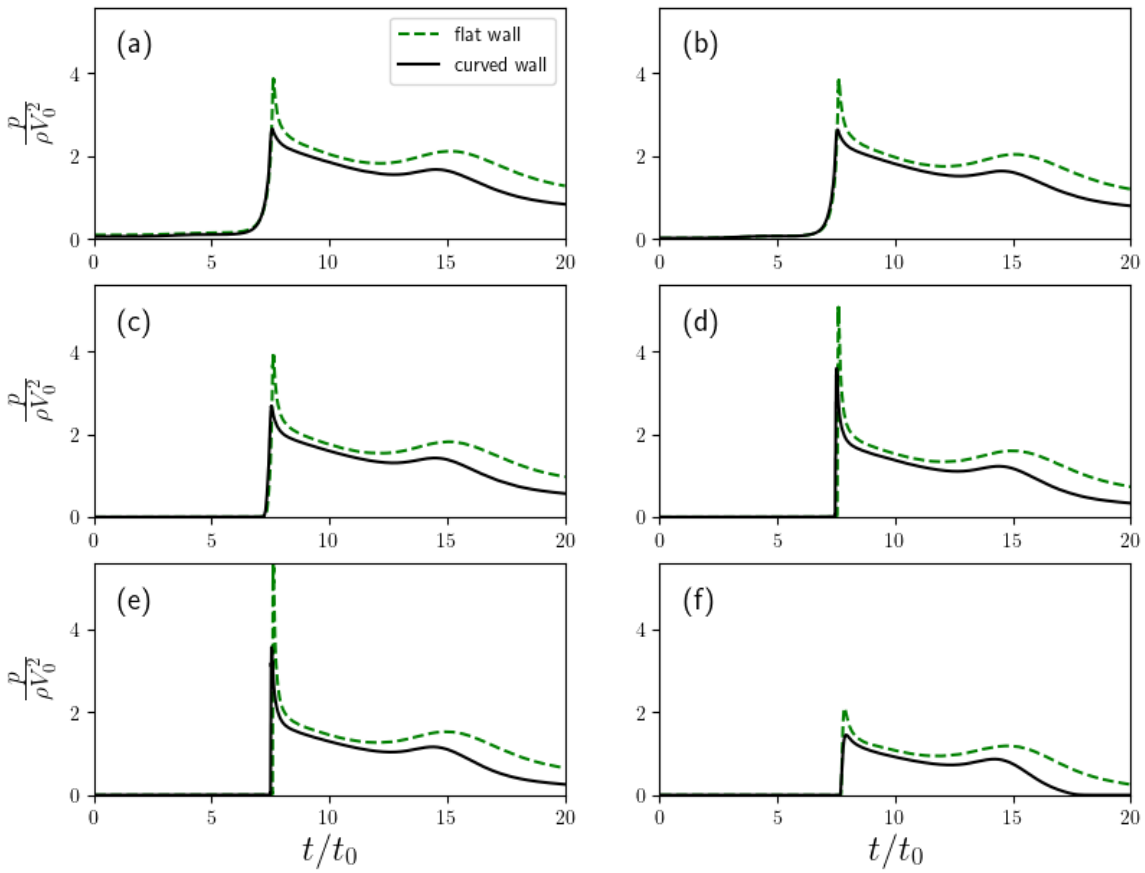

Figure 5.12: Pressure signal in the flat and curved case at $\frac{z}{\lambda \eta_b}$ = (a)0.25, (b)0.375, (c)0.75, (d)1.125, (e)1.25 and (f)1.875.

5.9 from $L = 0$ m to $L = 0.024$ m, a more violent impact impact is obtained (Figure 5.13). In this case the impulsive to quasi static pressure ratio is more than 3 on the initial impact line. It is likely that even higher pressures may be reached by slightly increasing the value of L. Nevertheless, with the resolution used here, this impact is one of the most violent obtained without air entrapped.

We try now to determine whether higher pressures can be found further along the cylinder face. Indeed, as our impact is not the perfect flip-through, there is necessarily a point on the cylinder that is at the distance where an ideal flip-through would occur on a flat wall. We make therefore the hypothesis that around this part, the flow condition may approach the case of the flip-through and generate higher pressures than during the initial impact (i.e. in the middle line).

On figure 5.14, the maximal value of the pressure in time is presented in function of the distance to the initial impact line along the x axis. As assumed in the former paragraph, in both cases, higher pressure values are obtained further along the cylinder face. Note that the increase is noticeably more significant in the case initially closer to the flip-through.

The impact closer to the flip-through naturally happens later than the other as the initial free surface has been shifted away from the cylinder (figure 5.15). We also note that the pressure peaks appears quickly

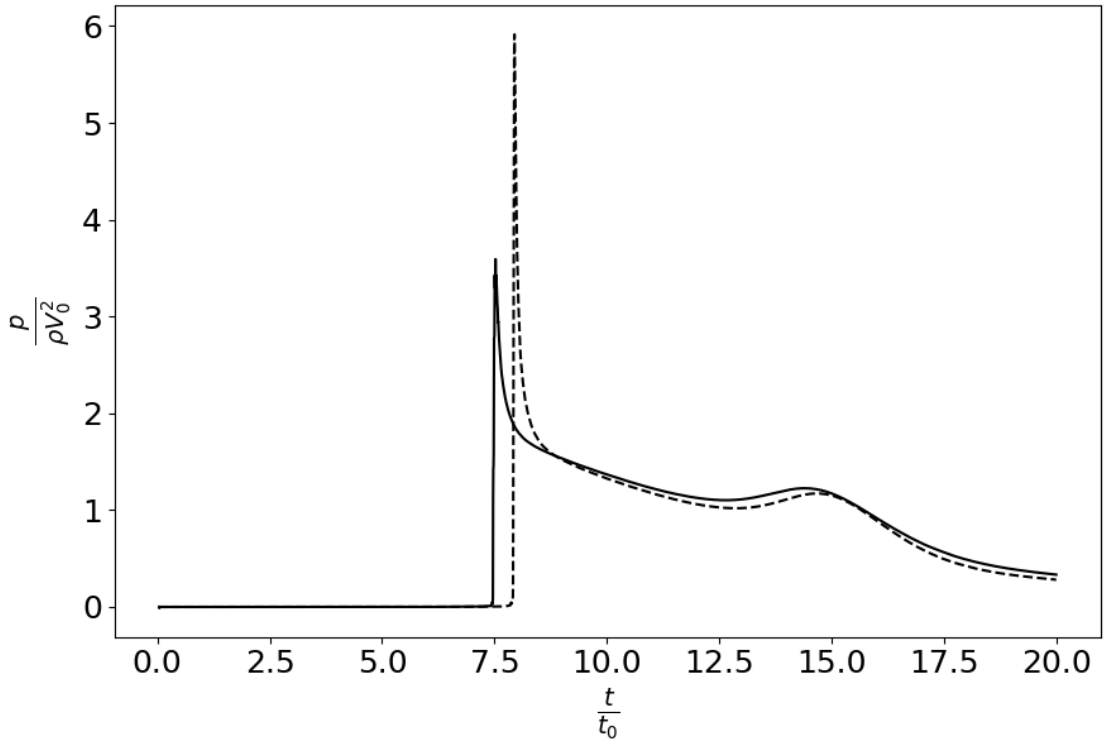

Figure 5.13: Normalised pressure time series at $z = 0.045$ m on the middle line of the cylinder for two different initial configurations : plain line $L = 0$ m and dashed line $L = 0.024$ m in equation (5.9).

at the second line after the first maximum obtained in the middle line. The process takes longer times for the 2 other vertical lines considered although they are closer to the second line than the second line was to the first. This indicates a faster dynamic of the impact in the middle zone of the cylinder likely related to the weak value of the angle formed between the water jet and the attacked surface in plane view.

Hence, in both cases presented here, the highest pressures obtained in the case of impact on a cylinder of relative large radius are not on the first impacted line. To the best of our knowledge this result is original and has not been shown previously. This is probably due to the smaller values for the cylinder radius usually considered in the wave impact studies. According to the geometrical features considered, the pressure is most of the time only investigated along the first impacted line.

Nevertheless, we note that the highest pressures observed on the cylinder remain lower compared to the related values appearing in the impact on a plane wall. For instance, we recorded a maximum absolute pressure of 3.6 on the cylinder for $L = 0$ while the corresponding value is 5.76 in the related 2D case, so a ratio of about 1.60. For $L = 0.024$m, the ratio is 2.2 (i.e., 6.1 Pa versus 13.7 Pa).

5.3.3 Influence of the cylinder radius

In this section, the influence of the cylinder radius on the maximal pressure obtained on the vertical middle line of the cylinder is studied using as initial condition, the free surface defined by equation 5.9 with $L = 0$

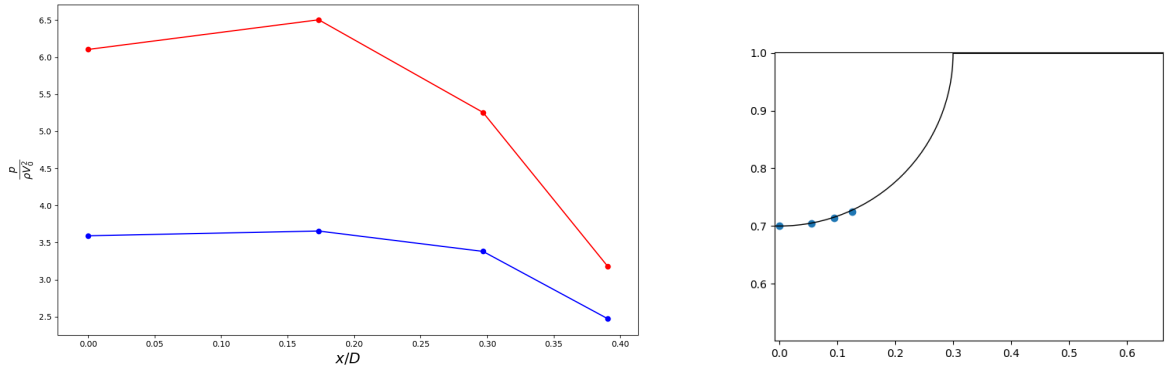

(a) (b)

Figure 5.14: (a)Relative maximal pressure on four different vertical lines located along the cylindrical obstacle in function of x/D. In red, the case $L = 0.024$ m and in blue, the case $L = 0$ m as defined in equation 5.9. (b) position of each vertical line on the cylinder in plane view.

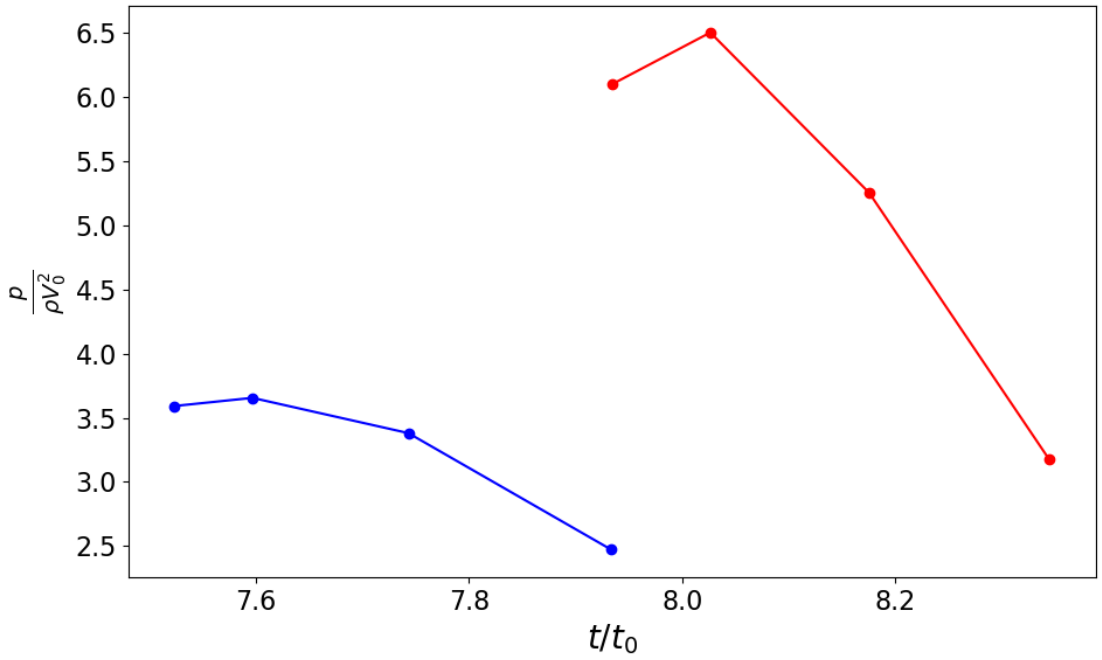

Figure 5.15: Relative maximal pressure on different vertical lines located along the cylindrical obstacle in function of t/t_0. In red, the case $L = 0.024$ m and in blue, the case $L = 0$ m as defined in equation 5.9.

m. Although it was shown previously that the maximal pressure is not obtained at the middle line of the cylinder, the symmetry vertical line is still the reference in the literature and is therefore conserved in this section.

The maximal pressure observed on the initial impacted line (i.e., the middle line) of the cylinder, for

different radius, is presented figure 5.16. Overall, despite two obvious outliers, the trend is an increase of the maximal pressure with the cylinder radius followed by an seemingly asymptotic value of about 3.6 in this case for non-dimensional radius up to 10-15. The two former points excepted, a law of the form $\frac{P_{max}}{\rho V_0^2} = a - \frac{b\lambda\eta_b}{D}$ can be fitted and returns a normalised root mean square deviation of less than 2%. The two outliers are maybe due to local problems present in the mesh generated by snappyHexMesh.

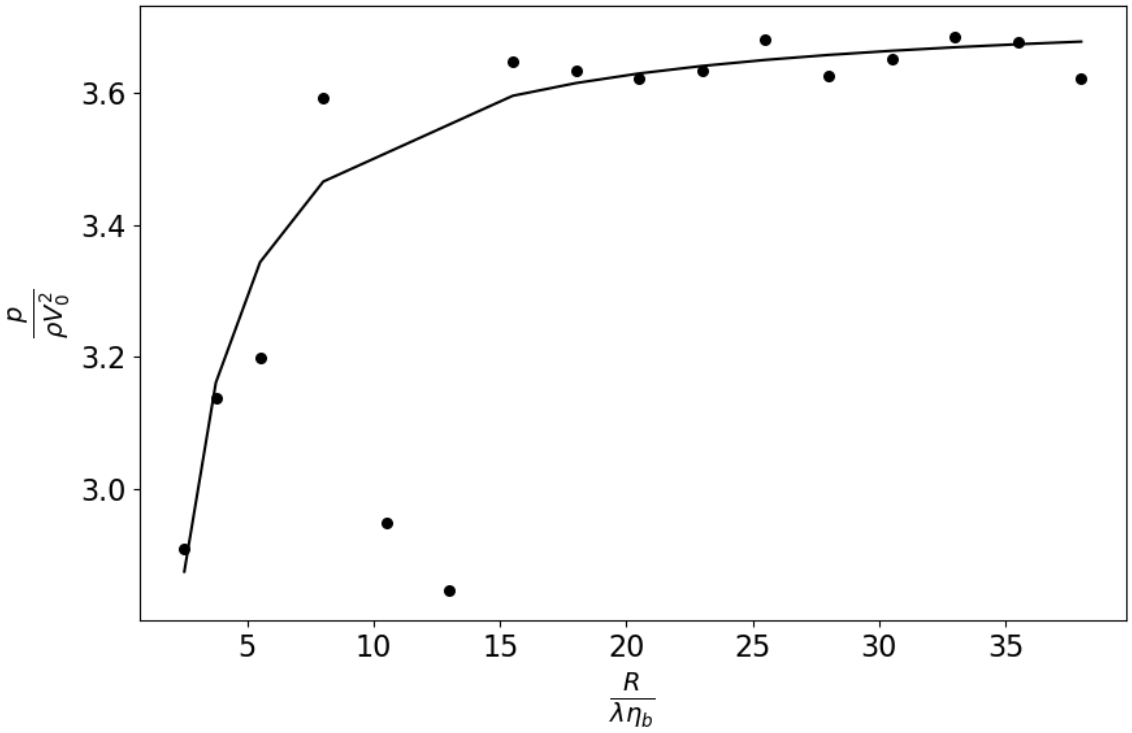

Figure 5.16: Relative maximal pressure computed at the middle line for different cylinder radius.

The force applied to the initial impacted line on the cylinder is also evaluated for different radius figure 5.17. As expected, and as for the pressure, the force increases with the cylinder radius. Nevertheless, in this case, the increase is continuous and no asymptotic value is reached conversely to the maximum pressure.

The instantaneous lateral discharge (in m^2/s) at the time pressure is maximum, is calculated by integrating the lateral velocity (i.e. in the y direction) along the first impacted line (see figure 5.2 for the axis definition). Note that this line is just shifted one cell away to allow for lateral velocities to occur (i.e., one cell away from the stagnation point). Obviously, the force increase is associated to a decrease of the lateral flow discharge at the cylinder. The flow continuity imposes that the decrease of the lateral discharge is compensated by an increase of the vertical discharge. Therefore, the force on the cylinder is positively correlated with the vertical discharge and negatively correlated with the lateral discharge.

For the non-dimensionalized force, a good fit was obtained with the function $f(x) = a \ln bx + c$ ($a = 0.54$, $b = 1.2$ and $c = 1.6$) with a normalised root mean square deviation (NRMSD) of less than 5%. Whereas the non-dimensionalized lateral linear discharge was best approximated with the law $f(x) = a/x + b$ ($a = 0.01$,

$b = 0.57$) with a normalised root mean square deviation of 24%.

The former variables (i.e., force and lateral discharge) are now integrated over the impact duration to determine the so-called force impulse and the total flow (surface) expelled laterally (Figure 5.18). Again, there are a few surprising values ($\frac{D}{\lambda\eta_b} = 8$ and 38 m) which appear, not for the same radius values as previously though. The same type of laws as previously, were fitted with larger normalised RMSD values (i.e., 13% and 42% respectively).

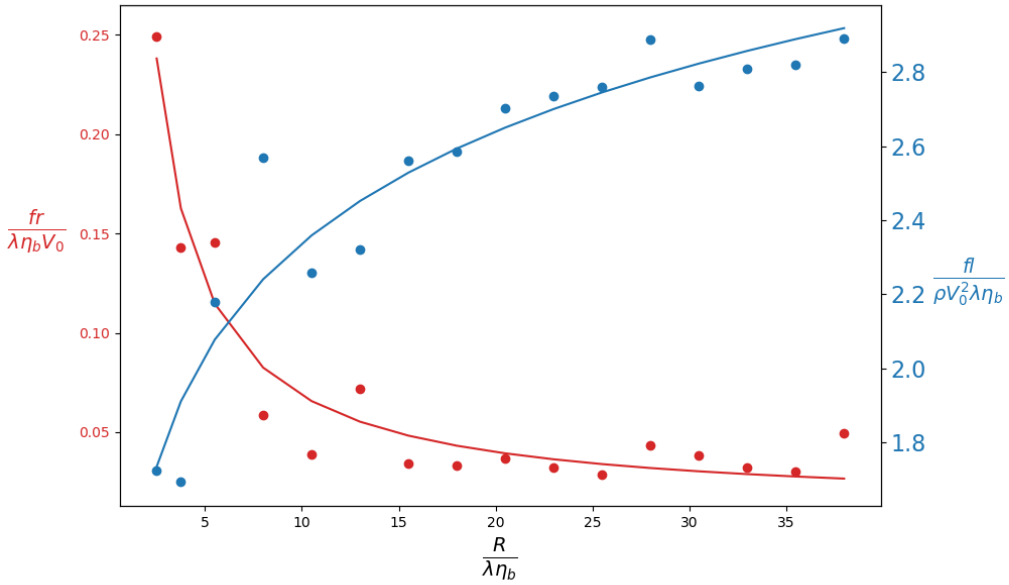

Figure 5.17: Non-dimensional force (blue) and lateral discharge (red) at the instant of maximal pressure on the initial impact line in function of the cylinder non-dimensional radius

As mentioned in Wienke and Oumeraci [2005], only the maximum force on the middle line at the beginning of the impact can be calculated with the theories described in Wagner [1932] or Von Karman [1929]. In our simulations, the NRMSD obtained for this parameter is quite low showing a regularity in the simulations.

In figure 5.19, we compare our numerical results with the values obtained when applying Goda's formula [Goda et al., 1966] with the wave characteristics simulated. Taking into account the uncertainty associated to the determination of $\lambda\eta_b$ and V_0 gives birth to the shaded area shown in the figure, representing all the possible values predicted by the formula. We first remark that this uncertainty results in a very large range of possible values, especially for large relative radius. Despite this, a clear discrepancy between the simulations and the predictions with the formula appears. For relative short radius, the formula underestimates the results of the numerical simulation while for larger relative radius, the range of the predicted values is very wide and even reaches values corresponding to the flat case considered as the upper limit. The results of the simulations seem to show that the force on the initial impacted line do not follow a linear trend with respect to the cylinder radius conversely of what predicts Goda's formula.

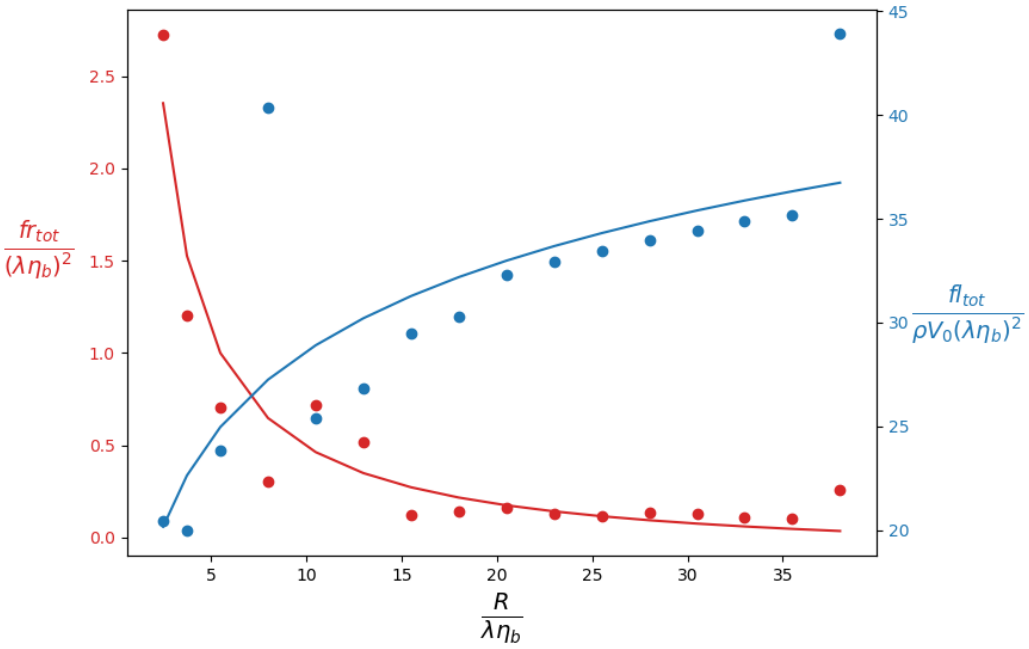

Figure 5.18: Non-dimensional force impulse (blue) and overall flow expelled laterally (red) in function of the cylinder non-dimensional radius

5.4 Discussion

In the present study, the interFoam solver of the openFoam code has been used to simulate wave impact on cylinders and on a planar surface. The underlying aim of the chapter was to evaluate the importance of wall curvature in the impact process in order to draw conclusions for coastal breakwater round heads. The model has been initially validated by comparison with results of a potential flow model in a case close to a flip-through impact [Scolan, 2010]. Several impacts on cylinder of varying radius have been simulated. The two wave cases simulated involved waves just about to break when first meeting the obstacle (one being closer to the flip-through than the other).

The 3D simulations shows significant differences in the pressure profile along the front line between the 2D and the cylindrical cases. These differences can be explained by the generation of lateral velocities allowed by the wall curvature, which, through momentum conservation, induce a decrease of the pressure peak.

In the simulations involving a cylinder, the largest pressure are found away from the front line especially for the most violent impact (i.e. the closest possible to the flip-through). It can be inferred that some kind of focusing occurs away from the front line when the hypothetical breaking point is located after the front line. In the 2D flip-through case, high pressures are generated at the focusing point where the fast up rising trough meets the incoming wave crest. In the cylindrical case, the same phenomenon still exists but associated with a lateral movement around the cylinder generated at earlier stages of the impact close to the cylinder front line. The question now remains whether the pressures generated by this process are or not larger than the ones generated with a perfect flip through on the front line. This problem will be studied in

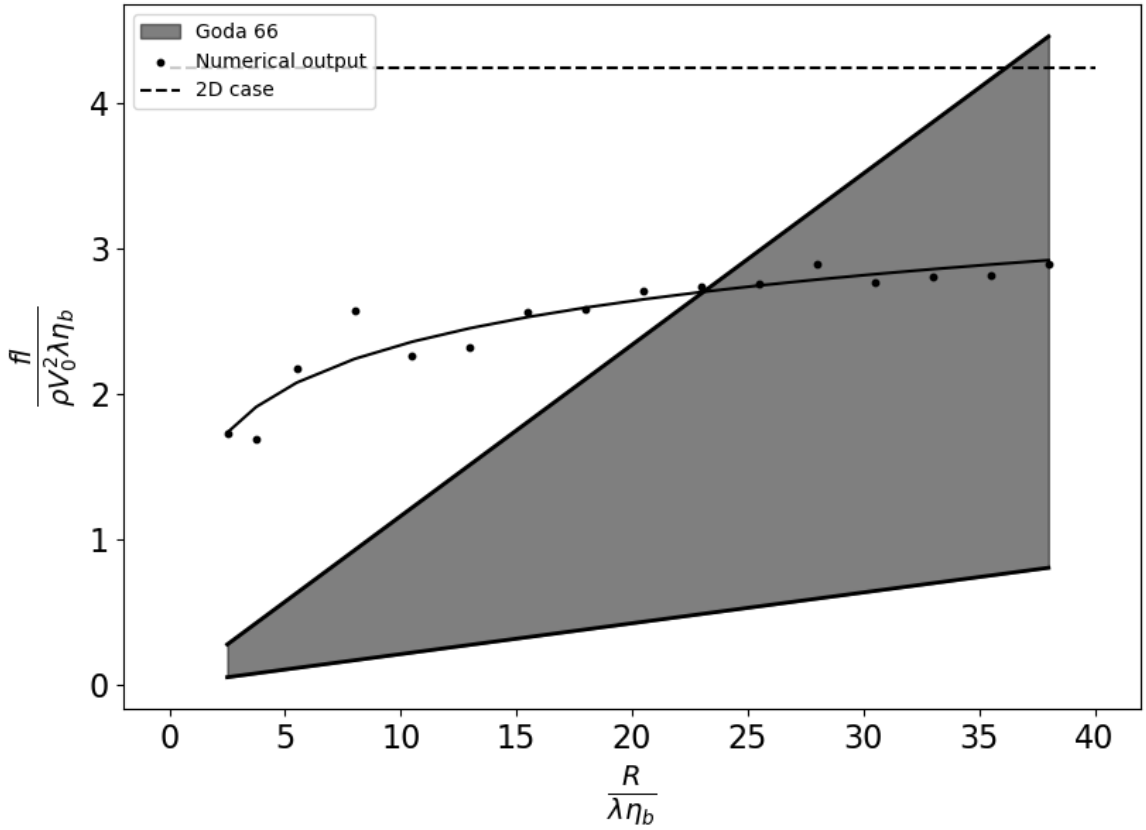

Figure 5.19: Computed non-dimensional maximum force on the first impacted line (dots) and fitted function (plain black line) versus non-dimensional radius. The shaded area represents the range of possible values when applying the Goda's formula [Goda et al., 1966] to the numerical simulations taking into account uncertainty in the determination of $\lambda\eta_b$ and V_0.

the next coming weeks. A denser array of virtual probes may be useful for this future work.

Event with this focusing effect, the maximum pressure do not reach values as high as the corresponding 2D case. This results is logical as there is always a lateral flow, which induces a pressure diminution compared to the 2D case, in which the flow can only escape upward. Therefore, the 2D impact should always be considered as the one generating the largest pressure peak even compared with an ideally placed cylinder submitted to a flip-through on the front line.

The theoretical formula of Goda et al. [1966] is still used today for engineering purpose and shows generally good agreement with measurements (e.g., Hallowell et al. [2016] for instance). It was therefore of interest to compare the present results obtained with 3D CFD simulations when varying the cylinder radius with prediction of this formula. Our simulations show a dependency of the maximum force with the radius of the form $f(x) = a \ln bx + c$ (with a normalised RMSD of less than 5%).

The slamming coefficient used in Goda et al. [1966] is π. With this value, the formula clearly underestimates the simulations results. With a factor 2π in agreement with Wagner [1932] theory and Wienke and Oumeraci [2005], the agreement may be better but a definitive conclusions is befficiult to draw according

the uncertainty range appearing for large relative radius. Goda's formula is linear with respect to the radius while the numerical simulations carried out in this study seem to imply a non linear evolution especially in the low relative radius range.

This study has shown the spatial variability of pressure during wave impact on cylinder and in particular that the initial impacting line is not necessarily the place where the maximal pressure is observed. While the in-situ pressure measurements on the wall of the Artha breakwater present numerous limits, an overall augmentation of pressure away from the axis of the main swell direction is sometimes observed. A 3D simulation of a very well documented impact in this real case could help determine whether the two results are due to the same phenomenon.

As formerly pointed out, one of the limitation of this study may be the mesh grid variability especially close to the cylinder front line. The snappyHexmesh process refines the grid around the cylinder so that it is not possible to have the exact same grid for all the cases. This problem may explain a seemingly erratic values obtained for a few specific radius. The numerical domain should also be extended along the y-axis to avoid the effect of reflection on the wall in later stages of the impact and therefore allow a longer time of simulation.

Finally, in this chapter, comparisons have been made with a widely used formula [Goda et al., 1966]. More recent theories considering the whole duration of the impact have also been established [Wienke and Oumeraci, 2005, Ghadirian and Bredmose, 2019] and could also be compared to the present simulations.

5.5 Conclusions

A comparative study of wave impact on a flat wall and on different cylinders have been conducted and showed a significant effect of the cylinder radius. As expected, the pressure values are, overall, weaker on the cylinder compared to the flat wall case. The maximum force acting on the cylinder front line was compared to the prediction obtained with Goda's formula [Goda et al., 1966]. This comparison apparently showed an underestimation by the latter but this conclusion is not certain according to the uncertainty obtained when applying the formula. For the case studied in this chapter, involving a violent sloshing impact, we observed that the highest pressure is not obtained on the cylinder front line. Quite high relative pressures were obtained and should be compared with an ideal flip-through case relatively to the front line.

Conclusion

5.6 Synthesis of the scientific approach

The aim of this thesis was to provide original results on wave propagation and impact on a composite breakwater and by extension, provide a better understanding of similar environments characterised by steep slopes, a macro roughness ended by a wall like structure as for instance found in coastal cliffs. For this purpose, field measurements were conducted and provide a unique dataset. The thesis is structured as a funnel starting from meso-scale to finally addressing micro-scale processes.

chapter 3 proposes an analysis of the high frequency wave impact pressures measurement carried out on the vertical wall of the Artha breakwater. The statistics and characteristics of the measured pressures were presented. A statistical analysis of the influence of environmental variables on the maximal pressure is then conducted. The explanatory variables, namely, the local wind, the water-level and the wave parameters are the results of large scale phenomena. The statistical models developed therefore offers an insight on how the meteorological systems and tides result in solicitations on a coastal structure. It is the first study of its kind to the best of our knowledge. But this statistical model is blind to the wave transformation processes between the offshore wave buoy and the vertical wall of the breakwater.

The aim of chapter 4 was therefore to fill this gap. The composition of the wave field in this area was investigated thanks to measurements in the block armour complemented with numerical simulations using the model SWASH. Based on the measurements and the model results, it was possible to determine the maximal wave height at the toe of the structure and the extent of the surf zone for different conditions of waves and water levels. The knowledge of the maximal wave height allows to perform a comparison between the prediction of the classical Goda's formula and the prediction of the statistical model of chapter 3. While chapter 4 also provides interesting information on the wave field in the direct vicinity of the structure, a share of the variability is still due to processes at the scale of a single wave impact on the vertical wall.

As the high frequency pressure measurements are conducted on the Artha breakwater western roundhead, it was necessary to evaluate the influence of the wall curvature on wave impact pressure. To address this question, chapter 5 presented a numerical study of wave impact on cylinders of varying radius. This study is conducted with a 3D full Navier-Stokes VOF models, its originality being the large relative value of cylinder radius considered.

5.7 Main results

The measurements on the wall of the Artha breakwater have provided an unmatched number of real wave impacts. More than 50% of the maximal pressure variability is explained by the multivariable statistical model. As expected wave height has a dominant influence on wave impact maximal pressure in this model. The other wave parameters, water level and wind speed also have a significant influence while wind direction is not significant. Outliers have also been observed. The study of the pressure signal of the corresponding impacts showed distinctive properties. While the vast majority of impacts present the characteristics of broken wave impacts, the outliers show the very particular and well recognisable topology of highly aerated impacts. This result proves that various modes of functioning coexist at this breakwater.

Pressure measurements in the breakwater armour provided original data on wave transformation in a steep chaotic bathymetry. Unfortunately, a simple transfer function linking the offshore wave height to the one at the toe of the breakwater could not be determined which makes the interpretation of the results more difficult. The main results of this study were therefore obtained on processes occurring in the direct vicinity of the structure. The significant wave heights and reflection coefficients were obtained from measurements and this data was used to validate a 2DV numerical model. After calibration, the numerical model shows acceptable differences with the measurements. The extent of the surfzone for the different scenarios confirms that most of the wave impacts are generated by broken waves which makes our database quite original compared to the existing literature. The maximal wave height at the toe of the breakwater was computed thanks to the model. Based on this information, maximal impact pressures predicted by the Goda formula were compared with the predictions of the statistical model obtained in chapter 3. The predictions of Goda's formula are found to be higher than the measurements statistics, which appears quite coherent according to the purpose of the formula (i.e. breakwater design).

The study of the influence of the wall curvature on wave impact pressure has shown a decrease of peak pressure with radius for non broken wave impacts. For this type of impacts, the maximal pressure is not observed on the initially impacted line but slightly away which is also, to our knowledge, an original result. The maximal pressures computed are nevertheless always lower than what is expected in the case of an ideal flip through on a flat surface.

Overall the results of this thesis seem to show that the failure of the breakwater during an exceptional wave impact is a very unlikely event. In particular the comparison with the Goda formula. On the other hand the various types of wave impact observed and the identification of different functioning modes for the breakwater suggest that some specific wave impact could be the source of the localised, small scale damages regularly observed on site.

5.8 limits and perspectives

Several limitations exist for the statistical model of chapter 3. Due to the limited number and the position of the sensors and also owing to the fact that pressure was only recorded for 10 minutes every hour, the maximal pressure peaks were likely missed. The pressure sensor array is indeed very far from perfect with irregular spacing both vertically (especially the gap between the lower sensor and the others) and alongshore. This placement was unfortunately imposed by the breakwater stakeholders who feared the

creation of weakness points on the exposed face which could constitute a potential source of severe and expensive damage. Therefore, the maximal pressure measured during each burst is almost certainly always not the highest pressure striking the western roundhead during this period. Nevertheless it was the best parameter at our disposal to grasp the range of pressure expected on this structure. Even though, the number of impacts and the variety of conditions in which those impacts were measured make it a very interesting database. This original and significant database will be the ground for more complete and detailed statistical analysis than the one presented in the first chapter of this thesis. Regarding the variety of pressure signals observed, a classification of impact type would be necessary and could for instance be used as a discrete variable in a future statistical model. It would also be interesting to test the capacity of machine learning algorithms to compute the maximal pressure for a given set of environmental variables.

Regarding the measurements of chapter 4, it would be interesting to have data over wider range of conditions. Nevertheless as shown by the loss of the sensor the closest to the wall, performing measurements in such environment is not without risk for the instrumentation. Overall, a better knowledge of the transfer function from the offshore buoy to the toe of the breakwater is necessary. A 3D model of the area could help answering this question.

The main limits of chapter 5 is the impacting wave phase which we did not variate extensively. A sensitivity analysis of the position of maximal pressure on the cylinder while varying this parameter will bring valuable knowledge on the mechanics of flip-through impacts on cylinders.

Overall with the combined knowledge of the three chapters, several operational tools are foreseeable. A more complete statistical model including wave impact type and the level of wave breaking in the block armour could provide real time alert to predict extreme wave impact pressures at the breakwater. For some specific cases, reproducing single wave impact with a 3D full Navier-Stokes model validated on the pressure measurement would allow to perform a very accurate evaluation of the structural stability for those specific impacts.

Bibliography

Hirotogu Akaike. Information theory and an extension of the maximum likelihood principle. In *Selected papers of hirotugu akaike*, pages 199–213. Springer, 1998.

R. A. Bagnold. Interim report on wave-pressure research. *Excerpt from the J. of the Institution of Civil Engineers*, 1939. URL `http://resolver.tudelft.nl/uuid:fba1d7fe-13f9-4496-be07-873d7faa607b`.

PAD Bird, AR Crawford, PJ Hewson, and GN Bullock. An instrument for field measurement of wave impact pressures and seawater aeration. *Coastal engineering*, 35(1-2):103–122, 1998.

P. A. Blackmore and P. J. Hewson. Experiments on full-scale wave impact pressures. *Coastal Engineering*, 8(4):331–346, 1984.

H. Bogaert, S. Léonard, L. Brosset, and M.L. Kaminsk. Sloshing And Scaling: Results From the Sloshel Project. All Days, 06 2010. ISOPE-I-10-030.

Jean Bougis, Didier Rihouey, Sébastien Bernard, Charlie Vergnet, Cyrielle Cayrol, Nicolas Garcia, Frédéric Jocou, and Alain Roudil. Extrapolation d'essais d'impacts de la houle sur modèles réduits. pages 333–342. Editions Paralia, 2016. ISBN 978-2-35921-017-0. doi: 10.5150/jngcgc.2016.038. URL `http://www.paralia.fr/jngcgc/14_38_bougis.pdf`.

H. Bredmose, D. H. Peregrine, and G. N. Bullock. Violent breaking wave impacts. Part 2: modelling the effect of air. *Journal of Fluid Mechanics*, 641:389, December 2009. ISSN 0022-1120, 1469-7645. doi: 10.1017/S0022112009991571. URL `http://www.journals.cambridge.org/abstract_S0022112009991571`.

H. Bredmose, G. N. Bullock, and A. J. Hogg. Violent breaking wave impacts. Part 3. Effects of scale and aeration. *Journal of Fluid Mechanics*, 765:82–113, February 2015. ISSN 0022-1120, 1469-7645. doi: 10.1017/jfm.2014.692. URL `http://www.journals.cambridge.org/abstract_S0022112014006922`.

L. Brosset, M. Marhem, W. Lafeber, H. Bogaert, P. Carden, and J. Maguire. A Mark III Panel Subjected to a Flip-through Wave Impact: Results From the Sloshel Project. All Days, 06 2011. ISOPE-I-11-029.

SA Brown, DM Greaves, V Magar, and DC Conley. Evaluation of turbulence closure models under spilling and plunging breakers in the surf zone. *Coastal Engineering*, 114:177–193, 2016.

G. Bullock, C. Obhrai, G. Muller, G. Wolters, H. Peregrine, and H. Bredmose. Characteristics and design implication of breaking wave impacts. In *Coastal Engineering 2004*, pages 3966–3978, National Civil Engineering Laboratory, Lisbon, Portugal, April 2005. World Scientific Publishing Com-

pany. ISBN 978-981-256-298-2 978-981-270-191-6. doi: 10.1142/9789812701916_0320. URL http://www.worldscientific.com/doi/abs/10.1142/9789812701916_0320.

G.N Bullock, A.R Crawford, P.J Hewson, M.J.A Walkden, and P.A.D Bird. The influence of air and scale on wave impact pressures. *Coastal Engineering*, 42(4):291–312, April 2001. ISSN 03783839. doi: 10.1016/S0378-3839(00)00065-X. URL http://linkinghub.elsevier.com/retrieve/pii/S037838390000065X.

G.N. Bullock, C. Obhrai, D.H. Peregrine, and H. Bredmose. Violent breaking wave impacts. Part 1: Results from large-scale regular wave tests on vertical and sloping walls. *Coastal Engineering*, 54(8):602–617, August 2007. ISSN 03783839. doi: 10.1016/j.coastaleng.2006.12.002. URL http://linkinghub.elsevier.com/retrieve/pii/S037838390600192X.

Bullock G., Obhrai C., Müller G., Wolters G., Peregrine H., and Bredmose H. Field and Laboratory Measurement of Wave Impacts. *Coastal Structures 2003*, 2004. ISSN 9780784407332. doi: 10.1061/40733(147)29.

Hongjian Cao, Jingjing Zha, Decheng Wan, et al. Numerical simulation of wave run-up around a vertical cylinder. In *The Twenty-first International Offshore and Polar Engineering Conference*. International Society of Offshore and Polar Engineers, 2011.

Ronald T Cenfetelli and Geneviève Bassellier. Interpretation of formative measurement in information systems research. *MIS quarterly*, pages 689–707, 2009.

Raymond Cointe and J-L Armand. Hydrodynamic impact analysis of a cylinder. 1987.

MJ Cooker and DH Peregrine. Violent water motion at breaking-wave impact. In *Coastal Engineering 1990*, pages 164–176. 1991.

Giovanni Cuomo, William Allsop, Tom Bruce, and Jonathan Pearson. Breaking wave loads at vertical seawalls and breakwaters. *Coastal Engineering*, 57(4):424–439, 2010.

D Damico, B Larroque, F Luthon, P.A. Poncet, and S. Abadie. Continuous measurement and automatic processing of in-situ wave impact pressure data. 2020.

Suraj S Deshpande, Lakshman Anumolu, and Mario F Trujillo. Evaluating the performance of the two-phase flow solver interfoam. *Computational science & discovery*, 5(1):014016, 2012.

F. Dias and J.M. Ghidaglia. Slamming: Recent progress in the evaluation of impact pressures. *Annual Review of Fluid Mechanics*, 50(1):243–273, 2018. doi: 10.1146/annurev-fluid-010816-060121. URL https://doi.org/10.1146/annurev-fluid-010816-060121.

Guillaume Dodet, Fabien Leckler, Damien Sous, Fabrice Ardhuin, Jean François Filipot, and Serge Suanez. Wave runup over steep rocky cliffs. *Journal of Geophysical Research: Oceans*, 123(10):7185–7205, 2018.

Andrew G Fabula. Ellipse-fitting approximation of two-dimensional, normal symmetric impact of rigid bodies on water. In *Proceedings of the 5th midwestern conference on fluid mechanics*, pages 299–315, 1957.

Odd Magnus Faltinsen and Alexander N. Timokha. *Sloshing*, volume 577. Cambridge university press Cambridge, 2009.

Joel H Ferziger, Milovan Perić, and Robert L Street. *Computational methods for fluid dynamics*, volume 3. Springer, 2002.

Amin Ghadirian and Henrik Bredmose. Pressure impulse theory for a slamming wave on a vertical circular cylinder. *Journal of Fluid Mechanics*, 867:R1, 2019. doi: 10.1017/jfm.2019.151.

Y. Goda, S. Haranaka, and M. Kitahata. Study on impulsive breaking wave forces on piles. , Ports and harbor research institute, Ministry of transport, Japan, 1966.

Yoshimi Goda. New wave pressure formulae for composite breakwaters. In *Coastal Engineering 1974*, pages 1702–1720. 1975.

Yoshimi Goda. *On the Methodology of Selecting Design Wave Height*, pages 899–913. 1988. doi: 10.1061/9780872626874.068.

Gene H Golub, Michael Heath, and Grace Wahba. Generalized cross-validation as a method for choosing a good ridge parameter. *Technometrics*, 21(2):215–223, 1979.

Ulrike Groemping. Relative importance for linear regression in r: The package relaimpo. *Journal of Statistical Software, Articles*, 17(1):1–27, 2006. ISSN 1548-7660. doi: 10.18637/jss.v017.i01.

RT Guza and Edward B Thornton. Swash oscillations on a natural beach. *Journal of Geophysical Research: Oceans*, 87(C1):483–491, 1982.

Joseph F Hair. Multivariate data analysis: An overview. *International encyclopedia of statistical science*, pages 904–907, 2011.

S. Hallowell, A. T. Myers, and S. R. Arwade. Variability of breaking wave characteristics and impact loads on offshore wind turbines supported by monopiles. *Wind Energy*, 19(2):301–312, 2016. doi: https://doi.org/10.1002/we.1833. URL `https://onlinelibrary.wiley.com/doi/abs/10.1002/we.1833`.

Trevor J Hastie. Generalized additive models. In *Statistical models in S*, pages 249–307. Routledge, 2017.

Masataro Hattori and Atsusi Arami. Impact breaking wave pressures on vertical walls. In *Coastal Engineering 1992*, pages 1785–1798. 1993.

Bas Hofland, Mirek Kaminski, and Guido Wolters. Large scale wave impacts on a vertical wall. *Coastal Engineering Proceedings*, 1(32):15, February 2011. ISSN 2156-1028. URL `https://icce-ojs-tamu.tdl.org/icce/index.php/icce/article/view/1312`.

DA Huntley, RT Guza, and AJ Bowen. A universal form for shoreline run-up spectra? *Journal of Geophysical Research*, 82(18):2577–2581, 1977.

Niels G Jacobsen, Jørgen Fredsoe, and Jacob H Jensen. Formation and development of a breaker bar under regular waves. part 1: Model description and hydrodynamics. *Coastal Engineering*, 88:182–193, 2014.

Xavier Kergadallan, Alain Le Berre, and Ronan Sanquer. Tome 1 - mer du nord, manche et atlantique - janvier 2020. *Fiches synthétiques de mesure des états de mer du réseau CANDHIS*, 2020.

O Kimmoun, A Ratouis, L Brosset, et al. Sloshing and scaling: experimental study in a wave canal at two different scales. In *The Twentieth International Offshore and Polar Engineering Conference*. International Society of Offshore and Polar Engineers, 2010.

Rex B Kline. *Principles and practice of structural equation modeling*. Guilford publications, 2015.

Andreas Kortenhaus and Hocine Oumeraci. Classification of wave loading on monolithic coastal structures. In *Coastal Engineering 1998*, pages 867–880. 1999.

Takashi Kuribayashi, Yoshio Muraki, and Goichi Udai. Field investigation of wave forces on breakwater. *Coastal Engineering in Japan*, 2(1):17–27, 1959. doi: 10.1080/05785634.1959.11924448.

Benoit Larroque, Philippe Arnould, Franck Luthon, Pierre-Antoine Poncet, A Rahali, and Stéphane Abadie. In-situ measurements of wave impact pressure on a composite breakwater: preliminary results. *Journal of Coastal Research*, pages 1086–1090, 2018.

Gold RZ Lindeman RH, Merenda PF. Introduction to bivariate and multivariate. *journal of statistical software*, 2006.

C. Lugni, M. Brocchini, and O. M. Faltinsen. Wave impact loads: The role of the flip-through. *Physics of Fluids*, 18(12):122101, December 2006. ISSN 1070-6631, 1089-7666. doi: 10.1063/1.2399077.

C. Lugni, M. Brocchini, and O. M. Faltinsen. Evolution of the air cavity during a depressurized wave impact. II. The dynamic field. *Physics of Fluids*, 22(5):056102, May 2010. ISSN 1070-6631, 1089-7666. doi: 10.1063/1.3409491. URL `http://aip.scitation.org/doi/10.1063/1.3409491`.

Etienne PD Mansard and ER Funke. The measurement of incident and reflected spectra using a least squares method. In *Coastal Engineering 1980*, pages 154–172. 1980.

M. Martin-Medina, S. Abadie, C. Mokrani, and D. Morichon. Numerical simulation of flip-through impacts of variable steepness on a vertical breakwater. *Applied Ocean Research*, 75:117–131, June 2018. ISSN 01411187. doi: 10.1016/j.apor.2018.03.013. URL `https://linkinghub.elsevier.com/retrieve/pii/S0141118717304248`.

RL Miller, S Leverette, J O'Sullivan, J Tochko, and K Theriault. Field measurements of impact pressures in surf. In *Coastal Engineering 1974*, pages 1761–1777. 1975.

Hisashi Mitsuyasu. Shock pressure of breaking wave. *Coastal Engineering Proceedings*, 1(10), 1966. ISSN 2156-1028. URL `https://icce-ojs-tamu.tdl.org/icce/index.php/icce/article/view/2431`.

JR Morison, JW Johnson, SA Schaaf, et al. The force exerted by surface waves on piles. *Journal of Petroleum Technology*, 2(05):149–154, 1950.

M Muttray, H Oumeraci, K Shimosako, and S Takahashi. Hydraulic performance of a high mound composite breakwater. In *Coastal Engineering 1998*, pages 2207–2220. 1999.

Markus Muttray, Hocine Oumeraci, and Erik ten Oever. Wave reflection and wave run-up at rubble mound breakwaters. In *Coastal Engineering 2006: (In 5 Volumes)*, pages 4314–4324. World Scientific, 2007.

I_ Orlanski. A simple boundary condition for unbounded hyperbolic flows. *Journal of computational physics*, 21(3):251–269, 1976.

Hocine Oumeraci, Andreas Kortenhaus, William Allsop, Maarten de Groot, R Crouch, H Vrijling, and H Voortman. *Probabilistic design tools for vertical breakwaters*. CRC Press, 2001.

BT Paulsen, H Bredmose, and HB Bingham. Focused wave impact on a vertical cylinder: Experiment, numerical reproduction and a note on higher harmonics. *IWWWFB28*, 2013.

D. H. Peregrine. Water wave impact on walls. *Annual Review of Fluid Mechanics*, 35(1):23–43, January 2003. ISSN 0066-4189, 1545-4479. doi: 10.1146/annurev.fluid.35.101101.161153. URL `http://www.annualreviews.org/doi/10.1146/annurev.fluid.35.101101.161153`.

L.-R. Plumerault, D. Astruc, and P. Maron. The influence of air on the impact of a plunging breaking wave on a vertical wall using a multifluid model. *Coastal Engineering*, 62:62–74, April 2012. ISSN 03783839. doi: 10.1016/j.coastaleng.2011.12.002. URL `http://linkinghub.elsevier.com.insmi.bib.cnrs.fr/retrieve/pii/S0378383911001864`.

Timothy G Poate, Robert T McCall, and Gerd Masselink. A new parameterisation for runup on gravel beaches. *Coastal Engineering*, 117:176–190, 2016.

John O Rawlings, Sastry G Pantula, and David A Dickey. *Applied regression analysis: a research tool*. Springer Science & Business Media, 2001.

A. de Rouville, P. Besson, and P. Petry. *Etat actuel des etudes internationales sur les efforts dus aux lames*. 1938. Google-Books-ID: _SDCoAEACAAJ.

BG Ruessink, MG Kleinhans, and PGL Van den Beukel. Observations of swash under highly dissipative conditions. *Journal of Geophysical Research: Oceans*, 103(C2):3111–3118, 1998.

G. Sainflou. Essai sur les digues maritimes verticales. 1928.

Gianfausto Salvadori, Giuseppe Roberto Tomasicchio, and Felice D'Alessandro. Multivariate approach to design coastal and off-shore structures. *Journal of Coastal Research*, 65(sp1):386 – 391, 2013. doi: 10.2112/SI65-066.1.

Toru Sawaragi and Masao Nochino. Impact forces of nearly breaking waves on a vertical circular cylinder. *Coastal Engineering in Japan*, 27(1):249–263, 1984.

Y.-M. Scolan. Some aspects of the flip-through phenomenon: A numerical study based on the desingularized technique. *Journal of Fluids and Structures*, 26(6):918–953, August 2010. ISSN 08899746. doi: 10.1016/j.jfluidstructs.2010.06.002. URL `https://linkinghub.elsevier.com/retrieve/pii/S088997461000071X`.

Nadia Senechal, Giovanni Coco, Karin R Bryan, and Rob A Holman. Wave runup during extreme storm conditions. *Journal of Geophysical Research: Oceans*, 116(C7), 2011.

Claude Elwood Shannon. Communication in the presence of noise. *Proceedings of the IRE*, 37(1):10–21, 1949.

Shigeo Takahashi. Design of vertical breakwaters. *PHRI reference document nr. 34*, 2002.

Jentsje W Van der Meer and Cor-Jan M Stam. Wave runup on smooth and rock slopes of coastal structures. *Journal of Waterway, Port, Coastal, and Ocean Engineering*, 118(5):534–550, 1992.

MRA Van Gent. Porous flow through rubble-mound material. *Journal of waterway, port, coastal, and ocean engineering*, 121(3):176–181, 1995.

Henk Kaarle Versteeg and Weeratunge Malalasekera. *An introduction to computational fluid dynamics: the finite volume method*. Pearson education, 2007.

Th Von Karman. The impact on seaplane floats during landing. 1929.

Herbrt Wagner. Über stoß-und gleitvorgänge an der oberfläche von flüssigkeiten. *ZAMM-Journal of Applied Mathematics and Mechanics/Zeitschrift für Angewandte Mathematik und Mechanik*, 12(4):193–215, 1932.

J. Wienke and H. Oumeraci. Breaking wave impact force on a vertical and inclined slender pile—theoretical and large-scale model investigations. *Coastal Engineering*, 52(5):435–462, May 2005. ISSN 0378-3839. doi: 10.1016/j.coastaleng.2004.12.008. URL `http://www.sciencedirect.com/science/article/pii/S0378383904001735`.

B.D. Williamson, P.B. Gilbert, M. Carone, and N. Simon. Nonparametric variable importance assessment using machine learning techniques. *UW Biostatistics Working Paper Series*, (422), 2017.

Cort J Willmott. On the validation of models. *Physical geography*, 2(2):184–194, 1981.

Simon N Wood. Thin plate regression splines. *Journal of the Royal Statistical Society: Series B (Statistical Methodology)*, 65(1):95–114, 2003.

Simon N Wood. Low-rank scale-invariant tensor product smooths for generalized additive mixed models. *Biometrics*, 62(4):1025–1036, 2006.

Marcel Zijlema, Guus Stelling, and Pieter Smit. Swash: An operational public domain code for simulating wave fields and rapidly varied flows in coastal waters. *Coastal Engineering*, 58(10):992–1012, 2011.